

Contribution of Pseudo-Focused Soft Protons to the Background of *Athena*

Dissertation

der Mathematisch-Naturwissenschaftlichen Fakultät
der Eberhard Karls Universität Tübingen
zur Erlangung des Grades eines
Doktors der Naturwissenschaften
(Dr. rer. nat.)

vorgelegt von
Roberta Amato
aus Palermo/Italien

Tübingen
2021

Gedruckt mit Genehmigung der Mathematisch-Naturwissenschaftlichen Fakultät der
Eberhard Karls Universität Tübingen.

Tag der mündlichen Qualifikation:

17.03.2021

Stellvertretender Dekan:

Prof. Dr. József Fortágh

1. Berichterstatter/-in:

Prof. Dr. Andrea Santangelo

2. Berichterstatter/-in:

Dr. Teresa Mineo

Abstract

This PhD thesis explores the role of low energy protons, the so-called ‘soft protons’, as a component of the background in view of the future ESA’s X-ray mission *Athena*. As a matter of fact, a high level of soft proton flux at the focal plane of *Athena* can adversely affect the scientific goals of the mission. To prevent this, a correct estimate of the soft proton flux expected at the focal plane of the satellite is fundamental. Such an estimate can be achieved only if the reflectivity of soft protons from the optics is well understood, with efforts on both the experimental and the theoretical sides.

To this aim, I applied the model of reflectivity of particles at grazing incidence proposed by Remizovich et al. (1980), under the non-elastic approximation, to the experimental measurements of proton scattering at low incident angles from *XMM-Newton* and *eROSITA* mirror samples. The mismatch between the model and the experimental data led me to create a new analytical semi-empirical model, where the parameter σ enclosing the micro-physics of the interaction between the protons and the mirror lattice is directly derived by fitting the data. This new model gives a more accurate estimate of the scattering efficiency and energy loss distributions, but depends on the specific materials *eROSITA* and

XMM-Newton are made of. For the model to be applied to *Athena*, new experimental data on *Athena*'s optics, the Silicon Pore Optics (SPO), are necessary.

These new data were acquired during dedicated experimental campaigns carried out by the Institut für Astronomie und Astrophysik of the University of Tübingen. The experiment consisted in measuring the scattering of low energy protons at grazing incidence from an *Athena* SPO sample, at two different incident energies, ~ 470 keV and ~ 170 keV, and at four different incident angles, 0.6° , 0.8° , 1.0° , 1.2° . The new data are consistent, within the error bars, with the data from the *eROSITA* mirror sample, so that the same model can be used to estimate the scattering efficiency of SPO. A more accurate model can be built from a fit of the new data sets, provided that energy loss measurements are retrieved from the raw data.

The new semi-empirical model can be implemented in a ray-tracing code to build a specific response matrix for protons. The construction of a proton response matrix is a 2-years project that falls within the AHEAD2020 activities, in view of the launch of *Athena*. The project foresees the construction of a proton response matrix for *XMM-Newton* as a reliable tool for the deconvolution of observed soft protons spectra. If the validation of this response matrix is successful, then the same procedure can be used to produce an analogous proton response matrix for *Athena*. In this framework, I performed a Geant4 simulation of the interaction of soft protons with the focal plane of *XMM-Newton*, consisting in a detailed representation of the 7 CCDs of the MOS camera, the filters, and the proton shields surrounding the focal plane assembly. The coupling of the Geant4 simulation with the output of

the aforementioned ray-tracing will bring to the proton response matrix for *XMM-Newton*.

To reach a round research profile, I also analysed observational X-ray data from two binary X-ray sources, which represent ideal cases to test to what extent soft protons can affect the quality of observational data. The low level of background required for *Athena* will improve the knowledge we have of these systems and will enhance advanced studies for a wider sample of X-ray binaries.

The first source is a very-faint millisecond pulsar in the globular cluster M22, for which I conducted a multi-wavelength search for counterparts. The lack of any optical counterpart returned an upper limit on the mass of the companion, allowing for a classification of the system as a so-called black widow binary, i.e., a low-mass X-ray binary with a companion star of mass $M \ll 0.1M_{\odot}$. The analysis of the X-ray spectra favoured an intra-binary shock scenario as mechanism responsible for the X-ray emission.

The second source is the well-known high-mass X-ray binary Vela X-1, for which I performed a high-resolution spectroscopy study of a *Chandra*/HETGS archival data, taken when the line of sight is intersecting the photoionisation wake. Standard plasma diagnostic techniques and simulations with the photoionisation codes CLOUDY and PION (in SPEX) suggested the presence of a multi-component plasma, which is typical for high-mass X-ray binaries with clumpy winds.

Acknowledgements

When I was in Amsterdam, I had the chance to attend the PhD defence of a colleague of mine. While celebrating, he said something that got stuck in my mind: "When we do science at our level, the most important thing is that we are comfortable and happy with the people we work with." And that is all. A PhD is a very long journey, both in science and in personal growth. And this journey is never done alone. This is why I have the duty and the pleasure to thank all the people that accompanied me all the way to the end of this incredible experience.

First of all, I want to thank Teresa, who guided me, taking me by hand while I was doing the first steps, and letting me go alone when I was independent enough to walk on my own. She taught me to dive into every problem, not to stop at the surface, to manage multiple tasks at once, and to work as part of a team. Secondly, I want to thank my other supervisor, Andrea. Even though not always present, he never gave me the impression of being left alone and showed me support and appreciation, hidden beyond positive criticism and clever sarcasm. You both showed me two different sides of the same medal. Thanks to the both of you I grow up as a researcher and as a scientist.

I also want to thank all the people of the EXACRAD group in Tübingen: Emanuele, Sebastian, Chris and especially Alejandro, who was infinitely patient with me in the lab. All the things that I learnt on the experimental side, I learnt from him. I also thank all the people I collaborated with, starting from Antonello, Melania, and Ciro, at the institute in Palermo, Rosario, Tiziana, and all the people of via Archirafi. Thanks to Stefano Bianchi, Natalie Hell, Domitilla de Martino, and Claudio Macculi, for the long, instructive scientific discussions over mails and video calls. Thanks from the bottom of my heart to Simone and Valentina, who guided me with the Geant4 simulation, and to Silvano, who represented a positive example and an inspirational figure from the day we met. And thanks to many, many others whose paths crossed mine, confronting each other and talking of what connects us all: the passion for science.

However, as I already said, a PhD is not only a journey in research. It is, most of all, a journey of personal growth. And from this point of view, there have been a lot of people that shared the best and the worst of it with me. Amongst all, the first and most important one is my mum, who always steps aside for me, listens to me, and shares my frustration and joy. Thanks to my dad, who taught me that the greatest achievements take the hardest work.

Thanks to the two most incredible people in my life: to my sister Alice, who always reminds me to not give up on my dreams, with all the bravery and the strength she shows every day; and to my brother Salvatore, who keeps me from cutting off my roots and always reminds me that sometimes happiness lies in the small things of everyday life. Thanks to my aunt, who always looks out for me from a distance. And

thanks to my grandmother, who sadly passed away while I was in Germany. I know we could not say goodbye, but you are now in that special place that keeps you, grandma, grandpa, and uncle alive.

Thanks to the friends of a lifetime, Nicola, Simona, and Giorgio: you are my certainties, my points of references, my lighthouses in the darkest moments, and the people I want to shared the brightest ones with. Thanks to all the friends I have in Prizzi, that makes me feel closer to my hometown, wherever I am. Thanks to the people from INAF-IASF Palermo, who made me enjoy very much my permanence there. Thanks to my colleagues in Tübingen, to Martina, Enza and Manfredi, to Samuel and Paul, and to all the people that helped me to build a second home. Thanks to Alessio: no matter where we are in the world, you will always be the best colleague I could have ever hoped for.

Finally, I have two more special thanks for the two people that changed my life the most and made this experience the best possible. To you, Victoria. Working together with you was one of the best things of my whole PhD. You created a stimulating and healthy environment, to grow as scientists and especially as a human being. It was a true honour meeting you.

And to you Nico. Even far apart, you are always by my side.

R.

30th November 2020

Quando ero ad Amsterdam, ho avuto la possibilità di assistere all'esame finale di dottorato di un mio collega. Durante i festeggia-

menti, lui disse qualcosa che mi rimase impresso nella mente: "Quando facciamo scienza al nostro livello, la cosa più importante è che siamo a nostro agio e felici con le persone con le quali lavoriamo". E questo è tutto. Un dottorato di ricerca è un viaggio molto lungo nella scienza, come nella crescita personale. Ed è un viaggio che non viene mai fatto in solitudine. Per questo ho il dovere e il piacere di ringraziare tutte le persone che mi hanno accompagnato in questa incredibile esperienza.

Il primo ringraziamento è per Teresa, che mi ha guidato, prendendomi per mano mentre muovevo i primi passi, finché non sono diventata abbastanza indipendente da camminare da sola. Lei mi ha insegnato ad approfondire ogni problema, a non fermarmi in superficie, a gestire più compiti contemporaneamente e a lavorare in squadra. Il secondo ringraziamento è per l'altro mio supervisor, Andrea. Anche se non sempre presente, non mi ha mai dato l'impressione di essere lasciata da sola e mi ha mostrato sostegno e apprezzamento, nascosti dietro alle critiche positive e ad un pungente sarcasmo. Entrambi mi avete mostrato due facce molto diverse della stessa medaglia. Grazie ad entrambi sono cresciuta come ricercatrice e come scienziata.

Devo anche ringraziare tutte le persone del gruppo EXACRAD di Tübingen, Emanuele, Sebastian, Chris e soprattutto Alejandro, che è stato infinitamente paziente con me in laboratorio. Tutte le cose che ho imparato sul lato sperimentale, le ho imparate da lui. Ringrazio anche tutte le persone con cui ho collaborato, a partire da Antonello, Melania e Ciro dell'istituto di Palermo, Rosario, Tiziana, e tutte le persone di via Archirafi. Grazie a Stefano Bianchi, Natalie Hell, Domitilla de Martino e Claudio Macculi, per le lunghe e istruttive discussioni scientifiche via mail e in video call. Grazie di cuore a Simone e Valentina, che mi hanno

guidato per la simulazione Geant4, e a Silvano, che ha rappresentato un esempio positivo e una figura d'ispirazione fin dal giorno in cui ci siamo incontrati. E grazie a tanti, tanti altri che hanno incrociato la loro strada con la mia, confrontandosi e parlando di ciò che ci unisce tutti: la passione per la scienza.

Tuttavia, come ho già detto, un dottorato non è solo un viaggio nella ricerca. È, soprattutto, un viaggio di crescita personale. E da questo punto di vista, ci sono state molte persone che hanno condiviso con me i momenti migliori e peggiori di questo viaggio. Fra tutti, la prima e la più importante è mia madre, che sempre si mette in ombra per me, sempre mi ascolta, sempre condivide la mia frustrazione e la mia gioia. Grazie a mio padre, che mi ha insegnato che le soddisfazioni più grandi richiedono il lavoro più duro.

Grazie alle due persone più incredibili della mia vita: a mia sorella Alice, che mi ricorda di non rinunciare mai ai miei sogni, con tutto il coraggio e la forza che dimostra ogni giorno; e a mio fratello Salvatore, che mi trattiene dal tagliare le mie radici e mi ricorda sempre che a volte la felicità sta anche nelle piccole cose di ogni giorno. Grazie a mia zia, che mi guarda sempre da lontano. E grazie a mia nonna, che se ne è andata mentre ero in Germania. So che non abbiamo potuto dirci addio, ma ora sei in quel posto speciale che tiene in vita te, il nonno, la nonna e lo zio.

Grazie agli amici di una vita Nicola, Simona e Giorgio: siete le mie certezze, i miei punti di riferimento, i miei fari nei momenti più bui e le persone con le quali voglio condividere quelli più luminosi. Grazie a tutti gli amici che ho a Prizzi, che mi fanno sentire più vicina alla mia città natale, ovunque io sia. Grazie alle persone dell'istituto INAF-

IASF di Palermo, che hanno reso molto piacevole la mia permanenza lì. Grazie ai miei colleghi di Tübingen, a Martina, Enza e Manfredi, a Samuel e Paul, e a tutte le persone che mi hanno aiutato a costruire una seconda casa. Grazie ad Alessio: non importa dove siamo nel mondo, tu sarai sempre il miglior collega che avessi mai potuto desiderare.

Infine, ho ancora due ringraziamenti speciali per le due persone che più mi hanno cambiato la vita e che hanno reso questa esperienza la migliore possibile. A te, Victoria. Lavorare insieme a te è stata una delle cose migliori di tutto il dottorato. Hai creato un ambiente stimolante e sano, in cui crescere come scienziati e soprattutto come essere umani. Incontrarti è stato un vero onore.

E a te Nico. Anche se a distanza, sei sempre al mio fianco.

R.

30 Novembre 2020

Table of contents

Introduction	1
1 Soft protons as a component of the background of the future X-ray mission <i>Athena</i>	7
1.1 <i>Athena</i> mission concept	8
1.2 The background of imaging X-ray missions	11
1.3 Soft protons as a component of the particle background	12
1.3.1 <i>Athena</i> 's requirement for the soft proton background	16
2 Scattering at grazing incidence of low energy protons from X-ray mirrors	19
2.1 Analytical model of Remizovich (1980) in non-elastic approximation	19
2.1.1 The parameter σ	25
2.2 Experimental measurements on <i>XMM-Newton</i> and <i>eROSITA</i> mirror samples	26

2.3	Analysis of the experimental data with the Remizovich model: a semi-empirical approach	29
2.3.1	Results of the fit and discussion	32
2.3.2	Comprehensive analysis of all the data sets	36
2.4	Summary	40
3	Experimental Activity	45
3.1	Experimental set-up	46
3.1.1	Beamline setup	47
3.1.2	Data acquisition chain	49
3.1.3	Alignment and angular calibration	50
3.2	Efficiency definition and normalisation measurement	52
3.2.1	Uncertainty calculation	55
3.3	Results on the scattering efficiency	58
3.3.1	Comparison with the <i>eRosita</i> measurements	61
3.4	Remarks and future perspectives	64
4	Geant4 simulations of XMM-Newton/EPIC MOS	67
4.1	<i>XMM-Newton</i> in a nutshell	70
4.2	Geometry of <i>XMM-Newton</i> focal plane for the Geant4 simulation	71
4.2.1	The EPIC MOS cameras	74
4.2.2	The Filters	75
4.3	Simulation set-up and preliminary results	75
4.4	Remarks and future perspectives	80
5	Observational Astronomy	83
5.1	Introduction on accreting X-ray binary systems	85

5.1.1	Millisecond pulsars	89
5.1.2	Supergiant X-ray binaries	91
6	The binary millisecond pulsar M22A	95
6.1	Introduction	95
6.2	X-ray observations and data reduction	98
6.3	Source detection and astrometric corrections of the <i>Chandra</i> observation	99
6.4	X-ray Data analysis	103
6.5	Optical observations	107
6.6	The γ -ray emission from M22	111
6.7	Discussion	112
6.8	Conclusions	121
7	A high resolution look at the photoionisation wake of Vela X-1	125
7.1	Introduction	125
7.2	Data reduction and temporal analysis	130
7.3	High-resolution spectroscopy	132
7.3.1	Iron region	134
7.3.2	Sulphur region	136
7.3.3	Silicon region	137
7.3.4	Magnesium region	139
7.3.5	Neon region	140
7.4	Photoionisation models with CLOUDY and SPEX . . .	142
7.5	Discussion	146
7.5.1	The Iron complex	146
7.5.2	Plasma properties	149

7.5.3	Wind geometry	152
7.6	Future perspectives with <i>XRISM/Resolve</i> and <i>Athena/X-IFU</i>	156
7.7	Conclusions	158
Conclusions		167
References		173
Appendix A Overall fits with the semi-empirical model		207
Appendix B Comparison of SPO data with the semi-empirical model		215

Introduction

The Advanced Telescope for High Energy Astrophysics (*Athena*, Nandra et al., 2013) is the future X-ray mission of ESA, planned to fly in the early 2030s. *Athena* will address the scientific theme ‘The Hot and Energetic Universe’, looking for answers to two key topics of modern X-ray astrophysics: how ordinary matter assembles into the large scale structures that we see today (the ‘Hot’ universe) and how black holes grow and influence the Universe (the ‘Energetic’ universe). To achieve this goal, *Athena* will observe, among others X-ray sources, clusters of galaxies, high- z AGNs, and the Warm Hot Intergalactic Medium (WHIM).

One of the biggest challenges of the mission is represented by the particle background. Every X-ray satellite is subjected to background contamination from charged particles, such as galactic and extra-galactic cosmic rays, solar particles, and secondaries generated inside the satellite itself. High levels of background can compromise the observational results and, in the very end, the goals of the missions. This is crucial especially for *Athena*, which will look at distant and, consequently, very faint X-ray sources: to achieve meaningful

observational data, the particle background level must be the lowest possible.

Amongst the components of the particle background, a key role is played by low energy protons, called ‘soft protons’, present in the solar wind and trapped in the Earth magnetosphere. When soft protons impact on X-ray mirrors at low incidence angles, they are pseudo-reflected and funneled towards the focal plane, where they reach the detectors. The signal produced by soft protons is similar to that of X-ray photons, so that the two cannot be disentangled. Hence, if the soft proton flux is high, no meaningful source spectrum can be extracted from the observational data. Soft protons have been affecting the operability of current X-ray missions, such as the *Chandra X-ray Observatory* and *XMM-Newton*, significantly reducing their good time intervals and their duty cycles – for instance, the observing time of *XMM-Newton* is reduced by $\sim 30\text{--}40\%$. In the interests of *Athena*, it is necessary to keep the level of soft protons as low as possible, to exploit the satellite at its best and accomplish the scientific goals. The soft proton flux can be reduced on board by mechanical or magnetic shielding, i.e., blocking filters and/or magnetic diverters. However, to implement such solutions, it is fundamental to have a correct estimate of the flux expected at the instrumental focal plane. And such an estimate necessarily relies upon a good model of the reflectivity of soft protons from the optics.

The work presented in this PhD thesis falls into the framework of the background evaluation of *Athena*, with a specific focus on the transmission of soft protons from the Silicon Pore Optics (SPO) of *Athena*. The thesis is structured as follows. After a brief introduction

on the *Athena* mission concept and on the issue of soft protons in Chapter 1, I illustrate in Chapter 2 the exploration of already available experimental data of scattering efficiencies from X-ray mirror samples of *eROSITA* (Diebold et al., 2017, 2015) and *XMM-Newton* (Rasmussen et al., 1999). Starting from the reflectively model of charged particle at grazing incidence proposed by Remizovich et al. (1980) in non-elastic approximation, I derived a new model, in which the parameter σ describing the micro-physics of the interaction of the protons with the reflecting surface is directly retrieved from a fit of the data (Amato et al., 2020). This new semi-empirical analytical model allows for the estimate of the scattering efficiency of *eROSITA* mirrors. Moreover, the model is valid for any X-ray satellite carrying on-board the same golden-coated optics of *eROSITA* and *XMM-Newton*. Of course, the chemical composition and the physical properties of *Athena*'s SPO are different. It is clear, then, that the model developed by far needs to be improved with experimental data on SPO samples.

New data on SPO were collected within several experimental campaigns, as a part of the EXACRAD (Experimental Evaluation of Athena Charged Particle Background from Secondary Radiation and Scattering in Optics) project, funded by ESA. The experiment was conducted at the Van der Graaff accelerator of the Goethe University of Frankfurt and the results are presented in Chapter 3. The data sets consist in scattering efficiency measurements from a single wafer of a SPO sample hit by a grazing incident proton beam at two different energies, 172 keV and 471 keV, and at four different incident angles, 0.6° , 0.8° , 1.0° , and 1.2° . The scattering efficiencies of SPO are consistent with those from *eROSITA*, so that, in a first approximation, the same semi-empirical

analytical model can be used also to estimate the proton flux expected at the focal plane of *Athena*. A more complete model can be built, provided that energy losses are retrieved from the experimental raw data.

A useful tool to estimate the soft proton spectrum expected at the focal plane of an X-ray telescope is a response matrix specific for protons. Response matrices are common tools of X-ray analysis, used to extract scientific parameters from source spectra. They give the probability that an incoming photon of energy E is detected in an output detector channel PHA . A response matrix takes into account the effective area of the satellite, as well as the energy redistribution of the detected events. To build a proton response matrix, it is necessary to simulate the interaction of the particles with all the elements encountered along their path, i.e, the optics, the filters, the focal plane assembly, and the detectors. Moreover, a proton response matrix has to be validated with real soft protons data. To this aim, *XMM-Newton* represents the best satellite. If the validation of a proton response matrix for *XMM-Newton* is positive, than the same process can be used to produce a similar response matrix for *Athena*.

In building the *XMM-Newton* proton response matrix, the reflection of grazing incidence protons from the optics can be simulated by a ray-tracing code available at INAF/IASF of Palermo (Lotti et al., 2018; Mineo et al., 2017), while the interaction of protons with all the other elements can be simulated using the Monte Carlo-based toolkit Geant4, developed by CERN. In Chapter 4, I illustrate the geometry built within Geant4, which includes a simple mass model of the focal

plane assembly of *XMM-Newton* and a detailed representation of the filters and of the EPIC MOS cameras. I show the preliminary results of the simulation, which, coupled with the ray-tracing output, will lead in the future to the production of the matrix.

The second part of this thesis presents two preparatory scientific cases for *Athena*, belonging to two different categories of X-ray binary systems: high-mass and low-mass binaries. The geometrical and physical properties of the two categories of X-ray binaries are briefly discussed in Chapter 5, where I also illustrate the limitation on the scientific knowledge due to the instrumental properties of currently operational X-ray satellites and the improvements of the next generation of satellites, especially of *Athena*.

The first source (Chapter 6) is the radio millisecond pulsar PSR J1836-2354A in the Galactic globular cluster M22, for which we conducted a multiwavelength search for counterparts in the gamma, optical, and X-ray wavebands (Amato et al., 2019). The analysis of the X-ray spectra led to discriminate between the physical mechanisms of X-ray emission, favoring an intra-binary shock scenario rather than thermal emission. Constrains on the mass of the companion determined the nature of the system as a black widow (low-mass X-ray binaries with a companion star of mass $M \ll 0.1M_{\odot}$) rather than redback (where companions have masses $M \sim 0.1 - 0.4M_{\odot}$). The source being very faint in X-rays, we show how *Athena* will improve the spectral analysis and how a high soft proton flux can affect the quality of the data.

The second source (Chapter 7) is the supergiant high-mass X-ray binary Vela X-1, for which we analysed the high-resolution spectrum

obtained with *Chandra*/HETGS at a specific orbital phase (Amato et al., accepted). After a blind search for spectroscopic features with a Bayesian blocks-based algorithm, we characterised the plasma, distinguishing a collisional component within the photoionised medium. Simulations with the photoionisation codes CLOUDY and PION (in SPEX) led to the conclusion of a multi-component plasma, typical for high-mass X-ray binaries with clumpy winds.

Finally, in the Conclusions section I summarise the main results and the future implications for *Athena* of all the different topics dealt within this thesis.

This PhD research project has been carried out in a cotutelle agreement between the University of Palermo, Italy, and the Eberhard Karls University of Tübingen, Germany. The position has been equally funded by the University of Palermo and the Istituto Nazionale di Astrofisica (INAF). The activities have been conducted mainly at the Istituto di Astrofisica Spaziale e Fisica Cosmica di Palermo (INAF-IASF Palermo), under the supervision of Dr. Teresa Mineo, and at the Institute for Astronomy and Astrophysics (IAAT) of the University of Tübingen, in the High-Energy Astrophysics group of prof. Andrea Santangelo.

Chapter 1

Soft protons as a component of the background of the future X-ray mission *Athena*

The Advanced Telescope for High-Energy Astrophysics (*Athena*, Nandra et al., 2013) is a future large-class X-ray mission of the European Space Agency (ESA), with the primary goals of mapping hot gas structures and searching for supermassive black holes at cosmological distance. *Athena* will push the sensitivity threshold to a flux lower than any current flying X-ray missions, with very stringent requirements on the level of particle background.

In this Chapter, I first briefly illustrate the *Athena* mission concept (Sect. 1.1) and its non-X-ray background (Sect. 1.2); then, I focus on low-energy protons as a component of the particle background

(Sect. 1.3), explaining what they are, how they were first discovered and why they have a crucial role for *Athena*.

1.1 *Athena* mission concept

Athena is the next ESA's L-class (L2) X-ray mission, selected in the frame of the scientific program Cosmic Vision 2015-2025. With the scientific theme 'The Hot and Energetic Universe', *Athena* will address two main astrophysical questions:

- How does ordinary matter assemble into the large scale structures that we see today?
- How do black holes grow and influence the Universe?

The first question concerns the Hot Universe and aims to understand the formation and evolution of groups and clusters of galaxies, the chemical history of the hot baryons, cluster feedbacks, such as jets from Active Galactic Nuclei, and the Warm-Hot Intergalactic Medium. The second question refers to the Energetic Universe, with the goal of understanding the formation and early growth of supermassive black holes, the obscured accretion and galaxy formation, the Galaxy-scale feedback of the interaction of supermassive black holes with the surroundings, and the physics of accretion in general.

The launch is planned for the early 2030s. Operation will start when the satellite will reach the Sun-Earth Lagrangian point L_2 ¹, at a

¹Currently, there are strong suggestions in favour of the Lagrangian point L_1 , between the Earth and the Sun, whose particle environment is better known and understood.

distance of 1.5 million km from Earth. *Athena* will host on board two detectors: the X-ray Integral Field Unit (X-IFU) and the Wide Field Imager (WFI). The X-IFU (Barret et al., 2013) is a cryogenic X-ray spectrometer, based on a large array of Transition Edge Sensors (TES). It will deliver spatially resolved spectra, with an energy resolution of 2.5 eV at 6 keV in the 0.2 keV–12 keV energy band, over a field of view of 5' in equivalent diameter. The WFI (Rau et al., 2013) is a silicon-based detector, which will provide imaging surveys over a field of view of 40'×40', in the 0.1 keV–15 keV energy band, as well as time-resolved spectra.

Athena will consist of a single-body telescope, with 12 m focal length (Willingale et al., 2013), based on ESA's Silicon Pore Optics (SPO) technology. SPO are made of rectangular blocks of silicon wafer, stacked on top of each other and nested in order to fill the pupil of the telescope. The wafers are properly curved so that two consecutive blocks reproduce a Wolter type-I geometry. Each single wafer is carved on one side in order to have several parallel ribs (with a thickness of ~0.15 mm). The other face of the Si wafer is coated with a reflecting material (iridium and silicon carbide for *Athena*, cfr. Sect. 3.1.1). When the Si slices are pressed one upon the other, they cold-bond together, without any gluing. The empty spaces between the ribs constitute the 'pores', through which X-ray photons impinging at grazing incidence are reflected towards the focal plane.

The advantage of using SPO reflects both on the costs and on the weight of the telescope. It will be possible, indeed, to reach the

nominal effective area of 1.25 m^2 at 1 keV^2 , never had before on any X-ray imaging telescope (see the figure of merit of Fig. 1.1, left panel). With a nominal angular resolution of $5''$ half energy width, *Athena* will reach a grasp³ greater than $0.2 \text{ m}^2 \text{ deg}^2$ at 7 keV for the WFI, higher than any operational or future X-ray observatory (Fig. 1.1, right panel).

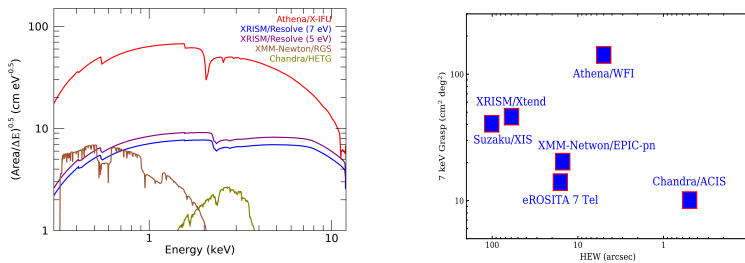


Fig. 1.1 *Left panel*: figure-of-merit for selected operational and future X-ray observatories, consisting of the square root of the ratio between the effective area and the energy resolution (Guainazzi and Tashiro, 2018). *Right panel*: 7 keV Grasp versus High Energy Width (HEW) for selected operational and future X-ray observatories (Guainazzi and Tashiro, 2018; Predehl et al., 2020).

²https://www.cosmos.esa.int/documents/400752/400864/Athena_SciRd_v2.6_noTracking.pdf/6e506240-c8a5-3956-e80e-cf787eb712b6?t=1585220920350.

³According to the Athena Science Requirements Document (cfr. note 2), the grasp is defined as the effective area times the field of view.

1.2 The background of imaging X-ray missions

X-ray imaging telescopes equipped with grazing incidence optics are subjected to three main components of the total background (as in Lotti et al., 2017):

- the Cosmic X-ray Background (CXB), made of all the X-ray photons coming from diffuse or unresolved sources;
- the soft proton component, which includes protons of the Earth magnetosphere with energy up to a few hundreds of keV, that are pseudo-focused by the mirror on the focal plane detectors (see below);
- the Non-X-ray Background (NXB), generated by all kind of charged particles crossing the satellite and reaching the detectors at the focal plane. NXB comprehends Cosmic Rays, Solar Energetic Particles (SEPs), high- and low-energy protons, secondary particles generated by the interaction of the previous particles with the satellite itself, etc.

While the CXB cannot be reduced, except by improving the resolving power of future telescopes, the NXB can be limited inserting magnetic or mechanical elements on board⁴.

High level of NXB, as well as of soft protons, can compromise the scientific goals of the mission and, in the worst case scenario,

⁴For instance, a magnetic diverter can be used to deviate electrons away from the focal trajectory, as well as anti-coincidence (e.g., for the X-IFU, Macculi et al., 2020) or event selection techniques (WFI, Meidinger et al., 2017). Also thick optical filters can limit the amount of charged particles reaching the detectors, as for the ‘closed’ position of the filter wheel of *XMM-Newton* (cfr. Sect. 4.2.2 and 4.5).

can also damage the detectors at the focal plane. Having a correct estimate of the particle flux expected at the focal plane is then essential in planning any X-ray mission. Two main factors must be taken into account to estimate the background level at the focal plane: the particle environment surrounding the satellite and the physical interactions of all the particles with the telescope itself (Lotti et al. (2018, 2017)).

Among all the components of the background, soft protons play a fundamental role: they are pseudo-focused by X-ray optics towards the detectors at the focal plane, where they produce a signal analogous to those of X-ray photons, thus potentially altering the scientific results (Tiengo, 2007, see below).

1.3 Soft protons as a component of the particle background

Soft protons (SPs) are low-energy protons, with energies up to a few hundreds of keV, present in the solar wind and Earth magnetosphere. When impacting on the mirrors of grazing incidence X-ray telescopes with low incident angles, they are scattered and funneled towards the focal plane, where they reach the detectors, producing signals indistinguishable from the ones generated by X-ray photons.

SPs were already experienced by the NASA's *Chandra X-ray Observatory* (Weisskopf et al., 2000), after its launch on 1999 July 23, in a highly elliptical orbit. While crossing several regions of the Earth magnetosphere, a sudden increase of the background level was registered in the front-illuminated CCDs (Prigozhin et al., 2000), but not in the back-illuminated ones. However, the ultimate proof of the pres-

ence of SPs was achieved when the ESA's *X-ray Multi-Mirror* mission (*XMM-Newton*, Jansen et al., 2001) was launched less than five months later.

On 2000 May 5, *XMM-Newton* observed the Lockman Hole, a sky region with minimal amount of neutral hydrogen gas, and hence, due to the small absorption at low X-ray energies, particularly suited to detect faint AGNs in a long observation. The detectors on board registered a sudden and flaring increase of the count rates, with the exposed field of view heavily illuminated (see Fig. 1.2). The satellite was in low gain mode, with the gain lowered by a factor of ten, allowing to reach energies up to ~ 300 keV. Moreover, two out of three on-board detectors (MOS1 and MOS2) were shielded with different filters⁵. The two cameras experienced different count rates in the flaring part of the observation (higher for the MOS1 shielded with the thin filter and lower for the MOS2 shielded with the thick one). From the chemical composition of the filters and the amount of energy loss, it was possible to attribute the flares to low energy protons, with energies in the range 1 keV–300 keV. The reconstructed SP spectrum (Fig. 1.3) had a power-law shape up to energies of ~ 50 keV, with a photon index of 2.78 ± 0.04 (Tiengo, 2007).

A more thorough analysis on the *XMM-Newton* particle background has been conducted by Marelli et al. (2017), Salvetti et al. (2017), Ghizzardi et al. (2017), and Gastaldello et al. (2017). By analysing ~ 100 Ms of background events exclusively, from 2000 to 2012, inside and outside the field of view of the EPIC MOS2, authors found that the overall *XMM-Newton* particle background is made of two main

⁵Cfr. Sect. 4 for a more detailed description of *XMM-Newton*'s cameras and filters.

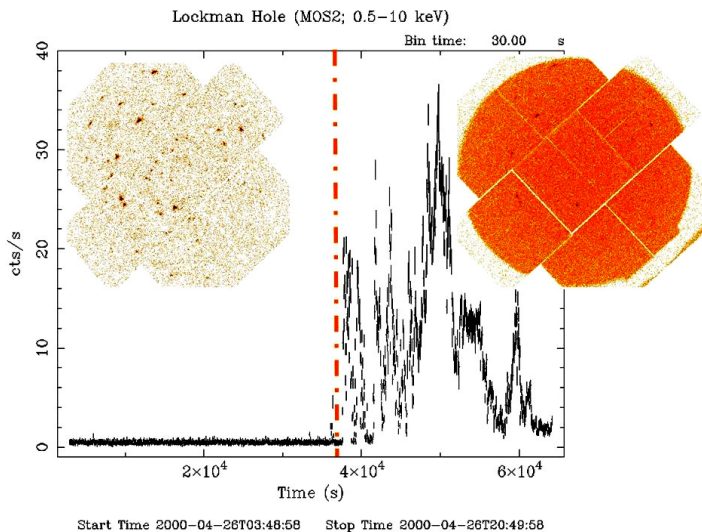


Fig. 1.2 Example of XMM-Newton observation partly affected by soft protons from Tiengo (2007). The second part of the observation shows SP flares, clearly visible both in the fluctuating, high-count rate light curve and in the illuminated image of the MOS2 field of view.

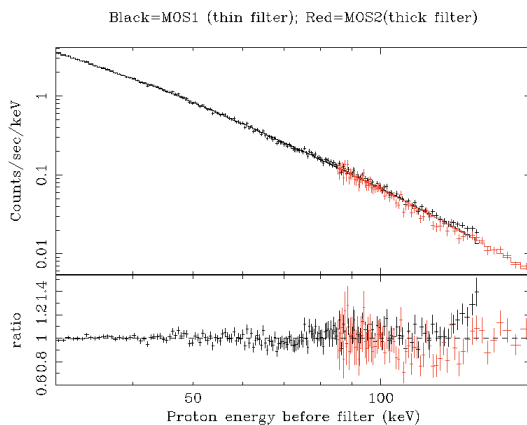


Fig. 1.3 MOS1 (black) and MOS2 (red) background subtracted proton spectra considering the proton energy corrected for the energy loss in the filter. Residuals are with respect to the cutoff power-law model with photon index ~ 3 , as described in the text (Tiengo, 2007).

different components: a ‘quiescent’ one, persistent, unfocused, and at high energies ($E \sim 100$ MeV), and a ‘flaring’ one, highly variable in time and intensity (more than a factor of three), with count rates higher than 1 cts/s. From Geant4 simulations, the first component can be attributed to Compton scattering of hard X-ray photons with the detector or knock-on electrons ejected by the high-energy Galactic cosmic rays protons (Gastaldello et al., 2017; Ghizzardi et al., 2017). On the other hand, the second component is due, indeed, to SPs pseudo-focused from the optics.

Nowadays, at each passage of the proton-rich outer radiation belts of the Earth magnetosphere, the filter wheel on board *XMM-Newton* is turned to the ‘closed’ position: 1.05 mm of aluminium, sufficient to completely stop the protons funneled from the optics (Turner et al., 2001). However, SP flares can also happen in different region of the highly eccentric orbit of the satellite. Since X-ray photons coming from astrophysical sources cannot be disentangled from the flaring SP background, the whole flaring part of any observation has to be entirely discarded. Therefore, proton flares can heavily affect the performance and reliability of scientific observations and the overall duty cycle, reducing, for instance, the *XMM-Newton* observing time by ~ 30 -40% (Ghizzardi et al., 2017).

1.3.1 *Athena’s* requirement for the soft proton background

Athena’s scientific goals address mainly faint and/or cosmological sources, for which the level of background must be low enough to achieve meaningful observational data. The current requirement for the SP flux at the focal plane of *Athena* is that it should be less than

5×10^{-4} cts $\text{cm}^{-2} \text{s}^{-1} \text{keV}^{-1}$ (corresponding to 10% of the total NXB), in the 2 keV–10 keV energy band, for 90% of the observing time⁶. This requirement is especially challenging, given the large collecting area of the optics.

In general, NXB and SPs are crucial for some of the key topics of *Athena*. A low NXB will ensure the determination of low surface brightness spectral features at 6 keV, as in faint clusters or outskirts, or of the bremsstrahlung exponential cut-off, as reported in the *Athena* Science Requirements Document⁶. Though SPs are not necessarily included in this scientific motivation, it is clear that a high level of SP flux can play the same role of the NXB and compromise the scientific results, especially if highly variable and not reproducible.

⁶https://www.cosmos.esa.int/documents/400752/507693/Athena_SciRd_iss1v5.pdf.

Chapter 2

Scattering at grazing incidence of low energy protons from X-ray mirrors

2.1 Analytical model of Remizovich (1980) in non-elastic approximation

A theory for the reflection of particles at grazing incidence from the surface of solid materials was formulated for the first time by Remizovich et al. (1980). Authors analytically derived the energy and angular distributions of a beam of ions reflected at grazing incidence from a mirroring surface.

Following that schematisation, let us suppose that a particle hits a reflecting surface with a grazing angle θ_0 and it is scattered with a polar angle θ and an azimuthal angle φ (see the geometric scheme

of the system in Fig. 2.1). For the sake of convenience, we adopt the definition of Remizovich et al. (1980) of dimensionless polar and azimuthal angles ψ and χ as:

$$\psi = \frac{\theta}{\theta_0} \quad \text{and} \quad \chi = \frac{\varphi}{\theta_0}. \quad (2.1)$$

and of the dimensionless energy of the scattered particle as:

$$u = \frac{T}{T_0}, \quad (2.2)$$

where T_0 and T are its initial and final kinetic energy.

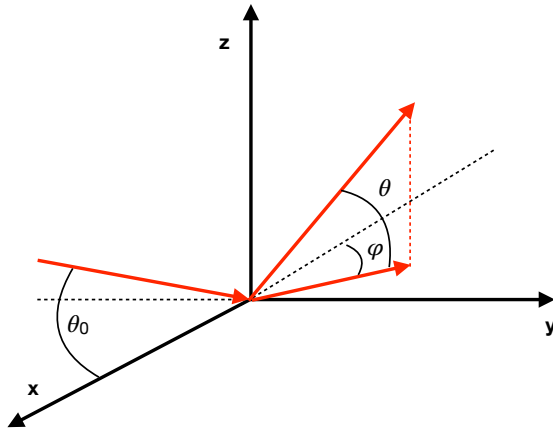


Fig. 2.1 Geometric scheme of the system: the incident beam hits the surface (in the xy plane) with an angle θ_0 and it is scattered with a polar angle θ and an azimuthal angle φ .

The theory of the interaction is developed under the small-angle approximation, that assumes that the product of the mean-squared value

of the scattering angle per unit path $\langle \theta_s^2(T) \rangle$ that the particle covers through consecutive collisions with the ions inside the medium and the whole range R_0 , at the given incident energy T_0 , is much smaller than one, i.e.

$$\langle \theta_s^2(T) \rangle R_0 \ll 1. \quad (2.3)$$

Under the condition of small incidence angles ($\theta_0 \ll 1$ rad), the thickness of the layer crossed by a single particle before emerging from the target is proportional to $\theta_0^3 / \langle \theta_s^2 \rangle$. If the energy T_0 of the incident particles is small enough ($T_0 \ll 1$ GeV for protons), the process of deceleration of particles in the medium can be modelled as a continuous energy loss (continuous slowing down approximation, CSDA). The process is not conservative, i.e. the incident particle loses part of its energy when interacting with the atomic lattice of the mirror. However, if the spectrum of the reflected particles has a sharp maximum close to the input energy T_0 , it is possible to assume (Firsov, 1972):

$$\langle \theta_s^2(T) \rangle \approx \langle \theta_s^2(T_0) \rangle = \text{const.} \quad (2.4)$$

Under all the assumptions stated above, the scattering probability is defined as the ratio of the number of reflected particles in a given direction from a unit surface area per unit time to the number of incident particles on the same unit area per unit time. It can be expressed as a function of the dimensionless variables ψ , χ and u as (Remizovich

et al., 1980):

$$W(\psi, \chi, u) = \frac{3^{1/2}}{2\pi^2} \frac{T_0 \psi}{R_0 \varepsilon(u)} \frac{\exp\{-[4(\psi^2 - \psi + 1) + \chi^2]/4\sigma s(u)\}}{\sigma^{3/2}[s(u)]^{5/2}} \times \text{Erf} \left(\left(\frac{3\psi}{\sigma s(u)} \right)^{1/2} \right) \quad (2.5)$$

where: $\varepsilon(u) = -\langle du/dl \rangle$ is the average energy loss per unit path, i.e the stopping power, which varies with the energy of the beam and with the chemical composition of the reflecting material; $R(T) = \int dT/\varepsilon(T)$ is the resulting average particle range, as a function of the energy; R_0 is the range at the specific incident energy; $s(u)$ is defined as $s(u) = L(T)/R_0 = 1 - R(T)/R_0$, being $L(T) = R_0 - R(T)$ the path travelled by a particle with energy T ; σ is a dimensionless parameter defined as:

$$\sigma = \langle \theta_s^2(T_0) \rangle R_0 / 4\theta_0^2 \quad (2.6)$$

The integration of Eq. 2.5 over the energy and angle coordinates gives the total scattering efficiency:

$$\eta_{\text{tot}} = \int_E \int_{\Omega} W(\psi, \chi, u) d\psi d\chi du \quad (2.7)$$

so that $1 - \eta_{\text{tot}}$ is the probability that the particle is not reflected¹.

The main characteristics of the scattering distribution can be summarised as follows:

¹The scattering probability can be expressed also as a function of the energy alone (see equation 41 of Remizovich et al., 1980), when integrating over the solid scattering angle.

- the maximum of the distribution in the plane $\chi = 0$ peaks at $\psi \sim 0.85$, while it peaks at $\psi \sim 1$ when integrated over the azimuthal angle χ and the energy u ;
- the distribution is symmetric with respect to the scattering azimuthal angle χ , with its maximum at $\chi = 0$;
- smaller values of σ produce lower and broader peaks of the distribution;
- the value of ψ relative to the maximum of the distribution changes also with σ ;
- the scattering distribution depends on the final energy u , but the same scattering probability can be obtained with different values of σ at different u ;

Fig. 2.2 shows an example of contour plot of the scattering function (Eq. 2.5) for a target of Au, with $\theta_0 = 0.36^\circ$, $T_0=250$ keV and $\sigma=50$, at $\chi=0$, in the space $u-\psi$, normalised to its maximum, while Fig. 2.3 shows the 1-D distributions as a function of ψ and of u corresponding to the values highlighted in the contour plot with black and red dashed lines, respectively.

Eq. 2.5 includes several parameters (e.g. $\varepsilon(u)$, $R(T)$, etc.) that can be found in literature. In the present work, $\varepsilon(u)$ and of $R(T)$ were computed interpolating the values retrieved from the NIST PSTAR Database². The Au density was set to 19.3 g/cm³.

²<https://physics.nist.gov/PhysRefData/Star/Text/PSTAR.html>.

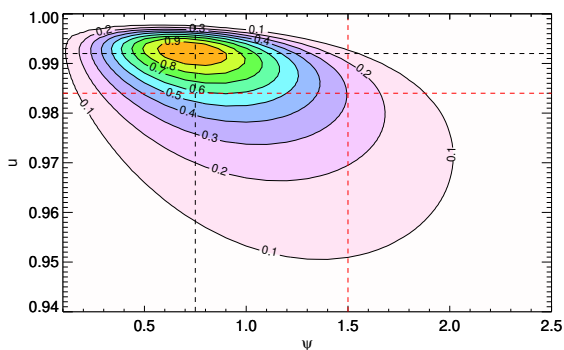


Fig. 2.2 Contour plot of the scattering probability $W(\psi, \chi, u)$ as a function of the polar scattering angle ψ and of the energy u , for $\theta_0 = 0.36^\circ$, $T_0 = 250$ keV, $\chi=0$ and $\sigma = 50$. The plot is normalised to the maximum of the distribution. Dashed black and red lines corresponds to the efficiencies used for Fig. 2.3.

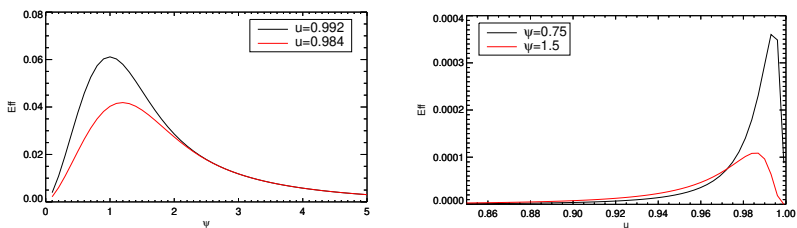


Fig. 2.3 Scattering efficiencies along the red and black dashed lines shown in Fig. 2.2, for $\theta_0 = 0.36^\circ$, $T_0 = 250$ keV, $\chi=0$ and $\sigma = 50$. The left panel shows the curve as a function of ψ at $u=0.992$ (black line) and $u=0.984$ (red line); the right panel is relative to the efficiency distribution vs. u at $\psi=0.75$ (black line) and $\psi=1.5$ (red line). Efficiency values are not normalized.

2.1.1 The parameter σ

The parameter σ in the Remizovich formula (Eq. 2.5) determines the total number of particles reflected from the surface: the larger this value, the larger the number of reflected particles, and the narrower the peak of the distribution (Mashkova and Molchanov, 1985). According to Eq. 2.6, σ can be computed knowing the mean-square scattering angle per unit path and the range, which depends on the scattering properties of the medium. Different approximations have been adopted to evaluate $\langle \theta_s^2(T) \rangle$, depending on the energy and on the angle of the incident particle. In the energy range of the experimental data used in this work, it can be obtained with the following formula (Firsov, 1958; Remizovich et al., 1980):

$$\langle \theta_s^2(T) \rangle = 2\pi n_0 \frac{Z_1^2 Z_2^2 r_e^2}{T^2} L_k \quad (2.8)$$

where n_0 is the density of the atoms in the target, Z_1 and Z_2 are the nuclear charge of the incident particle and of the material of the target, respectively, r_e is the classical electron radius, T the particle energy in units of mc^2 and L_k the Coulomb logarithm, which, in this specific case, can be approximated as:

$$L_k = \ln \left(1 + 0.7 \frac{T_{ev}}{30.5 eV} \frac{Z_1 Z_2}{\sqrt{Z_1^{2/3} + Z_2^{2/3}}} \right) \quad (2.9)$$

where T_{ev} is the energy of the incident charge in unit of electronvolt. Eq. 2.8 is a good approximation of values derived from a theoretical computation based on the assumptions that the inelastic process occur-

ring during the collision can be obtained using the potential for elastic interactions and that the energy of the incident particle is significantly greater than the ionization potential of the atoms (Firsov, 1958).

2.2 Experimental measurements on *XMM-Newton* and *eROSITA* mirror samples

Table 2.1 Incident angles for each incident energy for the *XMM-Newton* and *eROSITA* mirror targets used in this work.

E (keV)	θ_0 (deg)	Reference
250	0.36, 0.51, 0.67, 0.89, 1.06, 1.23	Diebold et al. (2015) ¹
300	0.50, 0.75, 1.00, 1.25, 1.50, 1.75	Rasmussen et al. (1999)
	0.50, 0.64, 0.81	Diebold et al. (2017) ²
500	0.50, 1.00	Rasmussen et al. (1999)
	0.33, 0.48, 0.64, 0.85, 1.02, 1.19	Diebold et al. (2015) ¹
1000	0.30, 0.46, 0.61, 0.83, 1.00, 1.17	Diebold et al. (2015) ¹
1300	0.25, 0.50, 0.75, 1.00, 1.25, 1.50, 1.75	Rasmussen et al. (1999)

¹ Dataset with energy losses explicitly reported.

² Dataset with off-axis measurements at azimuthal angles of about $\pm 2^\circ$.

The only available experimental measurements of reflection of low energy protons from X-ray mirrors were performed on *XMM-Newton* (Rasmussen et al., 1999) and *eROSITA* (Diebold et al., 2017, 2015) samples. A complete list of all the incidence angles and energies is given in Tab. 2.1. In both cases, samples were made of nickel and coated with gold, with a coating thickness >50 nm for *eROSITA* (Friedrich et al., 2008) and $0.2 \mu\text{m}$ for *XMM-Newton* (Stockman et al., 2001).

The first measurements on *XMM-Newton* optics were carried out at the Harvard University, Cambridge Accelerator for Materials Science. The facility included a tandem Van de Graaff accelerator, which produced a monoenergetic proton beam with energy tunable from 0.1 to 3 MeV. The beam divergence was reduced to 3 arcmin level, with consecutive collimating apertures. The mirror sample was mounted on a holder, so that the mirror sample exactly bisected the beam. The position of the detector was fixed at three different scattering angles (0.75° , 1.40° and 2.38°), while the incidence angles varied between 0° and 1.75° in steps of 0.25° . The proton beam had the following energies: 300 keV, 500 keV and 1.3 MeV (see Tab. 2.1). For each configuration, the scattering efficiencies and the output spectra are reported. However, the authors published only uncalibrated spectra from which no useful information on the energy loss could be extracted. In our analysis, we excluded those data points showing a drop in the scattering efficiency, due to the occlusion of the reflecting surface by the bulk of the mirror itself. Errors on the scattering efficiency are derived from the uncertainties on the beam flux and correspond approximately to 40% of the values.

More recent data were obtained by Diebold et al. (2017, 2015), using a piece of a spare mirror shell of the *eROSITA* telescopes, at the ion accelerator facility at the University of Tübingen, a 3 MV single-ended Van de Graaff accelerator, working in the energy range 400 keV–2.5 MeV. The beam line consisted of a pair of entrance slits, a pinhole aperture of 0.1–1 mm diameter, a ~ 80 cm-long collimator, with apertures of 1.0 mm at the entrance and of 0.3 mm at the exit, which limited the maximum opening angle to 0.1° . To achieve low

proton energies, a metal degrader foil was put after the pinhole aperture. It widened the beam and reduced the energy down to 250 keV, 500 keV and 1 MeV in the first campaign (Diebold et al., 2015) and to 300 keV in the second one (Diebold et al., 2017). The mirror target was located on a shiftable plane. The detector, a silicon surface barrier with a low energy threshold of 100 keV and an energy resolution of 10–20 keV, was mounted at a distance of ~ 1 m along the beam line, shiftable to a maximum distance of 75 mm, corresponding to a maximum angle θ of about 4.5° . The beam reached the detector through a 1.2 mm aperture, corresponding to a solid angle of $\sim 1.3 \mu\text{sr}$. Furthermore, only the data from Diebold et al. (2015) reported explicitly both the scattering efficiency and the energy loss measurements.

The experimental data can be directly compared if they are expressed in the normalised coordinate space of Eq. 2.1-2.2 (i.e., $\psi = \theta/\theta_0$, $\chi = \phi/\theta_0$, $u = T/T_0$) and if the experimental scattering efficiency are normalised coherently as:

$$\eta(\psi, \xi) = \eta_{\text{exp}}(\theta, \phi) \theta_0^2 \quad (2.10)$$

where η_{exp} is the measured efficiency (in units of sr^{-1}). Fig. 2.4 shows two representative examples, for the incident energies of 250–300 keV and 500 keV.

All data points from *eROSITA* optics are well in agreement at large scattering angles ($\psi > 1.5$), while a modest spread in the data relative to the first campaign (Diebold et al., 2015) is observed at angles close

to the incident one ($\psi \simeq 1$). This spread is not present in Diebold et al. (2017) measurements.

XMM-Newton measurements seem not to follow the same trend of *eROSITA* data (Fig.2.4, lower panel): the peaks appear to be shifted towards higher scattering angles and the efficiencies are slightly higher and more spread-out. Moreover, the low number of available data points (e.g., only two data points are available for the incident energy of 500 keV) prevents us to state more on the comparison.

2.3 Analysis of the experimental data with the Remizovich model: a semi-empirical approach

The analytic expression of Eq. 2.5 depends on the parameter σ (Eq. 2.6, with $\langle \theta_s^2(T_0) \rangle$ given by Eq. 2.8 and 2.9). However, after calculating the value of this parameter with Eq. 2.8, the theoretical curves never led to consistent results with the experimental data, as the theoretical scattering functions were higher and the energy losses lower than the experimental points, as showed in Fig. 2.4 (grey dashed curves), for two representative incident angles of 0.5° 1.0° (cfr. also Fig. 2.5). In general, high values of σ are indicative of a quasi-elastic scattering. It is not surprising, thus, that these values of σ return efficiencies higher than the data, closer to an elastic scattering. Assuming the target surface made of nickel instead of gold (nickel being the material of the substrate of the optics of both *XMM-Newton* and *eROSITA*) also did not significantly change the mismatch. Hence, we decided to adopt

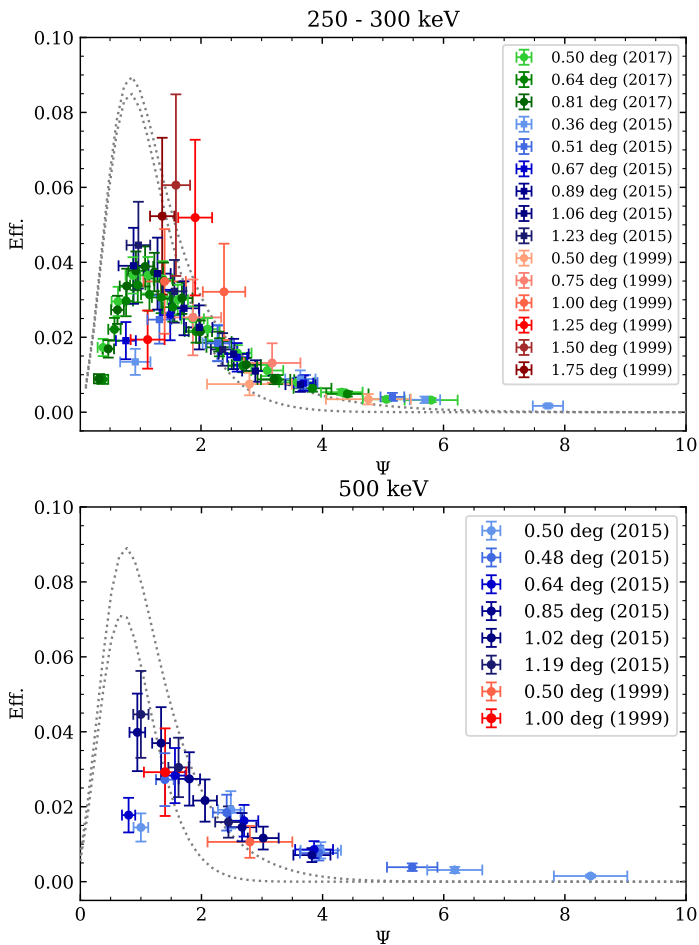


Fig. 2.4 Scattering efficiencies as a function of the scattering angle $\psi = \theta/\theta_0$, for two representative energies of the incident proton beam: 250-300 keV (*upper panel*) and 500 keV (*lower panel*). The blue and green dots stands for measurements on *eROSITA* optics (Diebold et al., 2017, 2015), the red ones for *XMM-Newton* optics (Rasmussen et al., 1999). The grey dashed lines represents the Remizovich scattering efficiencies computed with theoretical values of σ (Eqs. 2.6, 2.8, 2.9), for the incident angles of 0.5° (higher curves) and 1.0° (lower curves). Incidence angles are shown in the legends; errors on *XMM-Newton* scattering angles are at the nominal value of 21 arcmin.

a semi-empirical approach and to determine the parameter σ directly from the data.

We fit the data with the Remizovich formula given in Eq. 2.7, with the integral numerically evaluated, and with σ as a free parameter of the fit. Since the total scattering efficiency is a function of the scattering angle and of the energy at the same time, we could use only the data sets that included both these variables, i.e., data from Diebold et al. (2015). It must be stressed that the model we propose is an empirical best-fit model based on the Remizovich solution and, hence, it depends on the accuracy of the experimental data.

The fit model was computed taking into account the experimental set-up. More in detail, the scattering efficiencies were obtained by the integration of the scattering function (Eq. 2.5) over the solid angle subtended by the detector ($\sim 1.3\mu\text{sr}$) and over the energy interval between the energy of the incoming proton beam and the nominal low energy threshold of the detector of 100 keV. Because the energy of the protons from the laboratory beam is not perfectly monochromatic, but has a Gaussian profile around a nominal value, we considered several input energies within a Gaussian distribution whose center and width are given in Diebold et al. (2015). For each input energy of the Gaussian we produced one output spectrum. The sum of the output spectra gives the overall scattering spectrum per each incident energy. Concerning the energy losses, they were obtained as in Diebold et al. (2015): we fit Gaussians to each incident spectrum and to the corresponding scattering one and computed the difference between their centers.

The goodness of the fit was established using a least-squares minimization without taking into account uncertainties, because points at

large scattering angles, which have smaller errors, would have strongly biased the fit, while we are mainly interested in modelling the data around the peak, where the scattering efficiency is at its maximum. For this purpose, we define a total RMS as the sum of the RMS of the scattering efficiencies (RMS_S) and of the energy losses (RMS_E), normalised to the total efficiency and to the incident energy, respectively:

$$\text{RMS}^2 = \frac{\text{RMS}_S^2}{\eta_{tot}^2} + \frac{\text{RMS}_E^2}{T_0^2} = \frac{\sum_{i=1}^n (S_i - \eta_i)^2}{\eta_{tot}^2} + \frac{\sum_{i=1}^n (E_i - \varepsilon_i)^2}{T_0^2} \quad (2.11)$$

where S_i is the measured scattering efficiency for each i -th scattering angle, η_i is the corresponding efficiency given by the model, η_{tot} is the total scattering efficiency (Eq. 2.7), E_i is the experimental energy loss, ε_i is the energy loss given by the model, and T_0 is the energy of the incident beam. To compute the errors on the parameter σ , we produced 1000 Monte Carlo simulations of the scattering and energy loss distributions per each data set, sorting the values from Gaussian distributions whose means and widths were equal to the data and their relative errors, respectively. We fit every simulated data set with Eq. 2.7, assuming errors on σ at the 95% confidence interval.

The best-fit values of σ as a function of input angle and energy are reported in Tab. 2.2, together with the RMSs, and shown in Fig. 2.5.

2.3.1 Results of the fit and discussion

The model is always in good agreement with the experimental scattering efficiencies, but it is not with the energy losses, which exhibit a small consistency only for the lowest incident energy (250 keV). Fig. 2.6

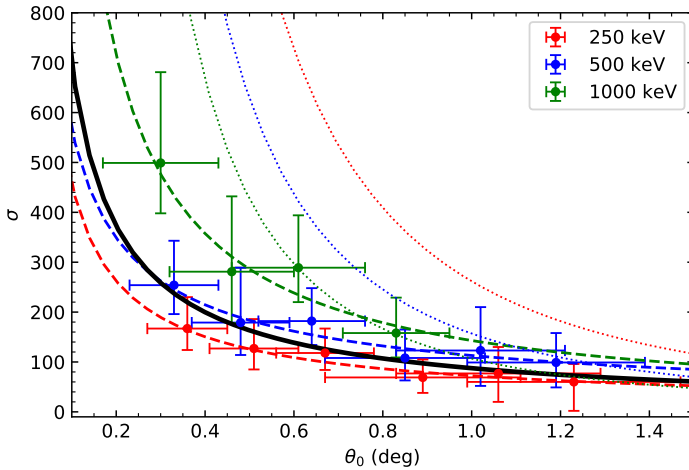


Fig. 2.5 Values of σ derived from the fit as a function of the incidence angle θ_0 , for 250 keV (red), 500 keV (blue) and 1 MeV (green), error bars on the values of σ at 95%. The dashed thick lines represent the best-fit curve for each energy, while the solid *black* line stands for the best-fit curve of all the values of σ . For comparison, also the theoretical values of σ (Eq. 2.6) for the three energies are reported (dotted thin lines).

shows one representative example, at 250 keV, for an incidence angle of 0.36° . The whole sample can be viewed in Appendix A.

Overall, the fit is mainly driven by the scattering efficiencies, while the energy loss distributions seem to contribute very weakly. The angular scattering distributions appear always well modelled by the Remizovich function and have lower RMS values in most of the cases. We note that the flatness of the energy loss distributions might be also due to systematics affecting all the experimental data, especially those at lower incident angles. A quantification of these systematic effects,

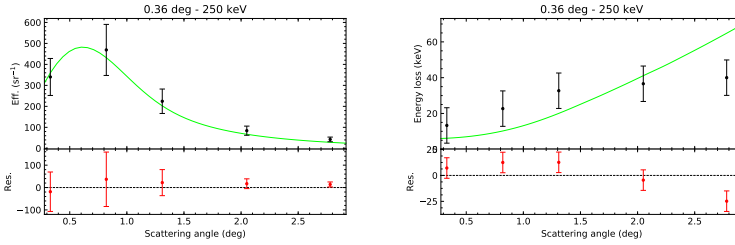


Fig. 2.6 Scattering efficiency (*left panel*) and energy loss (*right panel*) distributions as a function of the scattering angle, for the incidence angle of 0.36° and the incident energy at 250 keV, fit with the Remizovich model in non-elastic approximation. *Bottom panels*: residuals of the fit.

however, is not easy. Besides, the higher is the energy of the impacting beam, the higher is its penetration power inside the material, so that an interaction with the substrate, that would need a more complex treatment, cannot be entirely excluded (see below).

The values of σ show a clear trend with respect to the incidence angle θ_0 (Fig. 2.5), that we tried to describe analytically using a power law $\sigma \propto A\theta_0^{-\alpha}$. Results of the fits are reported in Tab. 2.3. We also note that, even if a systematic trend with the energy is visible, the σ relative to the same incidence angle are generally consistent with each other (apart from a few points), as well as the best-fit parameters shown in Tab. 2.3. We then fit the σ all together with the same power law, obtaining an index value of $\alpha = -(0.9 \pm 0.3)$. This is different from what is stated by Remizovich et al. (1980), for which $\sigma \propto \theta_0^{-2}$ (see Eq. 2.6). Also the trend of the parameter σ with energy is different from Remizovich et al. (1980), where an inverse and stronger dependence

on the energy of the incoming beam is expected: at lower energies correspond highest values of sigma (cfr. Fig. 2.5). We argue that some of the initial assumptions in treating this problem analytically might not fully hold, though we cannot still claim a complete rule-out of the model as more data are necessary to significantly diminish the uncertainty on this parameter.

The gold coating of the *eROSITA* mirrors is tens of nm thick (Merloni et al., 2012). For the energies under consideration, the mean penetration length of protons is of the order of $\sim 10^1-10^{-2}$ nm, depending on the energy of the incident beam. It is possible, then, that some of the incident protons pass through the gold layer and are scattered by the underlying nickel lattice. This led us to repeat the calculations by substituting density, range, stopping power and atomic number of gold with the ones of nickel. Nevertheless, the values of σ found for the nickel ranged from 500 to 40, perfectly consistent with the ones found using gold, so that no significant improvement was obtained. Our conclusion is that either the model is weakly dependent on the choice between the two metals or there is a more complex cumulative effect due to the presence of the double layer.

We also considered a potential deposit of water on the reflecting surface. Indeed, water molecules can be trapped within the superficial layers of the lattice, altering the scattering properties of the medium. A computation of the expected σ for water resulted in smaller values than the best-fit ones, assuring that, if present, the contribute of water deposits may be consider negligible. A more detailed analysis, comprehensive of all the layers or materials of the mirroring surface, is far beyond the goals of this work.

We also attempted to fit separately the scattering efficiencies and the energy loss distributions, but the two sets of fits returned different values of σ , not always consistent with each other. Moreover, the σ obtained from the scattering efficiency were systematically lower and flatter than those in Tab. 2.2, when plotted as a function of the incidence angle, while those from the energy were systematically higher and steeper. This confirms that the two distribution must be fit simultaneously to have consistent values of σ .

2.3.2 Comprehensive analysis of all the data sets

To fully test the validity of the model, we applied it to the other data sets (Diebold et al., 2017; Rasmussen et al., 1999) that could not be fit due to their lack of any energy loss information. We proceeded in two different ways:

- i) We computed the expected scattering probability distributions for the experimental measurements of Diebold et al. (2017) and Rasmussen et al. (1999), using the results of Table 2.2, and compared it to the data. Fig. 2.7 shows the over plot of the experimental measurements on *eROSITA* sample (Diebold et al., 2017) with the model computed with the best-fit power law value of σ . In the case of scattering along the incident direction (on-axis configuration), the scattering efficiency curve for the smallest incidence angle of 0.5° is noticeably underestimated in the peak, while the curves for the other two incidence angles of 0.64° and 0.81° are closer to the data, though they do not perfectly reproduce the experimental trend. However, if we consider the maximum and the minimum

of the expected scattering efficiency distributions (coloured area in Fig. 2.7), resulting by the maximum and minimum error on the parameter σ , then the data can be considered acceptably well modelled, especially at the peaks, even though the spread in efficiency is so high that it prevents any more precise evaluation. For the lateral scattering (off-axis configuration, with an azimuthal angle of $\sim 2^\circ$), instead, the expected scattering efficiencies are slightly overestimated in the peak, while the tails are underestimated (Fig. 2.7, bottom right panel). A correct modelling of the peak, rather than of the tail of the distribution, is essential to predict the expected flux of proton funnelled through the X-ray optics. For the first time, this semi-empirical approach is the closest to the experimental data in giving a correct modelling of the peak. We remark here that having a larger extent of experimental data, i.e. more data points per set, covering wider angular and energetic ranges, remains necessary for better assessing the experimental value of σ .

For completeness, we took into account also the measurements on *XMM-Newton* mirrors (Fig. 2.8), though the paucity of data does not really allow us to put tighter constraints. In this case, the model is not consistent with the data, since the peaks of the distributions are always shifted towards lower scattering angles, as we already noticed when comparing these data with the *eROSITA* sets (cfr. Fig. 2.4).

- ii) Since the fit is weakly dependent on the energy losses, we directly fit the data of Diebold et al. (2017), without accounting for them.

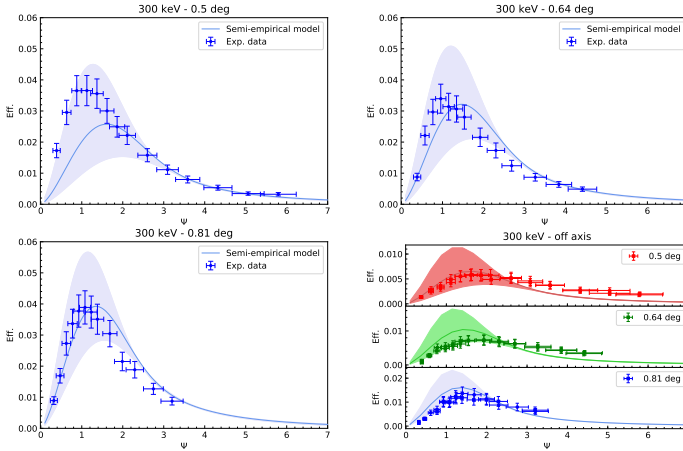


Fig. 2.7 Data and model for the scattering efficiencies at 300 keV (Diebold et al., 2017). The solid line corresponds to the model obtained from the best-fit value of the parameter σ , the coloured area to the maximum and minimum of the distribution, according to the error on σ (errors at 2.7σ). The bottom right panel shows the same comparison for the off-axis data.

However, the on-axis measurements resulted on the whole in smaller values than the previous ones and the values of σ for the on-axis and off-axis configurations are not consistent with each other (Fig. 2.9). This stresses once again that the energy losses are necessary to constrain the fit.

Overall, the consistency of almost all the σ of Tab. 2.2, regardless of the initial energy, leads to the hypothesis that the scattering efficiency is not dependent upon the energy of the impinging proton beam. To verify this assumption, we sort all the data simply by the incidence angle, irrespective of the energies. As a matter of fact, all the scattering

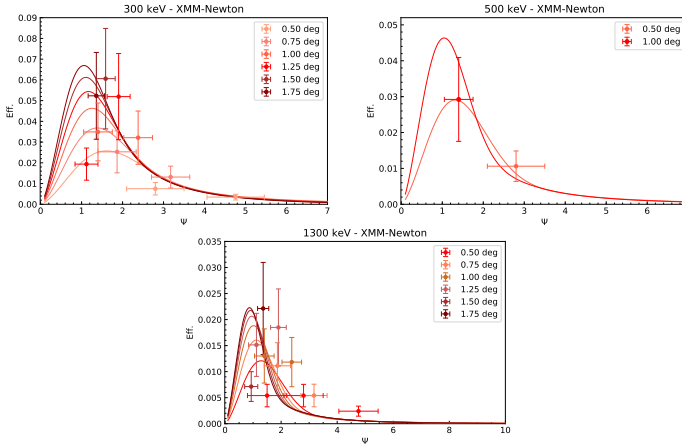


Fig. 2.8 Data and scattering efficiency distributions predicted by the model with the best-fit value of σ for the *XMM-Newton* mirror sample (Rasmussen et al., 1999).

efficiencies appear consistent with each other, as shown in Fig. 2.10, where we also display the efficiency curves for the best-fit values of σ for the two lowest incident energies of 250 keV (red) and 500 keV (blue), those energies being more relevant for our work. The coloured areas correspond to the maximum and minimum scattering efficiencies computed from the errors on the best-fit σ .

Finally, one minor concern regards the microroughness of mirroring surfaces, which is already known to be responsible of reducing the reflection efficiency of X-ray photons, by causing scattering in other directions than the incident one (Spiga et al., 2007). The same effect might apply to protons as well, although the higher mass of protons suggests that almost all the impinging particles penetrate the surface, instead of being scattered in the surrounding directions. The lack of

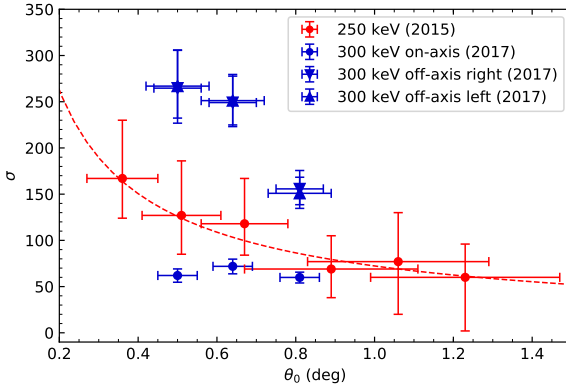


Fig. 2.9 Best-fit values of σ of the 2017 data sets, compared with the previous values for the incident energy of 250 keV (see Fig. 2.5). Error bars on the values of σ at 95%.

any experimental estimates on the angular distribution of sided or back scattered protons does not allow us to investigate this issue any further.

2.4 Summary

In this work we tested all the available experimental measurements of proton scattering efficiency at grazing incidence from X-ray mirrors with the analytic model developed by Remizovich et al. (1980) under the non-elastic approximation. We came up with a semi-empirical model based on the Remizovich formula, where the parameter σ is directly determined by fitting the only experimental data set with energy loss measurements. The main results can be summarized as follows:

- all the *eROSITA* data sets can be modelled with the same value of the parameter σ , which can be considered independent from the

energy of the incident protons, even if a systematic trend with energy is observed;

- there is a clear dependence of the parameter σ over the incidence angle θ_0 , well reproduced by a power law with $\sigma \propto \theta_0^{-1}$. This is in contrast to what is stated by Remizovich et al. (1980);
- the peaks and the tails of the scattering efficiency are acceptably well modelled. We remind here that a correct evaluation of the scattering efficiency at its peak is crucial to estimate the SP flux expected at the focal plane of every X-ray mission with grazing incidence optics;
- although the energy loss distributions drive marginally the fit, they are necessary in modelling the data and in returning consistent values of the parameter σ .

The semi-empirical model we propose is strictly limited to the actual experimental data sets. For instance, we cannot verify the independence of the angular scattering efficiency distribution from the incident energy also at energies below 250 keV, which are especially relevant for the future X-ray mission *Athena*. Simulations by Lotti et al. (2018) show, indeed, that SPs with energies between 1 and 150 keV produce significant background signals in the working range of the instruments at the focal plane. To overcome this weakness of the model and to better estimate the parameter σ , further laboratory activities are necessary, as the one presented in Chapter 3, performed on a Silicon Pore Optics sample.

Table 2.2 Best-fit values of the parameter σ and corresponding values of RMS of the scattering efficiency (RMS_S) and energy loss (RMS_E) distributions, with the number of data points (n).

	θ_0 ($^\circ$)	σ	$\text{RMS}_S(n)$	$\text{RMS}_E(n)$
250 keV	0.36	167^{+63}_{-43}	23(5)	14(5)
	0.51	127^{+59}_{-42}	11(4)	14(4)
	0.67	118^{+49}_{-34}	7(4)	17(4)
	0.89	69^{+36}_{-31}	16(4)	24(4)
	1.06	77^{+53}_{-57}	10(3)	26(3)
	1.23	60^{+36}_{-58}	12(3)	28(3)
500 keV	0.33	254^{+89}_{-58}	52(5)	18(5)
	0.48	179^{+110}_{-65}	10(4)	17(4)
	0.64	182^{+66}_{-48}	12(4)	21(4)
	0.85	108^{+57}_{-45}	15(4)	19(4)
	1.02	123^{+87}_{-71}	10(3)	22(3)
	1.19	99^{+59}_{-50}	13(3)	23(3)
1 MeV	0.30	499^{+182}_{-101}	71(4)	19(4)
	0.46	281^{+151}_{-103}	18(4)	20(4)
	0.61	289^{+105}_{-69}	14(4)	25(4)
	0.83	158^{+71}_{-49}	7(3)	25(3)

Table 2.3 Best-fit values of the σ parameters, fit with a power law of the type $f(x) = Ax^{-\alpha}$, and χ^2 values at 2.7σ level.

T_0 (keV)	A	α	χ^2 (d.o.f.)
250 keV	73 ± 34	0.8 ± 0.4	0.3(5)
500 keV	113 ± 55	0.7 ± 0.4	0.4(5)
1 MeV	143 ± 60	1.0 ± 0.5	0.4(3)
All	88 ± 28	0.9 ± 0.3	9(15)

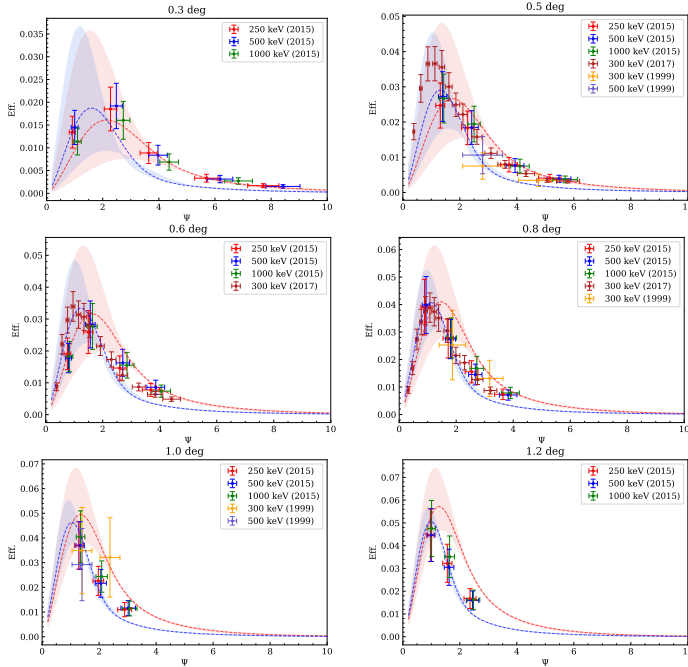


Fig. 2.10 Scattering efficiencies of all the available data sets as a function of the scattering angles Ψ for different incidence angles. Dashed curve represents the Remizovich functions computed with the best-fit value of σ for 250 keV (red) and 500 keV (blue), with coloured area corresponding the maximum and minimum scattering efficiencies as from the 2.7σ confidence errors on σ . Errors on *XMM-Newton* efficiencies are at $\sim 40\%$.

Chapter 3

Experimental Activity

The semi-empirical model presented in Chapter 2 was specifically derived by experimental measurements of scattering of low energy protons at grazing incidence from an *eROSITA* mirror sample. Hence, the best-fit value of the parameter σ is supposed to be valid only for golden reflecting surfaces with a thickness of several tens of nm.

To correctly estimate the soft proton flux expected at the focal plane of *Athena*, specific experimental measurements on Silicon Pore Optics (SPO) are required. Such measurements were performed within the EXACRAD (Experimental Evaluation of *Athena* Charged Particle Background from Secondary Radiation and Scattering in Optics) project, funded by ESA and carried out by the High-Energy Astrophysics group of the University of Tübingen.

3.1 Experimental set-up

The experimental campaigns were conducted at the 2.5 MV Van de Graaff accelerator at the Goethe University (Riedberg Campus) in Frankfurt am Main. The setup of the beamline, similar to that of Diebold et al. (2017, 2015), is given in Figs. 3.1 and 3.2.

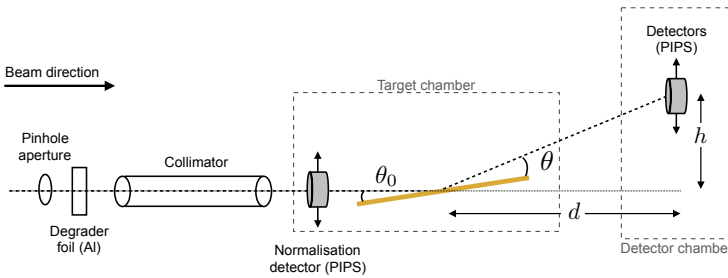


Fig. 3.1 Schematic drawing (not in scale) of the beamline set-up. The proton beam enters the set-up from the left-hand side. It encounters the pinhole aperture (1 mm in diameter), the Al degrader foil (0.002 mm thick) and the collimator. Inside the target chamber, the normalisation detector can be lowered down to intercept the beam for the normalisation measurements. If the normalisation detector is not in the line of the beam, then protons are reflected from the SPO sample (in yellow) towards the detector chamber, where they hit the central and lateral detectors. The incident angle θ_0 between the line of the beam and the mirror varies with the inclination of the target plate, while the scattering angle θ between the mirror and the detectors in the detector chamber varies with their height h . The distance d between the target plate and the vertical axis of the detectors is fixed to 942 mm.

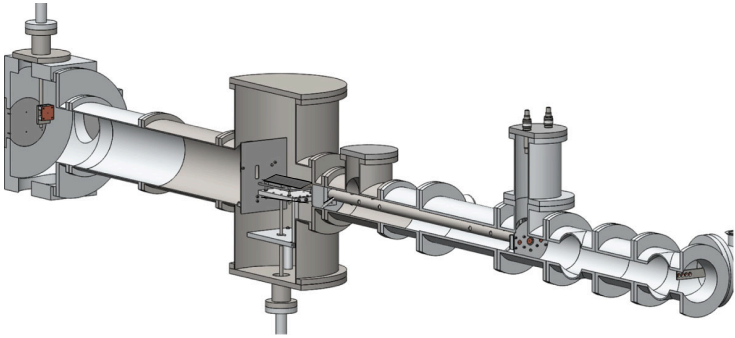


Fig. 3.2 A CAD model of the beamline (same as Diebold et al., 2015). The proton beam enters the set-up from the right and moves towards the left. The SPO sample is allocated in the target chamber, while the detector is placed in the chamber at the end of the beamline (detector chamber). A second detector (not shown in the picture) was placed next to the central one, at an angular distance of $\sim 2^\circ$.

3.1.1 Beamline setup

Protons enter the beamline through a copper pinhole aperture of the diameter of 1 mm, which reduces the size of the incoming beam to prevent pile-up and to maintain reasonable rates on the detectors. Successively, the beam goes through a 0.002 mm-thick aluminium foil, which degrades the incoming beam energy below the lower limit of the accelerator. The degraded beam enters, at this point, a 78 cm-long collimator, which directs part of the widened beam directly to the target. Two further apertures are positioned at the entrance and at the exit of the collimator, respectively, the former of 1 mm in diameter and the latter of 0.7 mm. This combination limits the maximum opening angle to 0.36° . The apertures are supported in their position by 2 mm-thick

aluminum plates, which absorb any proton of the degraded beam not entering the apertures and being scattered by the inner walls of the collimator and of the beamline itself.

The target – a 110 mm-long single silicon wafer, 0.775 mm thick, grooved in the bottom, and coated on top with a 10 nm of iridium and 7 nm of silicon carbide – is located inside an apposite chamber (hereafter called target chamber) and mounted on a tiltable plate. The height of the target can be adjusted by a set of screws underneath the plate. A linear manipulator is used to change the inclination of the plate, i.e., the incident angle (θ_0). The pivoting point is several centimeters below the line of the beam, so that the target can be completely removed from the course of beam, allowing for a determination of the primary beam position on the detector plane. The manipulator is set below the target chamber and, hence, can be easily accessed from the outside when the system is on vacuum.

Between the exit of the collimator and the target plate, a Passivated Implanted Planar Silicon (PIPS) detector¹ is mounted on a push-pull manipulator, at the same height of the beamline. This detector is used to register the amount of flux of the beam impinging on the target, useful to have normalisation measurements. This detector will be called hereafter ‘normalisation detector’. The push-pull manipulator permits a fast removal of the detector, guaranteeing a measure of the impinging proton flux (Φ_{inc} , Eq. 3.2) for each measure of the scattered beam (see Sect. 3.2 on the need of having frequent normalisation measurements). An aluminium blind with an aperture of 3 mm is set on top of the

¹The PIPS detectors used in this experiment have a nominal depletion region of 0.1 mm and a lower energy threshold of a few tens of keV.

normalisation detector to avoid saturation. Lastly, downstream of the target chamber, a thick aluminum sheet, with a slit of 3 cm height and 1 cm width, is installed a few centimeters after the target plate. This window let pass only the protons on the line of the beam, while the sheet absorbs all the ones that have been scattered by the inner walls or by other elements in the target chamber.

At the end of the beamline, a second chamber (hereafter detector chamber) hosts two more PIPS detectors, called ‘central detector’ and ‘lateral detector’, respectively, used to register the on-axis e off-axis fluxes ($\Phi_{\text{scat}}(\theta_0, \theta, \phi)$, Eq. 3.2) of the beam scattered by the target. They are mounted on a second linear manipulator, which allows for a vertical sampling of the scattered beam. The distance between the center of the target plate and the detection plane is 942 mm. The central detector is aligned with the beam direction, while the lateral detector is set on the left, at an azimuthal angle of $1.97^\circ \pm 0.13^\circ$. On top of each detector there is a blind with an aperture of a diameter of 1 mm for the central detectors and of 3 mm for the lateral detector. They reduce the solid angle of the detectors with respect to the mirror center to about 8×10^{-7} sr and 2×10^{-5} sr, respectively (Eq. 3.6, Sect. 3.2).

3.1.2 Data acquisition chain

The pulse signal produced by the PIPS is amplified and digitalised through several analogical/digital electronic components. A flow chart is given in Fig. 3.3.

The PIPS detectors produce a pulse with an amplitude proportional to the energy of the incident particle. The pulse signal from each PIPS goes through its own pre-amplifier and amplifier and then it is digi-

talised by the Analog to Digital Converter (ADC). The ADC receive the continuous signals (from 0 to ~ 10 V) from the three channels – one for each detector – and convert them into discrete signals, distributing them into 8192 bins, with a resolution of 1.22 mV. The digitised signals are then passed to the histogramming memory, which produces an histogram for each channel. Once the measurement is done, the histograms are read out by the CAMAC module and are transferred to a computer, which acquires and stores them to raw-data files.

The process of digitalisation of the data within the ADC takes a certain time (fractions of second), so that if a new signal comes within that time, it is not registered. To account for this dead-time, a pulse generator, which generates pulses at a fixed frequency, is connected to the ADC and to a scaler, which counts the number of pulses produced by the pulse generator during the acquisition time. The scaler is also fed to the CAMAC control module. The difference between the readings of the counts from the ADC and those from the scaler gives the dead-time correction factor (see Eq. 3.4, Sect. 3.2.1). The pulse generator fed to the ADC constitutes another channel, so that the whole acquisition system consists of four channels, all working simultaneously, plus the scaler.

3.1.3 Alignment and angular calibration

The alignment of the pinhole aperture and of the slits was done by using a telescope previously aligned with the exit of the accelerator.

A 520 nm laser, which can be operated using pulse-width-modulation (PWM), was employed to align the detectors and to perform the angular calibration. The laser was set right after the pinhole aperture and went

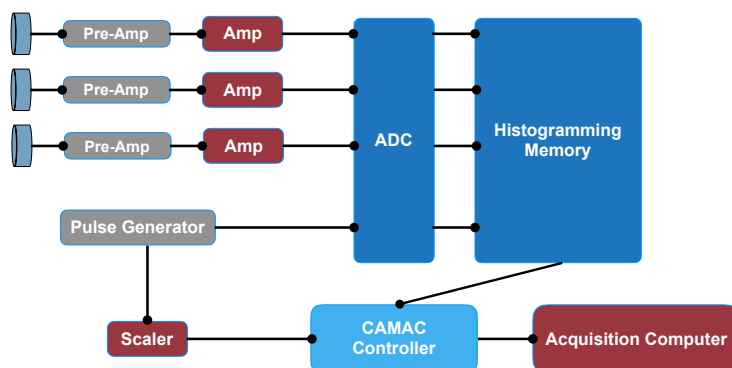


Fig. 3.3 Data flow of the electronic chain for the acquisition of the experimental data. The analogical signal from the PIPS detectors first goes through a pre-amplifier and an amplifier, then it is converted into a digital signal by the ADC, and finally it is stored in the histogramming memory. Contemporarily, a pulse generator sends signals at a fixed frequency to the ADC and to a scaler. The digitised signals are read out by a CAMAC controller unit, which transmits them to a computer once the measure is finished.

through all the slits. When the target plate was down, the laser reached the central detector in the detector chamber. In this way, we were able to establish the zero of the beamline, corresponding to $\theta = 0^\circ$. This measurement gave also the vertical offset on the linear manipulator of the central/lateral detectors.

To calibrate the incident and scattering angles, we used the property of the mirror target to reflect optical light. Hence, we rose the target plate, using its own manipulator, until the light was blocked. Then, we rose the central detector till the laser beam was detected again. Assuming a specular reflection, the incident angle is given by:

$$\theta_0 = \frac{\theta}{2} \quad (3.1)$$

This operation was repeated several time, so that we ended up with different angles corresponding to different readings on the linear manipulator of the target plate. The incident angle can then be determined with a simple linear interpolation.

3.2 Efficiency definition and normalisation measurement

In the laboratory system of reference, the scattering efficiency per unit solid angle can be defined as:

$$\eta(\theta_0, \theta, \phi) = \frac{1}{\Omega(\theta)} \frac{\Phi_{\text{scat}}(\theta_0, \theta, \phi)}{\Phi_{\text{inc}}} \quad (3.2)$$

where θ_0 is the incident angle, θ and ϕ are the polar and azimuthal scattering angles, Φ_{scat} and Φ_{inc} are the scattered and incident proton count rates, and $\Omega(\theta)$ is the solid angle seen by the detector. The geometric scheme of the system is given in Figs. 3.1, 3.4.

The count rate of the scattered particles is given by the number of protons N_{scat} scattered by the SPO sample reaching the detectors in the detector chamber divided by the integration time Δt_{scat} . In a similar way, the count rate of the incident particles is given by the number of protons N_{inc} intercepted by the normalisation detector in the mirror chamber divided by the integration time Δt_{inc} . The number of counts of incident and scattered protons, N_{inc} and N_{scat} , is obtained by integrating the ADC histograms. This number must be corrected for the dead-time of the ADC, as mentioned in Sect. 3.1.2, so that the effective count rates can be expressed as:

$$\Phi_{scat}(\theta_0, \theta, \phi) = \alpha \frac{N_{scat}(\theta_0, \theta, \phi)}{\Delta t_{scat}}, \quad \Phi_{inc} = \alpha \frac{N_{inc}}{\Delta t_{inc}} \quad (3.3)$$

with the correction factor α given by:

$$\alpha = \frac{N_{scaler}}{(N_{pulsers})_{ADC}} \quad (3.4)$$

where N_{scaler} is the number of counts from the pulse generator as read out from the scaler fed to the CAMAC controller module and $(N_{pulsers})_{ADC}$ is the number of pulses from the pulse generator as read out from the ADC (see Fig. 3.3).

For an ideal incoming proton beam, the number of incident particles N_{inc} is constant in time. However, the beam exiting the Van de Graaff

accelerator was not stable, with fluctuations in the direction of the beamline varying in a time range from a few to several tens of minutes. This made necessary to take normalisation measurements before and after each scattering measurement and average them for each scattering data point, so that:

$$\frac{N_{\text{inc}}}{\Delta t_{\text{inc}}} = \frac{1}{2} \left(\frac{N_{\text{inc},1}}{\Delta t_{\text{inc},1}} + \frac{N_{\text{inc},2}}{\Delta t_{\text{inc},2}} \right) \quad (3.5)$$

where $N_{\text{inc},1}$ and $N_{\text{inc},2}$ are the counts in two consecutive normalisation measurements with integration times $\Delta t_{\text{inc},1}$ and $\Delta t_{\text{inc},2}$, respectively.

The solid angle $\Omega(\theta)$ (see Fig. 3.4) seen by the detector can be computed as:

$$\Omega(\theta) = 2\pi \left(1 - \cos \left(\frac{\theta_{\text{max}} - \theta_{\text{min}}}{2} \right) \right) \quad (3.6)$$

with:

$$\theta_{\text{min}} = \tan^{-1} \left(\frac{h-r}{d} \right) - \theta_0 \quad \theta_{\text{max}} = \tan^{-1} \left(\frac{h+r}{d} \right) - \theta_0 \quad (3.7)$$

where d is the distance between the center of the target and the detection plane (942 mm), h is the height of the detector with respect to the zero of the beamline, and r is the radius of the aperture in front of the detector (0.5 mm for the central detector and 2.5 mm for the lateral one).

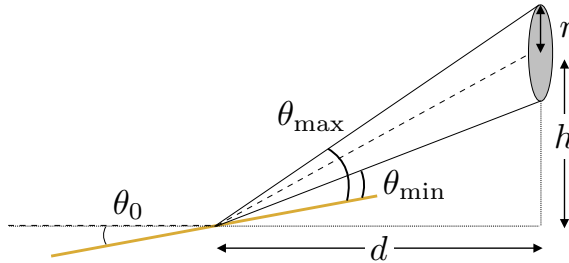


Fig. 3.4 Geometric scheme of the system, useful to compute the solid angle seen by the detector. d is the distance between the center of the target and the position of the detector projected on the beamline, h is the height of the detector with respect to the beamline, and r is the radius of the aperture in front of the detector. θ_{\max} and θ_{\min} are the angles subtended by the upper and lower edges of the aperture, respectively.

3.2.1 Uncertainty calculation

The uncertainty on the scattering angle is given by three main contributions: the error on the calculation of the scattering angle itself ($\delta\theta$), the error of the detector aperture (δr), and the error due to indeterminate position of the impact point of the beam on the mirror surface ($\delta\xi$). Since these contributes are independent from each other, the total uncertainty is:

$$\sigma_{\theta} = \sqrt{(\delta\theta)^2 + (\delta r)^2 + (\delta\xi)^2} \quad (3.8)$$

Let's examine these terms one by one. According to the geometry of the system (Fig. 3.1, 3.4), the scattering angle is given by:

$$\theta = \tan^{-1} \left(\frac{h}{d} \right) - \theta_0 \quad (3.9)$$

Hence, the corresponding error is simply:

$$\delta\theta = \frac{\partial\theta}{\partial h} \delta h = \frac{\delta h}{d} \frac{1}{1 + \left(\frac{h}{d}\right)^2} \quad (3.10)$$

where δh is the error on the reading of the detector manipulator (0.5 mm).

The error due to the detector aperture is simply given by:

$$\delta r = \frac{\theta_{\max} - \theta_{\min}}{2} \quad (3.11)$$

with θ_{\max} and θ_{\min} as in Eq. 3.7.

To compute the error due to the elongation of the beam spot over the target surface, we estimated the semi-major ax of the projected ellipse, which resulted 134 mm long, for the lowest incident angle (0.6°), and comparable, or even smaller than the mirror length m_l of 110 mm for the higher incident angles. We decide to adopt the whole mirror length, though we are aware that this uncertainty might be responsible for systematics in the data, especially at the lowest incident angle. With respect to the geometry scheme of Fig. 3.5, we can define:

$$\delta\xi = \xi_2 - \xi_1 \quad (3.12)$$

where:

$$\xi_1 = \tan^{-1} \left(\frac{h-r}{d} \right) \quad (3.13)$$

and

$$\xi_2 = \tan^{-1} \left(\frac{h+r-m_l \sin \theta_0}{\Delta d} \right) \quad (3.14)$$

with $\Delta d = d - m_l \cos \theta_0$.

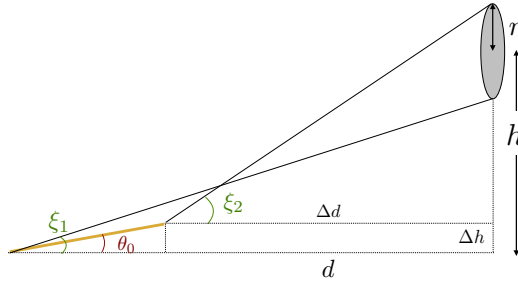


Fig. 3.5 Geometric sketch of the system, useful to compute the uncertainty due the elongation of the beam spot on the target. ξ_1 and ξ_2 are the angles subtended by the heights of the detector with respect to the upper and lower edges of the aperture in front of the detector itself.

Also the uncertainty on the incident angle θ_0 (Eq. 3.1) is mainly dominated by the dimension of the aperture on the central detector and by the length of the target. It resulted in 0.1° for all the chosen scattering angles.

Concerning the uncertainty on the scattering efficiency, it is mainly given by the intrinsic fluctuation of the proton beam (see also Sec. 3.2). Minor contributions are due to the count statistics and to the error on the solid angle $\Omega(\theta)$. The sum of this contributions results in statistical

fluctuations of $\pm 20\%$ on the scattering efficiency:

$$\sigma_\eta = 20\% \eta(\theta_0, \theta, \phi) \quad (3.15)$$

3.3 Results on the scattering efficiency

We measured the scattering efficiency at two different energies (hereafter referred to as high- and low-energy data sets, respectively) and at four different incident angles: 0.6° , 0.8° , 1.0° , and 1.2° . Each data set consists of scattering efficiencies acquired both with the central (on-axis configuration) and lateral (off-axis configuration) detectors. Results are shown in Figs. 3.7 and 3.6, where the scattering efficiencies are normalised to the square of the incident angle (cfr. Eq. 2.10 in Sect. 2.2) and are displayed as a function of the scattering angle divided by the incident one ($\psi = \theta/\theta_0$, cfr. Eq. 2.1 in Sect. 2.1).

For the high-energy data set (Fig. 3.7), we used a beam at ~ 590 keV from the accelerator, which was degraded by the Al foil down to 471 ± 25 keV. For the low-energy data set (Fig. 3.6), the beam exited the accelerator with an energy of ~ 340 keV, which reduced to 172 ± 30 keV after the Al foil. The value of the incident energy was determined by simulations with the software TRIM² (TRansport of Ions in Matter, Ziegler et al., 2010), already validated in Diebold et al. (2015).

The general trend is in agreement with the previous experimental results on the *eROSITA* mirror sample (see below) and with the semi-empirical model based on Remizovich et al. (1980) that we developed

²The TRIM code is one of the SRIM (Stopping and Range of Ions in Solids) group of programs, available at <http://www.srim.org/index.htm#HOMETOP>.

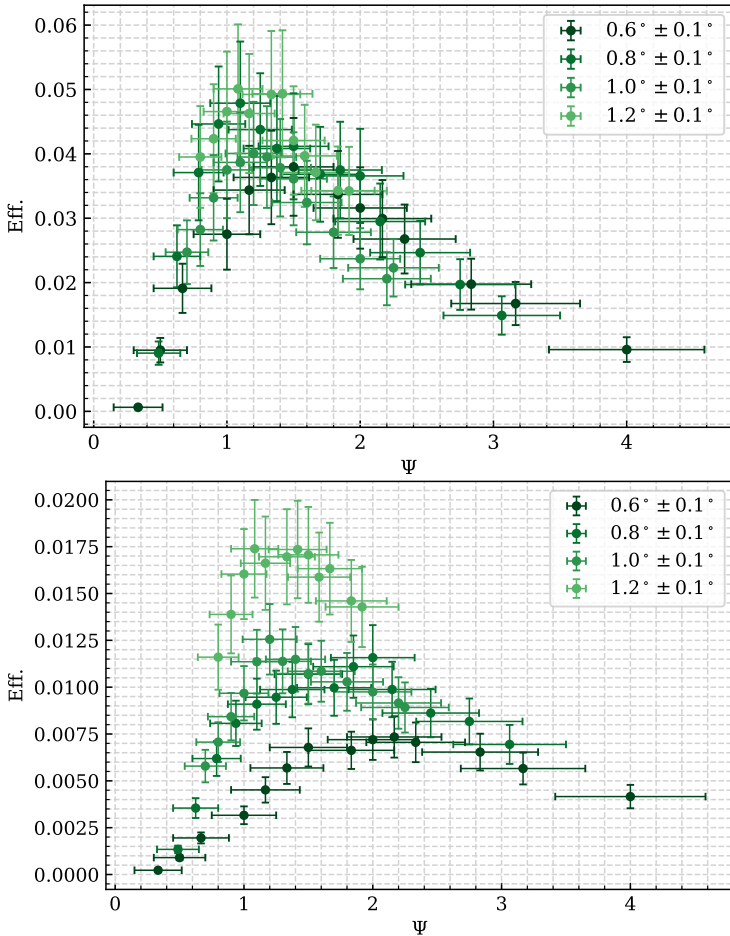


Fig. 3.6 Scattering efficiencies of the low-energy data set as a function of the scattering angle, for incident angles of 0.6° , 0.8° , 1.0° and 1.2° , for the on-axis (*top panel*) and off-axis (*bottom panel*) configurations. Energy of the beam of 172 ± 30 keV.

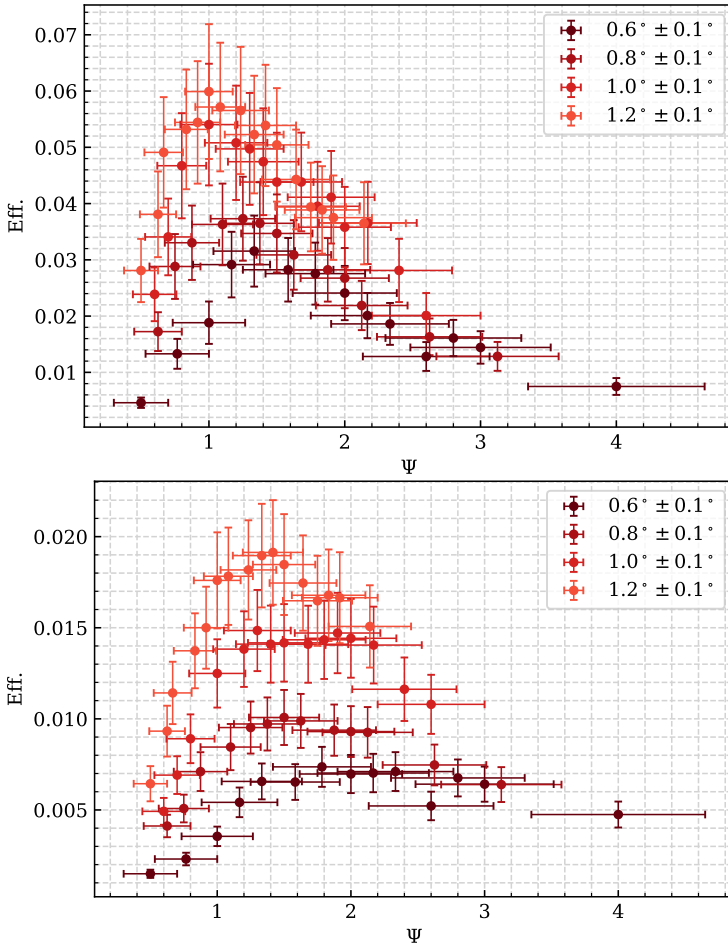


Fig. 3.7 Scattering efficiencies of the high-energy data set as a function of the scattering angle, for incident angles of 0.6° , 0.8° , 1.0° and 1.2° , for the on-axis (*top panel*) and off-axis (*bottom panel*) configurations. Energy of the beam of 471 ± 25 keV.

and discussed in Chapter 2. As expected, the on-axis scattering efficiencies peak at the specular angle ($\psi \simeq 1$) and are consistent with each other within the uncertainties. However, a higher spread is observed for the high-energy on-axis data set (Fig. 3.7, top panel), with efficiencies ranging from 0.03 to 0.07 at the peak of the distribution. Also the off-axis data show a significant spread, which is expected in this case.

Overall, the maximum scattering efficiency values (normalised to the square of the incident angles) are ~ 0.07 and ~ 0.02 for the on-axis and off-axis configurations, respectively, with the low-energy data set showing slightly smaller efficiencies than the high-energy one.

3.3.1 Comparison with the *eROSITA* measurements

Fig. 3.8 shows the *eROSITA* measurements (Diebold et al., 2017, 2015, cfr. Sect. 2.2) overlapped to the SPO data, for both the energies and the on-axis and off-axis configurations. Though the SPO efficiencies are systematically higher than the *eROSITA* data, they are consistent within the error bars.

Due to this consistency, it seemed natural to apply the semi-empirical model developed in Sect. 2.3, with the best-fit value of σ as in Sect. 2.3.1, to reproduce the scattering efficiencies of SPO. Fig. 3.9 compares the semi-empirical model with the scattering efficiency of SPO, for all the data sets. A more accurate representation is given in Appendix B, where each curve is plotted with the upper and lower errors at 2.7σ confidence level.

Overall, the model well reproduces the scattering efficiency of the low-energy data set, but overestimates the efficiency of the high-energy data set of ~ 1.5 times. From a closer look at the low-energy

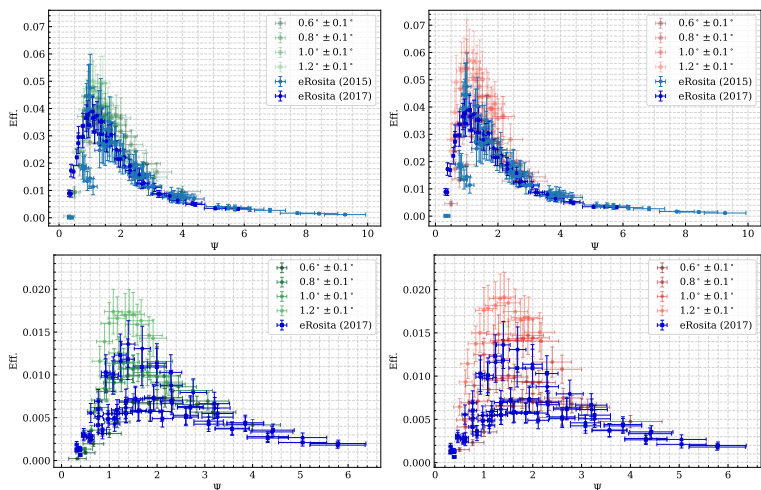


Fig. 3.8 Comparison of the *eROSITA* scattering efficiencies (blue dots) with the SPO ones (green dots for the low-energy set and red dots for the high-energy set), for the on-axis (*top panels*) and off-axis (*bottom panels*) data.

data set, the on-axis experimental data are perfectly reproduced by the semi-empirical model for the lower incident angles (0.6° , 0.8°), while the efficiency curve results slightly wider at the peak than the experimental data points for the higher scattering angles (1.0° , 1.2° , see also Fig. B.1). Nevertheless, the value of the efficiency at the peak of the model is always consistent with the experimental one. The trend is inverted for the low-energy off-axis data (cfr. Fig. B.2). The efficiency curves for lowest incident angles (0.6° , 0.8°) are lower and only marginally consistent with the experimental data, the peaks are slightly shifted to lower Ψ and the drops of the curves do not match the experimental points. On the other hand, the efficiency curves for the highest scattering angles (1.0° , 1.2°) match the experimental data points.

Nonetheless, it has to be borne in mind that at this stage we simply overlapped the semi-empirical model to the new SPO experimental data. It is clear that a fit of the SPO data is necessary to determine the appropriate value of σ . We remark, however, that the fit can be performed only if the energy loss data are available.

Lastly, as in Sect. 2.3.2, we grouped the efficiencies of the two data sets by the incident angle, irrespective of the energy of the incident beam. Fig. 3.10 shows that the data are perfectly consistent with each other and with the old *eROSITA* measurements when grouped by the incident angle, without accounting for the energy.

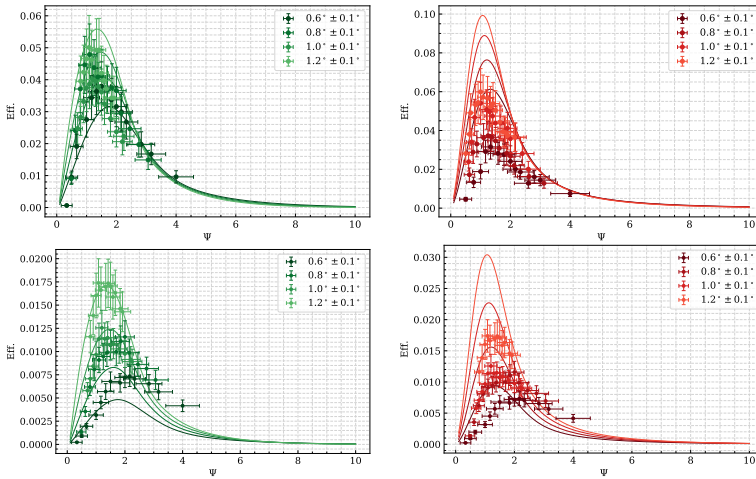


Fig. 3.9 Comparison between the experimental scattering efficiency of SPO (points) and the semi-empirical model developed from *eROSITA* data (solid line), for the low-energy (green) and high-energy (red) data sets and for the on-axis (*top panels*) and off-axis (*bottom panels*) measurements.

3.4 Remarks and future perspectives

Within the EXACRAD project, we measured for the first time the scattering efficiency of a single wafer of SPO hit by low energy protons at grazing incidence. Measurements were performed at two different energies, 471 keV and 172 keV, and at four different incident angles, 0.6° , 0.8° , 1.0° , and 1.2° .

Hereafter some major remarks:

- the scattering efficiencies show the trend expected from Remizovich et al. (1980) and from the experimental data on *eROSITA*

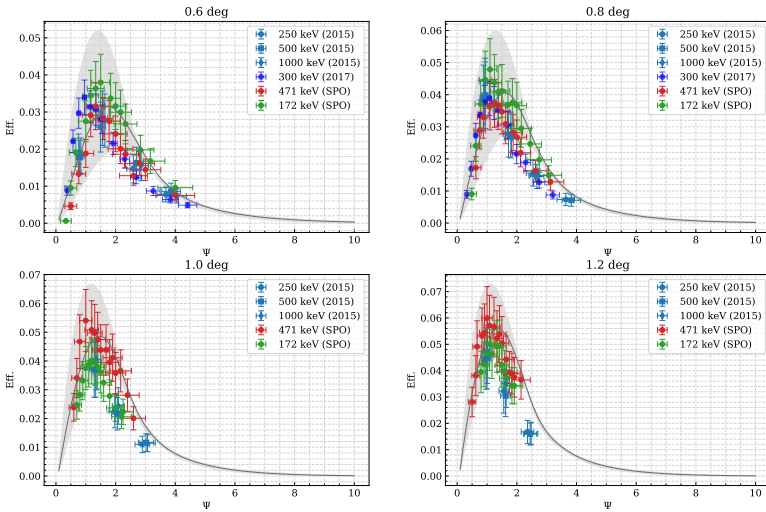


Fig. 3.10 Comparison of the *eROSITA* scattering efficiencies (blue dots) with the SPO ones (red dots for the high-energy set and green dots for the low-energy set) grouped by different incidence angles, irrespective of the energy of the beam. The solid lines stand for the semi-empirical scattering model, with the error on the efficiency given by the coloured area.

(Diebold et al., 2017, 2015). The on-axis data peak close to the specular reflection, while the off-axis data show a peak shifted to higher Ψ ; the off-axis data reach lower efficiencies than the on-axis ones; higher incident angles and higher energies resulted in higher scattering efficiencies;

- the SPO data are generally consistent with the *eROSITA* data, though the high-energy data set show a higher spread in efficiency;

- as for the *eROSITA* data, the scattering efficiency very weakly depends on the energy of the incident beam;
- the semi-empirical model developed from *eROSITA* experimental data is able to acceptably reproduce the low-energy data set, while it results in higher efficiencies for the high-energy data set;
- it is necessary to develop a model specific for the SPO, with the σ derived from a direct fit of the data.

Concerning the last point, the fit can be well constrained only if energy losses measurements are available. Those data can be derived from the raw data, after a proper calibration of the histograms acquired by the computer. Hence, this work could be improved by retrieving the energy loss for each experimental data point and performing the aforementioned fit, following the same approach of Chapter 2.

Chapter 4

Geant4 simulations of *XMM-Newton*/EPIC MOS

After being pseudo-focused by the optics of X-ray telescopes, soft protons (SPs) are funnelled towards the focal plane, where they reach the detectors and produce a signal indistinguishable from the one generated by the X-ray photons (cfr. Chapter 1). Along their path, they interact with all the mechanical components on their trajectory, such as optical filters, shields, etc., so that the final spectrum is altered. The link between SPs entering the optics and the spectrum as read-out from the detectors is given by a specific response matrix for protons.

Response matrices are common tools for X-ray data analysis. A photon response matrix gives the probability that an incoming photon of energy E is detected in the output detector channel PHA . According to the Office of Guest Investigators Program (OGIP) for high-energy astrophysics projects, the format of the matrix must be the Flexible

Image Transport System (FITS), conform to the OGIP Calibration Memo CAL/GEN/92-0021¹. As for a photon response matrix, a proton response matrix must be made of two different files: the ancillary response file (*arf*), containing information on the effective area computed as the product of the telescope grasp, the filter transmission and the probability that an absorbed proton is detected in the detector working energy range; the detector redistribution matrix file (*rmf*) that stores in a 2-d array (energy vs. *PHA* channel) the probability that a proton with energy E_i is detected in the channel *PHA* correspondent to the energy E_0 (Lotti et al., 2018; Mineo et al., 2017). The matrix must be written in units of cm^2 in order to be used within the X-ray analysis software XSPEC (Arnaud, 1996).

In building a proton response matrix, two major steps have to be taken into account:

- the interaction of SPs with the optics, described by the semi-empirical analytical model of Chapter 2, which can be implemented in any ray-tracing code;
- the interaction of SPs with the elements at the focal plane assembly of the telescope, which can be investigated with any platform, software, or tool simulating the passage of particles through matter.

The construction of a specific proton response matrix is one of the activity of the AHEAD2020 (Integrated Activities for the High-Energy Astrophysics Domain)² programme, funded by the Horizon

¹https://heasarc.gsfc.nasa.gov/docs/heasarc/caldb/docs/memos/cal_gen_92_002/cal_gen_92_002.html.

²<https://ahead.iaps.inaf.it/>.

2020 Framework Programme of the European Union. The specific activity consists in a 2-year project to update the proton response matrix of *XMM-Newton* and produce new proton response matrices for *Athena*.

A proton response matrix for *XMM-Newton* was already built by Mineo et al. (2017). Authors implemented a ray-tracing code for the optics, consisting in a Monte Carlo stand-alone code that can simulate the reflection of either photons or protons interacting with the mirror shells. The code was derived from an existing version used for the calibration of the X-ray telescopes *BeppoSAX* (Conti et al., 1994) and *Swift* (Cusumano et al., 2006). It takes into account the geometry of the optics and the baffle, and excludes the reflection from the uncoated back side of the shells. Mineo et al. (2017) used the reflectivity model for protons at grazing incidence proposed by Remizovich et al. (1980) in elastic approximation (see also Firsov, 1958). Recently, the semi-empirical model of Chapter 2 has been implemented, so that the ray-tracing can now be used to simulate the interaction of protons with *XMM-Newton* optics in non-elastic approximation.

The second step needs a more realistic rendering of the focal plane. To this aim, I set-up and performed a simulation of SPs impacting on the focal plane assembly of *XMM-Newton*, using the Monte Carlo-based toolkit Geant4 (GEometry ANd Tracking; Agostinelli et al., 2003; Allison et al., 2006, 2016), as one of the steps for the production of the matrix foreseen in the AHEAD2020 project. In the following sections, I illustrate the geometry and the physics of the simulation, and some preliminary results. It must be kept in mind that this is just a first stage for the production of a proton response matrix. A complete work

will put together the results from the ray-tracing code with a wider sets of Geant4 simulations, comprehensive of different energies and grazing incidence angles.

4.1 *XMM-Newton* in a nutshell

The X-ray Multi-Mirror Mission (*XMM-Newton*, Jansen et al., 2001) is the largest X-ray observatory of the European Space Agency (ESA). It was launched on 1999 December 10, inside the Horizon 2000 Science Program. It consists of three single telescopes, with 58 Wolter type-I mirror shells nested in a coaxial and confocal configuration each, and an optical/UV monitor, mounted on the mirror support platform for multiwavelength observations of target sources. The three X-ray telescopes allow for a nominal effective area of 4650 cm² at 1.5 keV — the biggest ever reached by far.

The satellite hosts on board two different types of CCD detectors, called European Photon Imaging Camera (EPIC), so that one telescope has at its focal plane a pn-CCD camera and the other two have MOS-CCDs cameras, named MOS1 and MOS2. The EPIC cameras perform imaging observations in the energy range 0.15 keV–15 keV, with moderate energy and angular resolution ($E/\Delta E \sim 20\text{--}50$, PSF $\sim 6''$ FWHM, $\sim 15''$ HEW)³. A comparison of the focal planes of the EPIC MOS and pn is given in Fig. 4.1.

The EPIC pn (Strüder et al., 2001) consists of a single silicon wafer, divided into four quadrants, with three 200×64 pixels CCD subunits, for a total of twelve individual CCDs (Fig. 4.1). Each pixel has a size of

³*XMM-Newton Users Handbook*, Issue 2.18, 2020 (ESA: XMM-Newton SOC).

4.2 Geometry of *XMM-Newton* focal plane for the Geant4 simulation 71

150×150 μm, with an angular resolving capability for a single photon of 3.3 arcsec.

The EPIC MOS (Metal Oxide Semi-conductor, Turner et al., 2001) is made up of seven CCDs (Figs. 4.1 and 4.3), one allocated at the focal point of the respective telescope, and the other six disposed around it, at different heights. The MOS1 and MOS2 cameras are arranged orthogonally to each other, so that the gaps between the CCDs are covered by one another. A more detailed description of the MOS camera, for the purpose of the Geant4 simulation, is given below (Sect. 4.2.1).

Each telescope hosting an EPIC MOS is also equipped with the gratings of the Reflection Grating Spectrometers (RGS), which deviate about half of the incoming light to the RGS detectors, so that each MOS receives 44% of the total flux. The RGS produces high-resolution spectra, with a resolving power $E/\Delta E$ in the range 200–800.

Finally, on board there is also the EPIC Radiation Monitor (ERM), which supplies particle environment information while the satellite is crossing the radiation belts or solar flares, for the correct operation of the EPIC cameras.

4.2 Geometry of *XMM-Newton* focal plane for the Geant4 simulation

For the Geant4 simulation we limited the elements of the focal plane assembly of *XMM-Newton* to the essential ones, while we tried to reproduce the EPIC MOS as much faithfully as possible (see Sect. 4.2.1). Fig. 4.2 illustrates the main components adopted to build the geometry

Comparison of focal plane organisation of EPIC MOS and pn cameras

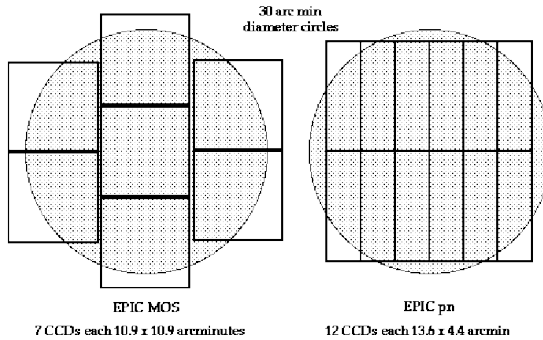


Fig. 4.1 Sketch of the field of view of the MOS (left) and pn (right) types of EPIC camera; the shaded circle represents a 30 arcmin diameter area (Credits: *XMM-Newton Users Handbook*, Issue 2.18, 2020, ESA: XMM-Newton SOC).

inside Geant4. The MOS-CCD detector at the focal plane is surrounded by a truncated cone in titanium, 100 mm height, which acts as a proton shield (hereafter called forward proton shield), absorbing all the protons with high-angles trajectories. Right above it, the filter wheel (see Sect. 4.2.2) and the entrance door to the focal plane instrumentation are placed. A further aluminium proton shield extends from the door towards the optics for a total length of 594 mm.

To simplify the simulation, we did not insert the filter wheel and the door, which do not play any significant role. Instead, we simply added a further 10 mm-thick Al truncated cone connecting the two proton shields. It absorbs all the protons scattered out of the direction towards the focal plane and guarantees a closed environment for the simulation.

4.2 Geometry of *XMM-Newton* focal plane for the Geant4 simulation **73**

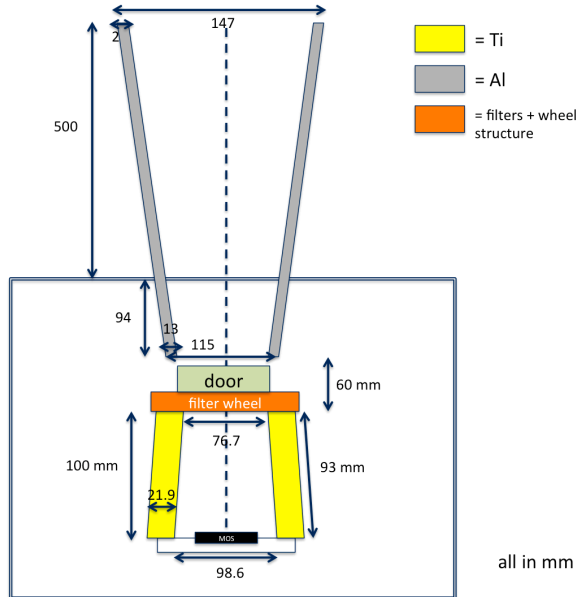


Fig. 4.2 Sketch of the elements of the focal plane assembly simulated with Geant4. Protons enter the set-up from above and encounter the Al proton shield (in grey), then the filter, the Ti forward proton shield (in yellow), and finally reach the EPIC MOS at the focal plane. The figure also shows the entrance to the focal plane instruments (the door, in light green) and the filter wheel (in orange), that we did not simulate. We simply added a further Al truncated cone connecting the two proton shields, to simulate a closed environment and to avoid the dispersion of protons. The box surrounding the focal plane assembly is indicative to the reader and was not simulated.

4.2.1 The EPIC MOS cameras

The EPIC MOS is composed of 7 front illuminated CCDs, numbered as in Fig. 4.3 for both MOS1 and MOS2, working in the energy range 0.2 keV–10 keV. The central CCD is at the focal point on the optical axis of the telescope, while the other six are at a distance of 4.5 mm towards the mirror, to approximately reproduce the focal plane curvature. Adjacent CCDs overlaps by about 1 mm to cover the 300 μm -wide dead region they have on three sides.

Each CCD has 600 x 600, 40 μm^2 pixels; one pixel covers 1.1×1.1 arcsec on the FOV, so that 15 pixels cover the mirror PSF half energy width of 15 arcsec. With an imaging area of $\sim 2.5 \times 2.5$ cm each, the mosaic of the seven CCDs covers the entire focal plane (62 mm in diameter, equivalent to 28.4 arcmin).

Each pixel has a depletion region of approximately 37 μm , while the electrodes are made of a double layer of silicon and silicon dioxide (SiO_2). To increase the efficiency, the pixels have been etched in the central part to gate oxide, so that 40% of the total pixel area is thinner than the surroundings (Hiraga et al., 2001), allowing for a higher transmission for very soft X-rays that would otherwise be absorbed in the electrodes. The etched area ('open' electrode, hereafter) consists of a 0.1 μm -thick layer of Si and 0.15 μm -thick layer of SiO_2 , while the remaining 60% ('closed' electrode, hereafter) is made up of a 0.3 μm -thick layer of Si and 0.75 μm -thick layer of SiO_2 (Fraser et al., 2014, Appendix A2).

In our simulations, we simply divided the electrode covering the depletion region into two parts for the 'open' (40% of the total area)

and ‘closed’ electrode (60% of the total area), respectively, as sketched in Fig. 4.4.

4.2.2 The Filters

The filter wheel (Fig. 4.5), allocated at a distance of 10 cm from the focal plane of the EPIC cameras, is equipped with four different filters:

- 2 thin filters, with 0.16 μm of poly-imide and 0.04 μm of aluminium
- 1 medium filter, with 0.16 μm of poly-imide and 0.08 μm of aluminium
- 1 thick filter, with 0.33 μm of polypropylene, 0.11 μm of aluminium, and 0.045 μm of tin

Additionally, the filter wheel also has an open and a closed position, the latter with 1.05 mm aluminium filter. Each filter, including the two closed/open positions, is circular shaped, with a diameter of 76 mm.

For purpose of comparison with Mineo et al. (2017), we implemented in our Geant4 simulation the medium filter, constructed as a thin disc, with the layers and the dimensions stated above.

4.3 Simulation set-up and preliminary results

We used Geant4 v. 10.02, with the Space Physics List developed for *AthenaX*-IFU and endorsed by ESA. We activated the Single Scattering process, which simulates and stores at each step of the interaction the information concerning the particle, such as energy, momentum, and

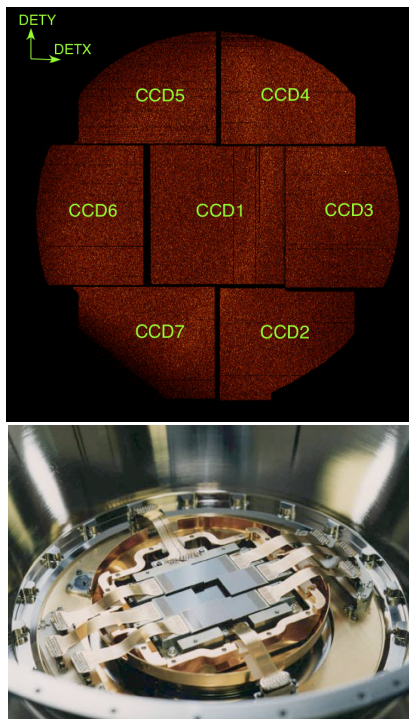


Fig. 4.3 *Left panel*: The layout of the MOS1 camera, in detector coordinates [DETX,DETY]. The image is extracted from an exposure taken during calibration with the closed filter on (Credits: *XMM-Newton Users Handbook*, Issue 2.18, 2020, ESA: XMM-Newton SOC). *Right panel*: the CCDs of the MOS cameras as mounted inside the cryostat (Turner et al., 2001).

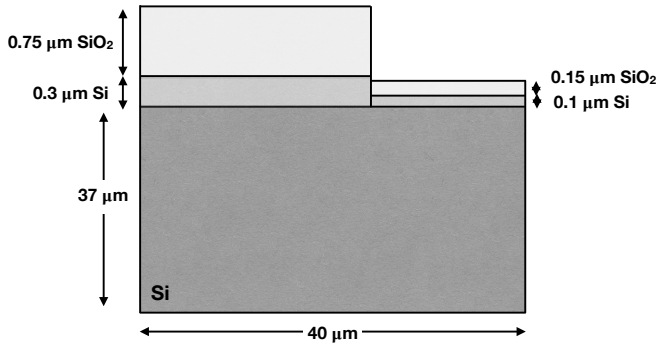


Fig. 4.4 Geometric scheme of the simulated MOS: on top of the depletion region ($37\ \mu\text{m}$ thick), the ‘closed’ and ‘open’ electrodes occupy respectively the 60% and 40% of the total area. Picture not in scale.

impact point. Due to the nanometer scale of the dimensions of the medium filters, we had to reduce the length between two consecutive interactions (called ‘step’ in Geant4 jargon) in the filter to the 20% of the thickness of each layer, to assure the correct execution of the simulation.

We used an initial distribution of 10^7 protons, with a circular beam profile of the same diameter of the filter ($76\ \text{mm}$), centered at the focal ax, $1\ \text{m}$ far from the central MOS-CCD. The energies of the protons were randomly selected between $8\ \text{keV}$ and $200\ \text{keV}$, with a flat energy distribution.

As a first, simple approach, we simulated a proton beam perpendicular to the filter. It is clear that a final and more complete simulation must take into account all the angles and directions of the protons exiting the optics. Protons lose $\sim 25\ \text{keV}$ while crossing the medium filter. Clearly, protons with less than $25\ \text{keV}$ are completely blocked

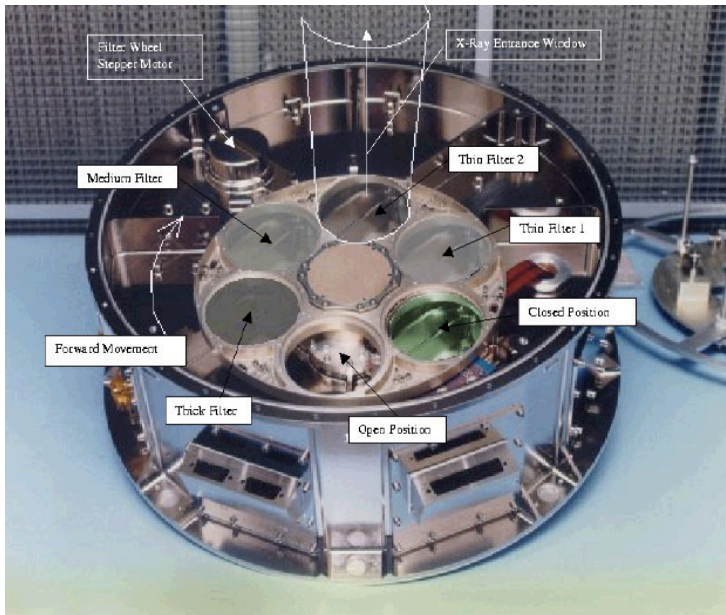


Fig. 4.5 The filter wheel for the MOS cameras in its bulk structure. The six apertures host the four filters and the closed on open positions. Picture from Turner et al. (2001).

by the filter. Of the remaining protons, almost 40% reaches the EPIC MOS, less than 10% is absorbed by the forward proton shield, and only a few (less than 10 particles) hit both the forward proton shield and the detector. Due to the shape chosen for the beam, the Al proton shield does not play any significant role, though it is obviously relevant for a more realistic beam with a greater divergence.

For each initial energy, we computed the transmission efficiency as the number of protons detected in the 0.2 keV–10 keV MOS working range over the total number of protons. The overall efficiency curve, given in Fig. 4.6 as a function of the initial energy, shows two main peaks, due to the different types of electrodes.

The broader peak centred at ~ 160 keV is due to the ‘closed’ electrode, which is thick enough to completely block the less energetic particles and let only the more energetic ones pass. Those protons lose the majority of their energy onto the electrode itself and deposit the remaining energy, usually less than 10 keV, into the depletion region of the pixel. Hence, they generate ‘good’ events (in the energy range 0.2 keV–10 keV), indistinguishable from photon events.

On the other hand, the ‘open’ electrode is thinner, so that the more energetic protons go through it and release all their energy in the depletion region. These events are rejected, since the deposited energies are outside the working range of the MOS. Instead, less energetic protons crossing the ‘open’ electrode, release a small amount of energy in the depletion region, resulting in good events. The ‘open’ electrode is responsible for the narrower peak at ~ 60 keV.

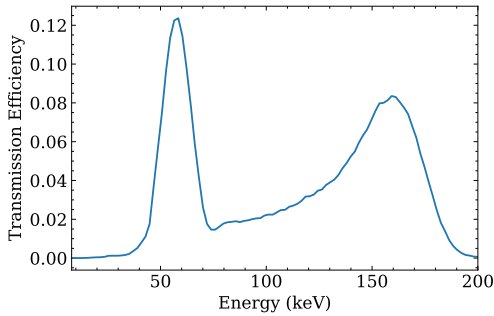


Fig. 4.6 Transmission efficiency of SPs as a function of the initial energy. The transmission efficiency is computed as the number of protons detected in the MOS working range over the total number of protons impacting on the (medium) filter.

4.4 Remarks and future perspectives

We perform a Geant4 simulation of low energy protons, with energies between 8 keV to 200 keV, hitting the EPIC MOS, after crossing the medium filter. This simulation is the first one with such a level of accuracy in the rendering of the geometry of the MOS detector. We insert also the Al proton shield between the optics and the filter and the Ti forward proton shield between the filter and the MOS-CCDs. The overall transmission efficiency shows two main peaks, due to the ‘open’ and ‘closed’ electrodes.

A consistent improvement to the present simulation might be to use a more complex energetic and spatial distribution of protons, given, for example, by the output of the ray-tracing code mentioned at the beginning of this chapter, where the non-elastic semi-empirical analytical model has been implemented. After that, the simulated resulting

spectra can be compared with observational data taken during proton flares to build a suitable proton response matrix for the EPIC MOS.

Chapter 5

Observational Astronomy

Soft protons will be relevant for *Athena* to meaningfully observe faint sources at cosmological distances. Nowadays, the knowledge of these sources is limited by existing instrumentation. The currently operational X-ray satellites can detect sources down to about 10^{-16} erg cm $^{-2}$ s $^{-1}$. Their capability to carry out high resolution spectroscopy with a resolving power ($E/\Delta E$) of 800–200 (*Chandra* and *XMM-Newton* gratings¹) is limited to much brighter sources, typically $>1 \times 10^{-12}$ erg cm $^{-2}$ s $^{-1}$. *Athena*, with its combination of a large effective area (1.4 m 2) and the X-IFU instrument (2.5 eV resolution), will allow an improvement of two orders of magnitude in the X-ray high-resolution spectroscopic capabilities. Likewise, the *Athena*/WFI, thanks to the combination of sensitivity (down to 10^{-17} erg cm $^{-2}$ s $^{-1}$)

¹*Chandra*/HETG has a resolving power ranging from ~ 800 at 1.5 keV to ~ 200 at 6 keV (<https://cxc.cfa.harvard.edu/cal/>). *XMM-Newton*/RGS resolving power goes from 200 to 800, over the energy range 0.35–2.5 keV (*XMM-Newton* Users Handbook).

and grasp, will increase the survey capability in X-rays by a similar quantum step.

A concrete idea of the future possibilities of *Athena* can be grasped only looking at the capabilities and limitations of present X-ray astronomy. To this aim, I analysed X-ray observational data of two different types of X-ray binaries, to understand how high levels of non-X-ray background can limit X-ray data analysis. Moreover, these sources are interesting *per se*, constituting valid samples to study the different mechanisms of X-ray emission due to the accretion of matter onto compact objects.

The first source is a binary millisecond pulsar and also a sample of a very faint source, for which a high level of background may compromise the detection itself. The second source is the high-mass X-ray binary Vela X-1, which is bright enough not to be affected by background issues: it constitutes the ideal case to investigate the potentiality of the high-resolution spectroscopy in view of *Athena*/X-IFU.

In the Sections below, I will illustrate the main characteristics and mechanisms of emission of X-rays of the two categories these sources belong to, pointing out some open questions and how they can be addressed with *Athena*. The complete works are presented in Chapter 6 (Amato et al., 2019) and Chapter 7 (Amato et al., accepted).

5.1 Introduction on accreting X-ray binary systems

X-ray binary systems consist of a main sequence star, called companion star or donor star, and a compact star, normally a neutron star (NS) or a black hole (BH), orbiting around the common center of mass (see, e.g., Longair, 2011). In the frame of reference rotating with the binary system, the total potential energy is given by the sum of the gravitational potential energy of the masses of the two bodies and the centrifugal potential associated with their binary motion. At a generic radial distance r from the center of mass of the binary system, the equipotential surfaces are defined as:

$$\phi = \frac{GM_1}{r_1} + \frac{GM_2}{r_2} - \Omega^2 r^2 = \text{constant} \quad (5.1)$$

where M_1 and M_2 are the masses of the orbiting bodies and r_1 and r_2 are their distances to the point at r (Longair, 2011). For a critical value of r , the corresponding equipotential surface encompass both the compact object and the companion star. The two area surrounding the compact object and the donor star are called ‘Roche lobes’. They intersect at the inner Lagrangian point L_1 , as in Fig. 5.1.

According to the mass of the companion star, X-ray binary systems are usually divided into three main categories:

- Low-mass X-ray binaries (LMXBs), when the companion star has a mass $M \sim M_\odot$;

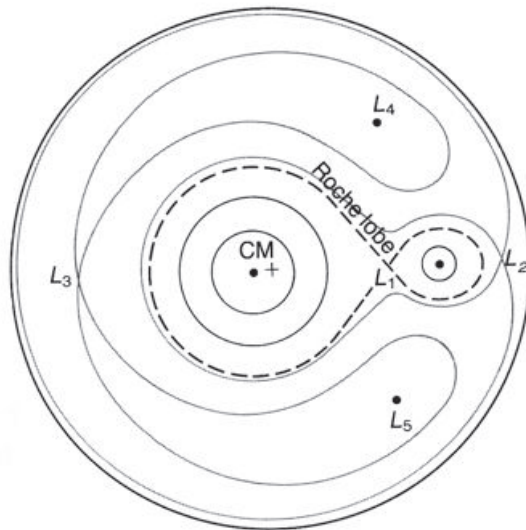


Fig. 5.1 Sketch of the equipotential surfaces of a binary star system in the rotating frame of reference, for a mass ratio of the stars of 10:1. The equipotential surface connecting the two bodies of the system defines the Roche lobes (dashed line), which intersect at the inner Lagrangian point L_1 . The other Lagrangian points are indicated as L_2 , L_3 , etc. (Longair, 2011).

- High-mass X-ray binaries (HMXBs), when the companion star has a mass $M \geq 10M_{\odot}$;
- Intermediate-mass X-ray binaries (IMXBs), when the companion star has a mass $1M_{\odot} < M < 10M_{\odot}$.

These categories also differ in the mechanisms of accretion of matter onto the compact object. In the case of LMXBs, the companion star fulfils its Roche Lobe and the material from the more superficial layers overflows via the inner Lagrangian point L_1 onto the compact object. The in-falling material carries angular momentum, so that an accretion disc forms around the compact object (Fig. 5.2, left panel).

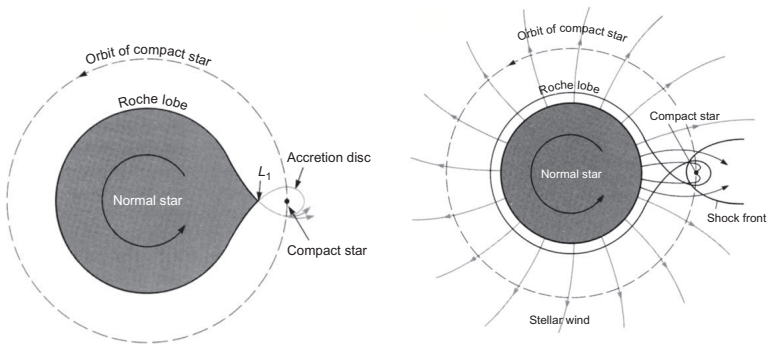


Fig. 5.2 Two different ways of accretion onto compact objects in X-ray binary systems (Longair, 2011). *Left panel*: a low-mass X-ray binary, where the stream of matter falls onto the compact object via the inner Lagrangian point L_1 and forms an accretion disc. *Right panel*: a high-mass X-ray binary, where the matter radiated by the stellar wind of the companion directly accretes onto the compact object.

In HMXBs, normally, the compact object is completely embedded in the strong stellar wind of the companion, usually a class O/B star,

with mass loss rate of the order of $10^{-5}M_{\odot} \text{ y}^{-1}$ (see the most recent review by Kretschmar et al., 2019). Accretion onto the compact object takes place through the gravitational capture of a certain fraction of the wind of the giant star (Fig. 5.2, right panel). HMXBs are divided, in turn, into subsequent categories:

- Be/X-ray binaries (BeHMXBs): a NS around a Be star in a highly elliptical orbit; the stellar wind is emitted in a disc around the Be star, so that matter is periodically accreted onto the NS, i.e., when it passes through the disc.
- Supergiant X-ray binaries (SgHMXBs): the compact object (NS or BH) is orbiting a O/B class supergiant companion in a circular or slightly eccentric orbit (as in Vela X-1, cfr. Chapter 7). Amongst them, Supergiant Fast X-ray Transients (SFXTs) show short outbursts with very fast rise times (\sim tens of minutes) and typical durations of a few hours.
- (Beginning Atmospheric) Roche Lobe Overflow (RLO) systems: the massive star is filling its Roche lobe and the matter flows through the inner Lagrangian point so that an accretion disc is formed. These systems have short orbital and spin period. Only a few are known, e.g., Cen X-3, SMC X-1, LMC X-4.

IMXBs fall on the borderline between the two categories and are thought to be at the origin of LMXBs. They can also present an accretion disc, as in the case of Her X-1.

The zoo of X-ray binaries is so vast that the one listed above is not the only possible classification. Astronomers also refer to X-ray

binaries as as ‘X-ray bursters’ (Strohmayer et al., 1996; Watts, 2012, for a review), when they exhibit periodic and rapid increases in X-ray luminosity, ‘X-ray pulsars’ (Davidson and Ostriker, 1973; Giacconi et al., 1971; Lamb et al., 1973; Pringle and Rees, 1972), when they display strict periodic variations in X-ray intensity, and ‘microquasars’ (see review by Corbel, 2011; Mirabel et al., 1992), when they also show strong and variable radio emission.

5.1.1 Millisecond pulsars

A highly magnetized rotating NS emits beams of electromagnetic radiation from its magnetic poles. This radiation is detected only when pointing directly to the observer. If the magnetic axis is not aligned with the line of sight, due to the rotation of the NS, the observer registers only pulsed radiation – the so-called ‘lighthouse effect’.

Millisecond pulsars (MSPs) are binary systems with a pulsars with rotational periods $P \lesssim 40$ ms. Pulsed emission from MSPs has been detected in radio, X-, and γ -ray wavebands. The short spin period of MSPs is easily explained by their nature of accreting binary systems. Mass flowing from the companion star onto the NS transports angular momentum, that is transferred to the pulsar, inducing a spin-up effect. This theory, know as the ‘recycling scenario’, simply states that MSPs are old, rapidly rotating NS spun-up by the matter accreted from the donor star in a close binary system (Bhattacharya and van den Heuvel, 1991a; Tauris and van den Heuvel, 2006). This is why they are also called ‘recycled pulsars’.

MSPs are mainly found in globular clusters, where the population is old and the high-density environment enhances alternative mechanisms

in the formation of binary systems, such as tidal capture, collision with a giant star, or exchange between primordial binaries.

Amongst the MSPs, we can distinguish two subclasses, named after two species of Australian spiders: ‘black widows’ and ‘redbacks’ (see Roberts, 2011, 2013). They both have tight orbits ($P_{\text{orb}} < 24$ h) and low-mass companions, with $M \ll 0.1M_{\odot}$ for black widows and $M \sim 0.1 - 0.4M_{\odot}$ for redbacks. In these close binaries the spin axis is aligned or close enough to the orbital plane, so that the companion star is directly irradiated by the beamed emission from the poles of the pulsar. The external layers of the donor star are then heated up to evaporation, so that the star progressively loses its mass and gets colder. In most cases, the star is out of the hydrodynamic equilibrium and it is bloated, as proved by the observed optical modulation. The star fills its Roche lobe, causing material to flow onto the NS. This explains why redback and black widow pulsars have short spin periods (due to the spin-up caused by accretion), and why the companion is non-degenerate and very faint. The study of black widows and redbacks falls inside the pulsar recycling scenario. Especially redbacks are thought to be recycled pulsars spun-up to their maximum before the accretion stopped. Both the species are also important for studying the regions close to the pulsar, in the proximity of the light cylinder.

The debate on the origin of X-ray emission from these systems is still on-going. Three main mechanisms have been proposed so far: non-thermal pulsed X-ray emission, thermal X-ray emission from the polar

caps, and intra-binary shock scenario (see, for instance, Bogdanov, 2018, and references therein).

Non-thermal pulsed X-ray emission is more likely produced by relativistic particles accelerated in the pulsar magnetosphere. It is the case of the youngest, more energetic pulsars, with the highest magnetic field at the light cylinder. They show narrow pulses and power-law spectra.

Thermal X-ray emission is produced when a flow of relativistic particles returns from the open field line region into the magnetic polar caps, heating them up. Those MSPs show broad X-ray pulsations, soft blackbody-like spectra, and luminosities $\lesssim 10^{31}$ erg s⁻¹.

According to the intra-binary shock scenario, X-ray emission can be produced by the interaction of the pulsar wind with the material flowing from the companion star. It is typical for black widow and redback binary systems, where it would be responsible for the eclipse of the NS in eclipsing systems and for the modulation of the X-ray radiation with the orbital phase.

In Chapter 6, I will present a multi-wavelength search for counterparts and an X-ray data analysis of the radio MSP J1836-2354A, in the Galactic globular cluster M22. The source was at the edge of detectability of *Chandra* (with an X-ray luminosity of $L_X \sim 10^{30}$ erg s⁻¹), which makes hard to establish its nature of redback or black widow and infer the emission mechanism of X-rays.

5.1.2 Supergiant X-ray binaries

SgHMXBs are wind-fed HMXBs (van den Heuvel and Heise, 1972; Walter et al., 2015, for a review), with a O/B supergiant companion star.

They have typically small orbital periods ($P_{\text{orb}} \sim 3 - 15$ d) and long spin period ($P_{\text{spin}} \sim 10^2 - 10^4$ s). Except for a few sources, they occupy the upper-left corner of the $P_{\text{spin}} - P_{\text{orb}}$ Corbet diagram (Fig. 5.3).

Their orbits being almost circular, the compact object is constantly embedded in the wind of the supergiant star, so that the accretion onto the compact object can be considered approximately spherical. The X-ray emission is luminous ($L_X = 10^{36} - 10^{38}$ erg s $^{-1}$), persistent and highly variable over short timescales. The high spin periods of the NSs in SgHMXBs suggest strong magnetic fields ($B \sim 10^{11} - 10^{12}$ G). Stellar wind and Roche lobe overflow accretion can also coexist, as in the case of Cyg X-1.

In the case of a SgHMXB hosting a NS, the interaction of the stellar wind with the gravitational field of the compact object creates peculiar large-scale structures. The material accreting from the front is compressed by the gravitational field of the compact object and is heated by the X-ray radiation of the NS, so that an accretion wake is formed. On the other hand, the stellar wind photoionised by the passage of the NS creates a photoionisation wake that trails the compact object along the whole orbit. This complex geometry results in strong changes in the absorption while the line of sight crosses the different elements at different orbital phases.

To further complicate the picture, the perturbed stellar wind shows evidence of clumpiness: denser blobs of matter embedded in the smooth wind of the companion star. Clumps are responsible for short changes (of the order of ks) in flux and column density, generated, for instance, when a clump is directly accreted onto the NS along the line of sight (see, e.g., Martínez-Núñez et al., 2014). Clumps are also responsible for

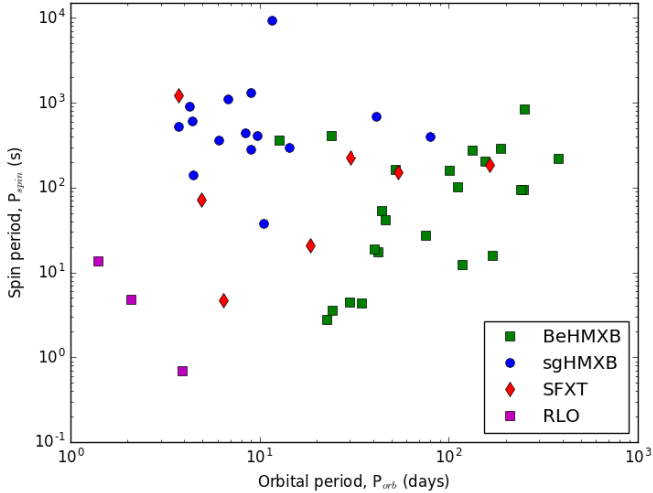


Fig. 5.3 Corbet diagram P_{spin} vs. P_{orb} of the population of HMXBs. Different classes are indicated with different symbols: green squares for BeHMXBs, blue dots for SgHMXBs, red diamonds for SFXTs, and violet squares for RLO (Credits: Chaty et al., 2019).

the presence of multi-phase plasma, where collisional and photoionised components seem to coexist (Goldstein et al., 2004; Grinberg et al., 2017; Hirsch et al., 2019; Schulz et al., 2002; Watanabe et al., 2006).

In Chapter 7, I show a high-resolution spectroscopy study of the SgHMXB Vela X-1 while the line of sight is crossing the photoionisation wake. The aim is to investigate the nature of the plasma at this orbital phase with both canonical plasma diagnostic techniques and more advanced plasma models. Plasma diagnostic studies on highly resolved X-ray spectra are crucial to understand the accretion of these systems. Currently, they can only be made with the grating spectrometers on

board of *Chandra* and *XMM-Newton*, albeit the know limitations on energy resolution. The future X-ray observatories, *XRISM* and especially *Athena*, will overcome these limitations, reaching energy resolutions of the order of the eV, as shown by simulations in Section 7.6. Moreover, if the requirement on the background for *Athena* is satisfied, the same studies could be conducted in the future also for fainter HMXBs.

Chapter 6

Search for multiwavelength emission from the binary millisecond pulsar PSR J1836-2354A in the globular cluster M22

6.1 Introduction

Millisecond pulsars (MSPs) are neutron stars (NSs) emitting radio pulsed radiation at their spin periods. They can be isolated or in binary systems. According to the recycling scenario (Alpar et al., 1982), MSPs are the outcome of accretion onto the NS of mass transferred from a

late-type companion. After Gyr-long mass accretion phase during which these systems appear as low-mass X-ray binaries (LMXBs), the mass transfer rate declines allowing the activation of a radio and/or γ -ray pulsar powered by rotation of its magnetic field (Bhattacharya and van den Heuvel, 1991b; Burderi et al., 2001). A few systems – three so far – were found to transit from an accretion to a rotation-powered state and viceversa proving the existence of the link between LMXBs and MSPs (Bassa et al., 2014; Papitto et al., 2013; Stappers et al., 2014).

Globular clusters (GCs) are the densest environments in our Galaxy where MSPs can be found. Their high stellar densities imply a high rate of dynamical interactions, such that binary systems are formed through alternative mechanisms to the normal evolutionary channels, e.g., tidal capture (Fabian et al., 1975), collisions with a giant star (Sutantyo, 1975) or by exchange between primordial binaries (Hills, 1976). Moreover, due to the aged population, binary systems in GCs are predominantly constituted of a compact object, like white dwarfs (WDs) or NSs, which accretes matter from its companion, usually a low-mass Main Sequence star. Hence, the X-ray population in GCs is mainly constituted by a mixture of quiescent LMXBs, Cataclysmic Variables (CVs), MSPs and Chromospheric Active Binaries (ABs) (see Heinke, 2010, for a review).

M22 (NGC 6656) is one of the most luminous GC in the Milky Way. At a distance of 3.2 kpc, it has a projected core radius (r_{core}) of $1.33'$ and a half-mass radius of $3.36'$ (Harris, 1996, 2010 edition), a tidal radius of $31.9'$ (Alonso-García et al., 2012), a total mass of $\sim 5 \times 10^5 M_{\odot}$ (Cheng et al., 2018) and an absolute age of 12.67 Gyr (Forbes and Bridges, 2010). Lynch et al. (2011) reported the detection

of two radio MSPs in this GC: J1836-2354A and J1836-2354B. J1836-2354A (M22A, hereafter) is a 3.35 ms pulsar in a binary system with an orbital period of 4.87 h, negligible eccentricity, $a \sin(i) = 0.046412$ lt-s, a mass function of $2.609(1) \times 10^{-6}$ and a minimum mass of $0.017 M_{\odot}$ for the companion star. An extremely low mass secondary would indicate M22A as a black widow system, rather than a redback system, which instead harbours a non-degenerate secondary (i.e. $M_2 \geq 0.1 M_{\odot}$) (Roberts et al., 2018). The other pulsar (M22B hereafter) is isolated with a 3.23 ms spin period. Both pulsars lie within the cluster core radius.

Besides the radio emission, MSPs can also be detected in other bands, thus allowing to probe different environments and processes in, or close to, the pulsar magnetosphere, e.g. optical emission can come from the companion star or, in the case of a LMXBs, from the accretion disk (Archibald et al., 2009), when present.

Furthermore, γ -ray emission from Galactic GCs has been detected by the LAT instrument on board of *Fermi Gamma Ray Space Telescope* (*Fermi-LAT*, hereafter) since its launch, in 2008. Being MSPs strong emitters of γ -rays (Chen, 1991; Harding et al., 2005) and being GCs extremely rich of MSPs, the whole γ -ray emission from GCs is thought to be the convolution of the emission from all the MSPs in a cluster (Abdo et al., 2010; Caraveo, 2014). γ -ray emission from M22 was only recently detected by *Fermi-LAT* (Zhou et al., 2015), after more than 6 years of observations. A flux of $(8.6 \pm 1.9) \times 10^{-12}$ erg cm $^{-2}$ s $^{-1}$ was derived by fitting the spectrum with a power law model with a spectral index of 2.7 ± 0.1 , in the energy range 0.1-100 GeV.

The first X-ray observations of M22 were made with *Einstein* (Hertz and Grindlay, 1983) and *ROSAT* (Johnston et al., 1994). More recently, *XMM-Newton* observed the cluster in 2000 (Webb et al., 2002, 2004) while *Chandra* in 2005 (Webb and Servillat, 2013) and in 2014. Webb and Servillat (2013) analysed the *Chandra* observation made in 2005 and reported a faint X-ray source (Source 3 in their Table 1) as the possible X-ray counterpart of M22A. In the work here illustrated, we used all the available archival data from *Chandra* and *XMM-Newton*, focusing especially on the longest *Chandra* observation (2014). We also analysed 28 observations performed with the *X-ray Telescope* (XRT, Burrows et al., 2005) on board of the *Neil Gehrels Swift Observatory* (Gehrels et al., 2004, *Swift* hereafter), which has been monitoring the cluster for the past two years. We also performed a search for the optical counterpart using the *Hubble Space Telescope* (*HST*) catalogue from the HUGS project (Piotto et al., 2015), as well as we inspected the 4-year *Fermi*-LAT catalogue (3FGL; Acero et al. (2015) and the 8-yr catalogue (4FGL, The Fermi-LAT collaboration, 2019).

6.2 X-ray observations and data reduction

We analysed two *Chandra* observations of M22, made on 2005 May 24 for 15.82 ks with ACIS-S in the FAINT mode (Observation ID 5437) and on 2014 May 22 for 84.86 ks with ACIS-S in the VFaint mode (ObsID 14609). For data extraction and analysis we used CIAO version 4.10 and CALDB version 4.7.7. Data sets were reprocessed without including pixel randomization (the parameter `pix_adj` was set to EDser), in order to slightly improve the point-spread function (PSF).

The *XMM-Newton* observation of M22 was performed on 2000 September 19 (ObsID 0112220201), for a total exposure of 41.2 ks, using the EPIC instruments (pn, MOS1 and MOS2) in imaging mode with the medium filters. We reprocessed the data to obtain calibrated and concatenated event lists with the Science Analysis Software (SAS) version 16.0.0. We produced images for all the EPIC instruments in three different energy ranges: 0.5-2 keV, 2-4 keV, and 4-10 keV.

We analysed all the *Swift*/XRT observations of the source performed between March 2017 and August 2018. The full XRT observation log consists of 28 pointings of 1–3 ks exposure each, with approximately one or two visits per month. All the data were taken in Photon Counting (PC) mode. Data were reprocessed with `xrtpipeline` to obtain the cleaned event files and exposure maps, using R.A. and Dec. of the source, as detected in the *Chandra* ObsID 14609 (R.A. = 18:36:25.375, Dec. = -23:54:51.08, in the J2000 system). We merged all the observations, combined the event lists and exposure maps, using the XIMAGE, version 4.5.1 package. Finally, we extracted the image from the merged event list file. The log of all the analysed X-ray observations is reported in Table 6.1.

6.3 Source detection and astrometric corrections of the *Chandra* observation

The radio position of M22A determined by Lynch et al. (2011) is 2.2' and 0.9' offset from the *Chandra* pointing directions of the 2004 and 2014 observations, respectively. This ensures negligible distortion of the PSF and hence a high accuracy in determining the position of the

Table 6.1 Log of the X-ray observations of M22 analysed in this work.

	Obs.	Start Time (UT)	Stop Time (UT)	Exposure Time (s)
<i>XMM-Newton</i>	0112220201	2000-09-19 22:05:00	2000-09-20 09:31:56	41216
<i>Chandra</i>	5437	2005-05-24 21:22:27	2005-05-25 02:12:40	15819
	14609	2014-05-22 19:40:24	2014-05-23 20:00:44	84864
<i>Swift/XRT</i>	34847001	2017-03-07 06:34:57	2017-03-07 09:03:36	2412
	34847002	2017-03-23 15:07:57	2017-03-23 19:09:39	2550
	34847003	2017-04-03 23:58:57	2017-04-04 05:22:41	1988
	34847004	2017-05-02 03:55:57	2017-05-02 23:37:16	2272
	34847005	2017-05-16 21:24:57	2017-05-17 00:07:26	1377
	34847006	2017-05-30 06:05:57	2017-05-30 10:24:12	2926
	34847007	2017-06-13 19:06:57	2017-06-13 21:36:51	3011
	34847008	2017-06-27 05:14:57	2017-06-28 00:30:46	2801
	34847009	2017-07-11 10:18:57	2017-07-11 16:41:07	2821
	34847010	2017-07-25 01:22:57	2017-07-26 00:34:23	2693
	34847011	2017-08-08 03:15:57	2017-08-08 16:59:13	3074
	34847012	2017-08-22 11:54:57	2017-08-22 20:47:36	1529
	34847013	2017-08-25 11:29:57	2017-08-25 13:13:34	925
	34847014	2017-09-05 13:53:57	2017-09-05 17:57:26	1086
	34847015	2017-09-08 13:16:57	2017-09-08 15:50:11	2580
	34847016	2017-09-19 20:48:57	2017-09-20 00:23:58	2580
	34847017	2017-10-03 03:26:56	2017-10-03 13:40:01	2878
	34847018	2017-10-18 00:14:57	2017-10-18 23:29:29	2989
	34847019	2017-10-31 04:04:57	2017-10-31 06:33:44	2221
	10376001	2018-02-16 02:20:57	2018-02-17 22:34:10	8397
	10376002	2018-03-15 10:04:56	2018-03-16 00:43:10	3881
	10376003	2018-03-16 20:32:57	2018-03-17 02:13:05	5305
	10376004	2018-04-15 02:02:57	2018-04-15 10:52:39	5433
	10376005	2018-04-18 09:53:57	2018-04-18 13:45:06	1958
	10376006	2018-05-15 07:10:57	2018-05-15 11:24:38	1645
	10376007	2018-05-16 07:03:57	2018-05-17 00:06:40	7456
	10376008	2018-06-15 10:51:57	2018-06-15 19:39:23	9792
	10376009	2018-07-15 01:53:56	2018-07-15 17:07:35	9816

source. For each observation, we created an exposure-corrected image and exposure map using the `fluximage` tool with a binning equal to 1; we used the tool `mkpsfmap` to determine the PSF-size at each pixel. We selected two different energy bands, 0.3–10 keV and 0.5–6 keV, and for these bands we set the encircled counts fraction (ECF) equal to 0.5, while the energy of the PSF was equal to 1.4 keV and 0.3 keV for the broader and for the softer energy band, respectively. We used the source detection tool `wavdetect` with pixel wavelength radii of 1.0, 1.4, 2.0, 2.8, 4.0, 5.6. The probability threshold was left to the default value of 10^6 (corresponding to one spurious source in a 1000×1000 pixel map). Image and detection regions (corresponding to a 3σ error on the position) are shown in Fig. 6.1. We limited our analysis to the ACIS-S3 chip.

An X-ray source is found at R.A. = 18:36:25.5(8) and Dec. = -23:54:51.5(5), with 1σ errors, in the 2014 observation. The position detected in the 2005 observation differs of $0.1''$ in R.A. with respect to the 2014 one. These are consistent with that reported by Webb and Servillat (2013), although with a slightly larger uncertainty, likely due to the different source extraction procedure (ACIS-Extract). The detection is always consistent with a point-like source, with no evidence of extended emission. The X-ray source is found to be at $0.2''$ East and $0.9''$ North from the radio position of M22A. Since the long 84 ks *Chandra* exposure could be affected by the spacecraft drift, we improved the absolute astrometry, using a cross-matching method.

For this purpose, we used the UV-optical catalogue of M22 from the *HST* UV Globular Cluster Survey (HUGS; Nardiello et al., 2018; Piotto

et al., 2015, see Section 6.5), available at the University of Padua¹. The catalogue covers an area of about $4' \times 4'$, centred on the cluster core. The surveys also encompass two distant regions (parallel fields, Simioni et al., 2018), but none of the X-ray sources detected in the ACIS-S3 chip fall in those two regions. We therefore limited our analysis to the cluster HUGS source catalogue. Among the optical sources, we could select only nine that satisfy the condition of being the bright ones (typically $F814W < 18$ mag) within a small ($\lesssim 1.2''$ major axis) 1σ error ellipse. In most cases, the optical source was the only one (when more than one bright source was present the corresponding X-ray source was disregarded). In just a few cases, two or three much fainter stars were present. The association was done irrespective of being cluster members or not (see also Section 6.5). Among the nine sources, eight are within the cluster core and one within the half-mass radius. One of them corresponds to the source labelled CV1 by Webb and Servillat (2013), classified as a cataclysmic variable through the study of its X-ray emission and optical spectrum. Its position matches the star R0047833 in the HUGS catalogue. We use the CIAO tools `wcs_match`, to perform a cross-matching through a translation (`method=trans`), and `wcs_update` to upgrade the aspect solution file, the `level=2` event files and the list of the detected sources. We find an average systematic shift of $+0.071''$ in R.A. and of $-0.634''$ in Dec., with an rms value of $0.3''$. Applying this correction, we then find the X-ray source at R.A.=18:36:25.5 and Dec.=-23:54:52.1. The radio MSP M22A lies well inside the 1σ X-ray error ellipse (see Fig. 6.3). Hence, the detected

¹<http://groups.dfa.unipd.it/ESPG/treasury.php>

X-ray source can be confidently seen as the counterpart of the radio MSP M22A.

6.4 X-ray Data analysis

We find 5.5 and 11.8 net counts for ObsID 5436 and ObsID 14609, respectively. The net count rates are then $(4.1 \pm 1.8) \times 10^{-4}$ cts s^{-1} (ObsID 5436) and $(1.8 \pm 0.4) \times 10^{-4}$ cts s^{-1} (ObsID 14609). We verified the consistency of the two count rates by a Poissonian ratio test. We tested the null hypothesis probability of the first rate being equal to the second. The resulting *p-value* of 0.1 does not constitute a strong evidence against the null hypothesis probability, which is not rejected. We concluded that there is not any statistically significant variability between the two observations. We also investigated the distribution of the arrival times of the detected photons with energies up to 8 keV, considering an extraction region of $1''$, for both the 2005 and 2014 *Chandra* observations. We do not detect any clear modulation linked to the orbital period ($P_b = 0.2028278011(3)$ days), possibly due to the very low statistics.

We extracted a source spectrum from each observation, selecting a circular area centered at the best-fit position returned by WAVDETECT using a radius of $1''$ and binning the spectrum to have at least 1 count per noticed bin. We used XSPEC, version 12.9, for spectral analysis. Due to the low number of counts, we used the C-statistic (Cash, 1979). Errors are given at 1σ confidence level, if not stated otherwise.

Since no statistically significant variability is present in the two observations, we fitted the two spectra together, in the energy range 0.5–6 keV, adopting two alternative models: an absorbed power law and an absorbed black-body. We used the TBABS (in XSPEC) component for the interstellar neutral absorption, setting the element abundances from Wilms et al. (2000) and the cross-sections from Verner et al. (1996), and the equivalent hydrogen column density value N_{H} fixed to 0.197×10^{22} atoms cm^{-2} (Cheng et al., 2018).

The power law model gave a photon index $\Gamma = 1.5_{-0.6}^{+0.7}$, while the black-body model (BBODYRAD in XSPEC) has a best-fit temperature of 0.8 ± 0.4 keV. To evaluate the fit goodness, we iterated over 1000 Monte Carlo simulated spectra, within XSPEC. We obtained the 0.30% of realisations with lower C-statistic values than the best-fit ones, in both cases. Hence, the models are both acceptable, though the very low number of counts does not allow us to discriminate between them.

The unabsorbed fluxes, calculated in the energy range 0.5–8 keV, are $2.3_{-0.6}^{+1.2} \times 10^{-15}$ erg cm^{-2} s^{-1} for the power law model and $1.8_{-0.9}^{+1.2} \times 10^{-15}$ for the black-body model. These values give an X-ray luminosity of 2.8×10^{30} erg s^{-1} for the power law model and 2.2×10^{30} erg s^{-1} for the black-body model, respectively, in the energy range 0.5–8 keV, assuming a distance of 3.2 kpc (see Table 6.2). We obtained an unabsorbed X-ray flux slightly lower than that reported by Webb and Servillat (2013) of 5.2×10^{-15} erg cm^{-2} s^{-1} (1σ error). This is due to the different power law slope assumed by Webb and Servillat (2013) in their analysis (2.1 instead of 1.5). However, by fitting the 2005 spectrum with a fixed the power law slope at 2.1, we obtained a slightly higher, but still consistent, unabsorbed flux, equal to

Table 6.2 Best-fit values of the simultaneous fit of the spectra of M22A from *Chandra* ObsID 5437 and 14609. The fit was performed with the C-statistic, the errors are at 1σ confidence level and the goodness was calculated over 1000 Monte Carlo simulations on the ObsID 14609.

Model	Γ	kT (keV)	R_{eff} (10^{-3} km)	Unabs. Flux [0.5-8 keV] (10^{-15} erg cm^{-2} s^{-1})	L_X [0.5-8 keV] (10^{30} erg s^{-1})
POWER-LAW	$1.5^{+0.7}_{-0.6}$			$2.3^{+1.2}_{-0.6}$	$2.8^{+1.5}_{-0.9}$
BBODYRAD		0.8 ± 0.4	$6.5^{+7.5}_{-3.8}$	$1.8^{+1.2}_{-0.9}$	$2.2^{+2.0}_{-1.1}$

9.1×10^{-15} erg cm^{-2} s^{-1} , in the energy range 0.5-8 keV.

The archival *XMM-Newton* and *Swift* observations have overall exposure times of ~ 41 ks and ~ 96 ks. Using the NASA's HEASARC tool WEBBPIMMS², we estimated the expected count rates for the *XMM-Newton*/EPICs and *Swift*/XRT observations. We converted the mean flux of the two *Chandra* observations derived from the power law model into count rates, obtaining 5.4×10^{-4} cts s^{-1} for *XMM-Newton*/EPICs and 4.4×10^{-5} cts s^{-1} for *Swift*/XRT. The count rate thresholds (3σ) for *XMM-Newton* observation and for the stacked *Swift* one are of 6.9×10^{-4} cts s^{-1} and 8.5×10^{-5} cts s^{-1} . Hence, the source flux is well below the threshold of detectability in both the data sets. Moreover the PSFs are far larger (nominally $15''$ at 1 keV for *XMM-Newton* and $18''$ at 1.5 keV for *Swift*, against $0.5''$ of *Chandra*), so that M22A, which is in the cluster core, cannot be resolved with respect to the closest and brightest source (source 2 of Webb and Servillat (2013), see also Fig. 6.1).

²<https://heasarc.gsfc.nasa.gov/cgi-bin/Tools/w3pimms/w3pimms.pl>

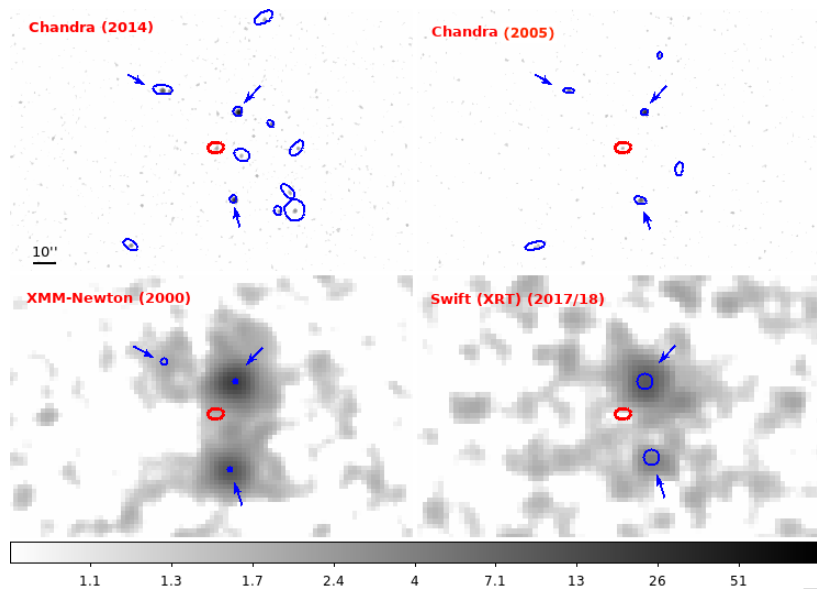


Fig. 6.1 X-ray images of *Chandra* ObsID 14609 (*top left panel*) and 5437 (*top right panel*), of *XMM-Newton* obs. (*bottom left panel*) and of the stacked *Swift*-XRT observations (*bottom right panel*). The red ellipse corresponds to the position of M22A in the longest *Chandra* obs. (14609), the blue circles/ellipses indicate the other detected X-ray sources. The dimensions of each ellipse in *Chandra* observations correspond to a 3σ positional error as given by the detection pipeline, the dimension of the circles of *Swift* observations are given by a centroid procedure and the ones of *XMM-Newton* observations are the catalogued positional errors (<http://xmm-catalog.irap.omp.eu/>). The blue arrows point to the most luminous sources close to M22A detected in almost all the data sets.

However, since it cannot be excluded that the source could have undergone a change of luminosity in the recent past, we inspected the *Swift*/XRT images one by one, with XIMAGE, using a signal to noise ratio threshold of three. Once we checked out that the source was never detected, we looked for its X-ray emission in the stacked XRT image. For purpose of comparison with Webb et al. (2004), we also performed a source detection on the *XMM-Newton* combined EPIC/pn and EPIC/MOS images, using the tool `edetect_chain`, with the appropriate Energy Conversion Factor (`ecf`) values of the medium filter configuration. In neither case we detect any source at the radio position of the MSP, as the source have remained below the threshold sensitivity of the two instruments. The detection pipelines, indeed, identified sources with fluxes down to 9×10^{-15} erg cm⁻² s⁻¹ for *XMM-Newton* and to 1.1×10^{-14} erg cm⁻² s⁻¹ for *Swift*. The sensitivity thresholds, together with the larger PSFs, justify the lack of detection of M22A.

6.5 Optical observations

We searched for the optical counterpart of the radio MSP M22A using *HST* images and the astrophotometric catalogue of M22 (Nardiello et al., 2018) from the treasury project HUGS (Piotto et al., 2015). M22 has been imaged in several filters with the WFC3/UVIS (F275W, F336W, F438W) and ACS/WFC cameras (F606W and F814W). We inspected the stacked images in all the five filters, against the astrophotometric catalogue that also provides probability membership for each detected star (see Nardiello et al., 2018, for details). Within the accuracy of the radio position provided by Lynch et al. (2011), no optical coun-

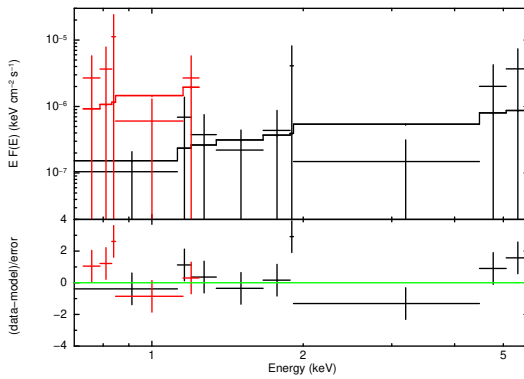


Fig. 6.2 Simultaneous fit of *Chandra* obs. ID 14609 (black) and obs. ID 5437 (red) with a power law plus absorption model and residuals as $(\text{data}-\text{model})/\text{error}$ where error is calculated as the square root of the model predicted number of counts, in the energy range 0.5-6 keV.

terpart is detected. The two closest cluster member stars, catalogued as R0039501 ($m_{814w} = 20.59(5)$) and R0002743 ($m_{814w} = 17.254(7)$) in the HUGS project list, are found at much larger distance of $0.197''$ and $0.237''$, respectively. The optical positions of these two stars are very accurate, $0.0014''$ and $0.0024''$ respectively (Nardiello, private communication), and therefore we exclude them as possible counterparts. We infer a 3σ upper limit at the position of the radio source of $m_{F606W} \geq 25.6$ mag and $m_{F814W} \geq 24.7$ mag in the stacked long exposures in these two filters. The stacked astrometrically corrected image in the F814W filter is shown in Fig. 6.3, together with the radio position of the MSP from Lynch et al. (2011) and with the X-ray position of our detection in the latest *Chandra* dataset.

While we are confident that no optical counterpart is detected for the radio source M22A in the *HST* images, we note that *Chandra* error region in Fig. 6.3 shows four or five optical sources within the 1σ region and tens of sources at the 3σ level. A scrupulous inspection of the closest optical sources in the Colour-Magnitude diagram revealed no bona-fide candidate to a possible red straggler source (Geller et al., 2017), which are sometimes associated to quiescent X-ray binary systems (Shishkovsky et al., 2018). We therefore believe that the source identified in the *Chandra* data is the X-ray counterpart of the radio MSP M22A and consequently none of the optical sources in its error ellipse can be safely associated to the X-ray source.

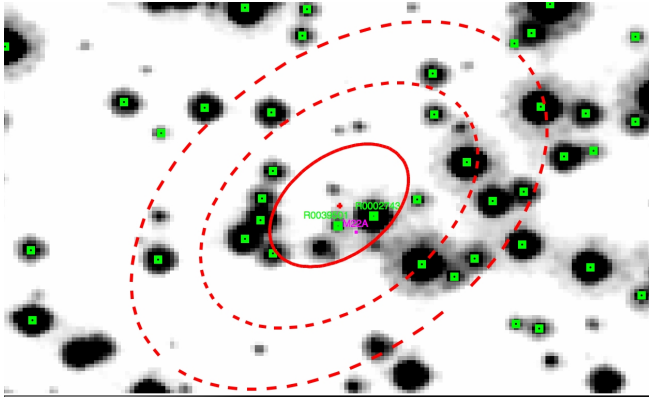


Fig. 6.3 The $8'' \times 4''$ enlarged region of the *HST* stacked ACS image in the F818W filter (Nardiello et al., 2018) around M22A. North is up, East is left. M22A is marked in magenta. The X-ray 1σ error ellipse is reported with a red line, the 2σ and 3σ error ellipses with red dashed lines. The green boxes mark the optical stars belonging to the M22 cluster with probability membership $> 80\%$. The two cluster stars, labelled R0039501 and R0002743, have accuracies that rule out any association with M22A.

6.6 The γ -ray emission from M22

Based on the γ -ray association to the GC M22 by Zhou et al. (2015), we checked whether this γ -ray source is compatible with the M22A position by using the latest *Fermi*-LAT catalogues. We found in the 4-year catalogue (3FGL, Acero et al., 2015) that the source 3FGL J1837.3–2403 is positionally consistent with the emission detected by Zhou et al. (2015), but the MSP M22A is off from the 95% error region (Fig. 6.4, yellow ellipse)³. The 95% error ellipse touches the half-mass radius of the cluster, but does not cover the cluster core. 3FGL J1837.3–2403 showed a power law spectrum with photon index 2.40 ± 0.14 and a flux in the 0.1–100 GeV range of $(8.7 \pm 1.7) \times 10^{-12}$ erg cm⁻² s⁻¹, consistent with the best-fit power law by Zhou et al. (2015). The corresponding γ -ray luminosity is $(10.6 \pm 2.1) \times 10^{33}$ erg s⁻¹, for a distance of 3.2 kpc. 3FGL J1837.3-2403 appears rather stable, as also indicated by the low variability index of 43.73 reported in the catalogue (see also Acero et al., 2015, for details on variability).

From the inspection of the preliminary 8-yr *Fermi*-LAT source list (FL8Y), we found that 3FGL J1837.3–2403 is associated to FL8Y J1836.7–2355, whose detection is at 6.45σ and at only $5.1'$ from the cluster centre. Though the 95% error ellipse is smaller (Fig. 6.4, green ellipse), it includes both the radio positions of the two MSPs M22A and M22B and obviously precludes a clear association to any of them.

While the present work was under review stage, the final 8-year catalogue (4FGL, The Fermi-LAT collaboration, 2019) was officially

³The other MSP identified by Lynch et al. (2011), M22B, does not fall in the 95% 3FGL J1837.3–2403 error ellipse either.

released. The new release refines the preliminary position of the FL8Y list. The closest source to M22 is 4FGL J1836.8–2354, detected at 8.2σ , at a distance of almost $6'$ from the cluster centre. Its 95% error region barely touches the cluster core and does not encompass M22A, neither at the radio or X-ray position, though it is very close (see Fig. 6.4, red ellipse)⁴. In the 4FGL catalogue the source spectrum is found to be best fit with a log-normal representation (LogParabola)⁵. The significance of the fit of a LogParabola over a power law is 4.2σ . The energy flux in the 0.1–100 GeV range is $(4.1 \pm 0.9) \times 10^{-12} \text{ erg cm}^{-2} \text{ s}^{-1}$ with a corresponding γ -ray luminosity of $(5.0 \pm 1.1) \times 10^{33} \text{ erg s}^{-1}$. The difference in flux between the 3FGL and 4FGL catalogues is consistent within 2σ .

6.7 Discussion

We have presented here a comprehensive study of the radio MSP M22A, located in the GC M22, from multiwavelength observations. We search for X-ray emission from M22A, taking into account all the available X-ray observations within the last two decades. Using the most recent *Chandra* observation of 2014, we detect an X-ray source whose 1σ positional uncertainty encompasses the radio source M22A and therefore we ascribe it as the X-ray counterpart of the radio MSP. Thanks to its ~ 85 ks of exposure time, the *Chandra* observation allows us to investigate the spectral shape and to determine the X-ray luminosity of the pulsar. We do not detect any X-ray emission from M22A in either

⁴The 95% elliptic region of 4FGL J1836.8–2354 does not encompass M22B either.

⁵See https://fermi.gsfc.nasa.gov/ssc/data/access/lat/8yr_catalog/.

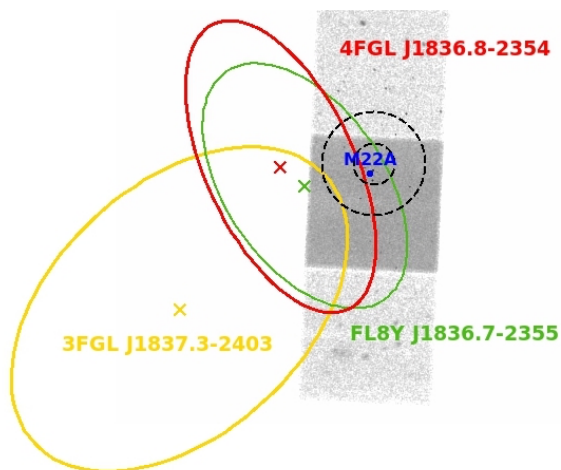


Fig. 6.4 γ -ray sources and 95% error ellipses from the 3FGL (in yellow, Acero et al., 2015), the preliminary FL8Y (in green) and the 4FGL (in red, The Fermi-LAT collaboration, 2019) catalogues of *Fermi*-LAT. The blue dot marks the radio position of the MSP M22A, while the black dashed circles the core radius (inner circle) and the half-mass radius (outer circle) of M22.

XMM-Newton or *Swift*/XRT pointings; the *Swift* monitoring campaign of the cluster, with one or two visits per month, shows that M22A remains likely around, or below, the luminosity derived in the *Chandra* observations.

We studied the X-ray spectrum of M22A by using the data from the two *Chandra* observations. We considered two possible scenarios: a non-thermal emission, originating from an intrabinary shock produced between the powerful pulsar wind and that from the companion star (Romani and Sanchez, 2016; Wadiasingh et al., 2017), and a thermal emission, which could originate in the polar caps of the NS, where the infall of relativistic particles keeps heating the pulsar surface (Gentile et al., 2014). Both the emission mechanisms are discussed below.

The X-ray spectrum can be reasonably fit with a relatively hard power-law ($\Gamma \sim 1.5$) which could hint at a non-thermal origin and favours the intrabinary shock scenario. In fact, the X-ray emission from the shock is expected to be hard with a power law shape with index 1.1 – 1.2 (Becker and Trümper, 1999; Zavlin, 2007). The X-ray flux and spectrum is also expected to be variable at the binary orbital period, as indeed found in most systems (Bogdanov et al., 2005; de Martino et al., 2015; Gentile et al., 2014; Roberts et al., 2015). Unfortunately, due to the low statistics, we could not infer any orbital modulation. We compare the photon index of M22A with those presented by Arumugasamy et al. (2015) for a sample of black widow pulsars (see also Gentile et al., 2014) and those of Linares (2014) for a sample of redbacks (see also Roberts et al., 2015; Strader et al., 2019), as shown in Fig. 6.5 (top panel). Though the photon index of M22A is

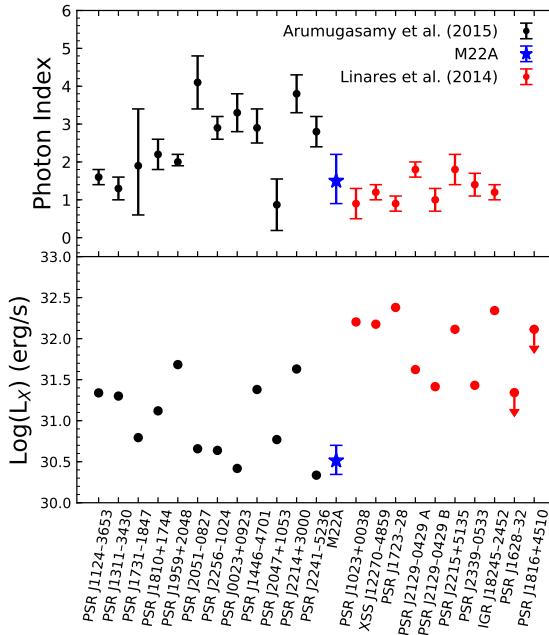


Fig. 6.5 Photon indices (*top panel*) and X-ray luminosities in the energy range 0.5-10 keV (*bottom panel*) of a sample of black widows (black) from Arumugasamy et al. (2015), redbacks (red) from Linares (2014) and our derived values for M22A (blue star).

poorly constrained, it is consistent with similar hard values found in a number of black widows and in all redbacks.

Thermal emission is often observed from faint MSPs, where the total power generated is $\log_{10}(L_x)=30-32 \text{ erg s}^{-1}$ (Bhattacharya et al., 2017; Bogdanov et al., 2006; Forestell et al., 2014) and the magnetic field is low, typically $B \lesssim 10^9 \text{ G}$ (Heinke et al., 2006; Zavlin et al., 1996). The intensity of the magnetic field at the surface of the NS, in the

simple case of a magnetic dipole, is given by $B_{\text{surf}} = 3.2 \times 10^{19} (P\dot{P})^{1/2}$ G (Manchester and Taylor, 1977), where P and \dot{P} are respectively the spin period and the spin-down rate of the NS. From Lynch et al. (2011), $P \simeq 3.35$ ms and $\dot{P} \simeq 5.36 \times 10^{-21}$ ss $^{-1}$, being \dot{P} the intrinsic spin-down of the pulsar, disentangled from the effect due to the potential of the Galaxy and of the proper motion of the cluster (Lynch et al., 2011, formula 9). Hence, $B_{\text{surf}} \sim 1.4 \times 10^8$ G, implying that the contribution of a thermal emission cannot be excluded.

The X-ray spectrum, indeed, could be equally described by a black-body with temperature of 0.8 ± 0.4 keV. It is perfectly consistent with the temperatures of other samples of X-ray pulsars (see, for instance, Bogdanov et al. (2006) and Bhattacharya et al. (2017) for a spectral analysis of the MSPs of the GC 47 Tucanae).

To argue more deeply about the thermal scenario, we can use the correlation between the X-ray luminosity and the rotational energy loss rate ($\dot{E} = 4\pi^2 I \dot{P} / P^3$), which is equal to $\sim 5.6 \times 10^{33}$ erg s $^{-1}$ for M22A. We compare our result with a sample of 24 MSPs (Gentile et al., 2014) in Fig. 6.6. Under the hypothesis that the rotational energy loss rate is converted in X-ray thermal emission from the polar caps with an efficiency of 0.1% (Pavlov et al., 2007) (*solid line* in Fig. 6.6), the thermal conversion mechanism would seem to be plausible for M22A. However, we underline that the best-fit value of the radius of the emitting polar cap, $R_{\text{eff}} = 6.5_{-4}^{+8}$ m (Tab. 6.2), is unrealistically small.

We derive an X-ray luminosity of $(2 - 3) \times 10^{30}$ erg s $^{-1}$, for the black-body and the power law models, respectively, in the energy range 0.5–8 keV. These values are consistent with the ones typically found for

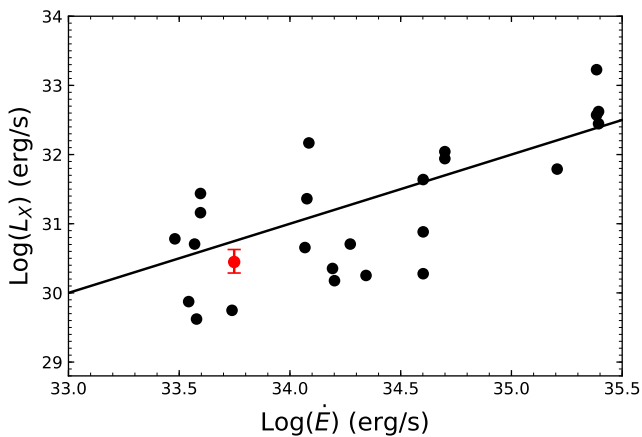


Fig. 6.6 Luminosity versus spin-down energy loss rate \dot{E} for 24 X-ray detected MSPs (black circles), from Gentile et al. (2014). The red dot stands for M22A. Luminosities are in the 0.3-8.0 keV range, while the line represents 0.1% efficiency.

GC X-ray sources ($L_X \sim 10^{30} - 10^{31} \text{ erg s}^{-1}$) (Bogdanov et al., 2006). On the base of the X-ray luminosity, we try to discriminate whether M22A is more likely a black widow or a redback. For this purpose, we made a comparison between the X-ray luminosities of the black widow pulsars from Arumugasamy et al. (2015) and of the redbacks from Linares (2014), as shown in the bottom panel of Fig 6.5 (for a wider sample consider also sources from Gentile et al. (2014), Roberts et al. (2015) and Strader et al. (2019)). Black widows luminosities are in the range $\log_{10}(L_X) = 30.2 - 31.3 \text{ erg s}^{-1}$, while redbacks luminosities seem to be sistematically higher, in the range $\log_{10}(L_X) = 31.5 - 33.7 \text{ erg s}^{-1}$. With a value of $\log_{10}(L_X) = 30.5 \text{ erg s}^{-1}$, in the range 0.5–10 keV, M22A is more consistent with black widows rather than with redbacks.

The persistent low X-ray flux does not favour accretion of matter from the companion star. The low companion mass and relatively large orbital period seem to indicate that mass accretion in this system is unlikely. The mass function of 2.6×10^{-6} indicates a companion star of mass $M_2 = 0.017 M_\odot$ for $i = 90^\circ$ (Lynch et al., 2011) and $M_2 = 0.22 M_\odot$ for $i = 5^\circ$. We exclude lower angles, being the probability of observing a binary system with an inclination $i < 5^\circ$ equal to $1 - \cos(i) \simeq 0.4\%$ (Lorimer and Kramer, 2004). Using $M_2 = 0.22 M_\odot$ as an upper limit, we consider a Roche-lobe overflow as possible mechanism of mass transfer. In this case the secondary star radius R_2 must be at least of the same order of magnitude of its Roche lobe radius R_L , therefore it is sufficient to compare the two radii R_2 and $R_{L,2}$. The size of the Roche lobes is $R_{L,2} = 0.49q^{2/3}/[0.6q^{2/3} + \ln(1 + q^{1/3})]a$ (Eggleton, 1983), where q is the ratio between M_2 and M_1 , the mass of the primary

star, and of the orbital separation a . We adopt a mass of $1.4 M_{\odot}$ for the NS and the range $0.02\text{--}0.2 M_{\odot}$ for the companion, according to the possible inclinations of the system. Using the third Kepler's law we derive an orbital separation a in the range $(1.14\text{--}1.16)\times 10^6$ km and, hence, $R_{L,2} = (1.2\text{--}2.7) \times 10^5$ km ($0.18\text{--}0.39 R_{\odot}$). On the other hand, an estimate of R_2 can be made according to the mass-radius relationships for low mass stars and sub-stellar objects by Chabrier et al. (2000) (see their Table 5); for an "old" object, with an age of ≈ 10 Gyr and a mass between 0.05 and $0.1 M_{\odot}$, the radius ranges between 0.08 and $0.12 R_{\odot}$, which is about the Jupiter radius. Since $R_2 < R_{L,2}$, the accretion of matter onto the NS through Roche-lobe overflow is ruled out.

However, it cannot be excluded that the companion star is out of thermal equilibrium and bloated with respect to its main sequence configuration (see, e.g., King, 1988). In this case, the companion star can be close to fill its Roche lobe and can transfer or loose mass (as it happens in red-backs and black widows) thanks also to the pulsar irradiation. In any case, we do not expect accretion in this phase of the system since the radiation pressure from the pulsar may be able to expel the mass transferred by the companion star out of the system (see, e.g., Burderi et al., 2001).

Even in the case of a lack of detection of an optical counterpart, we can derive some constraints on the nature of the companion of M22A. We compare the expected magnitudes for the case of maximum radii, i.e. Roche-lobe filling between 0.18 and $0.39 R_{\odot}$, adopting temperatures up to 3400 K. Here we note that no brown dwarf is ex-

pected to have temperatures above 3000 K and radius larger than $0.2 R_{\odot}$ even at 0.1 Gyr (Chabrier et al., 2000). The upper limits in the F606W and F814W filters derived from *HST*, once converted into the Johnson-Cousin system (Sirianni et al., 2005) and adopting an interstellar extinction $E(B-V)=0.34$ (Alonso-García et al., 2012) and the distance of 3.2 kpc, give absolute magnitudes of 12.5 and 11.6 in the V and I bands, respectively. These values are well above the evolutionary sequences of brown dwarfs by more than 3 mag in V and 1 mag in I (Chabrier et al., 2000). For R_2 between $0.18 R_{\odot}$ and $0.39 R_{\odot}$ and $T_{\text{eff}} = 3400$ K, the expected magnitudes are $V=13.3-10.8$ mag and $I=10.8-8.6$ mag, respectively. On the other hand, the limits in the V and I bands would correspond, for a similar temperature, to a stellar radius of $0.23 R_{\odot}$ and $0.16 R_{\odot}$. In the case of Roche-lobe filling, i.e. $R_2 = R_{L_2}$, adopting again $1.4 M_{\odot}$ for the NS, these radii would correspond to masses between 0.04 and $0.014 M_{\odot}$, respectively. Releasing the Roche-lobe filling condition, the magnitude limits and thus the corresponding upper limits to the radii give a main sequence star of $0.2 M_{\odot}$ and $0.1 M_{\odot}$ respectively (Baraffe et al., 2015). Therefore, although tentative, these estimate appears to rule out a companion with a mass above $0.1-0.2 M_{\odot}$. According to the recent study of Strader et al. (2019), redback companions have median masses of $0.36 \pm 0.04 M_{\odot}$, with a scatter of $\sigma=0.15 \pm 0.04 M_{\odot}$. Thus, our analysis may favour a black widow binary, in agreement with the interpretation of Lynch et al. (2011).

Concerning the γ -ray emission, the new position and uncertainty in the 8-year catalogue seem to exclude the contribution of the two MSPs

to the γ -ray emission of 4FGL J1836.8–2354, although the 95% error ellipse is only slightly offset from the two radio sources. The number of MSPs expected in the cluster can be estimated as $N_{\text{MSP}} = L_{\gamma} / \langle \dot{E} \rangle \langle \eta_{\gamma} \rangle$ (Abdo et al., 2010), where L_{γ} is the γ -ray luminosity of the cluster, $\langle \dot{E} \rangle$ is the average power loss during the spin down of MSPs and $\langle \eta_{\gamma} \rangle$ is the average conversion efficiency of the spin down power into γ -ray radiation. Assuming $\langle \dot{E} \rangle = (1.8 \pm 0.7) \times 10^{34} \text{ erg s}^{-1}$, $\langle \eta_{\gamma} \rangle = 0.08$ (Abdo et al., 2010) and $L_{\gamma} = 5 \times 10^{33} \text{ erg s}^{-1}$, we obtain $N_{\text{MSP}} \simeq 4$, i.e., we expect that the γ -ray emission seen from *Fermi* is the cumulative contribution of at least 4 MSPs. With only 2 radio MSPs detected in M22 so far, we are unable to assess their true contribution. The curved γ -ray spectrum, as reported in the 8-year *Fermi*-LAT catalogue, may be also compatible with an origin from pulsars (The *Fermi*-LAT collaboration, 2019).

6.8 Conclusions

We have carried out a search for the X-ray, optical and γ -ray counterparts of the radio MSP M22A, detected by Lynch et al. (2011). We find persistent X-ray emission in two *Chandra* observations, made in 2005 and 2014 respectively. The X-ray spectrum is well modeled either with a hard power law, with a photon index of ~ 1.5 , or with a black-body model with a temperature of $\sim 0.8 \text{ keV}$. In both cases, the resulting unabsorbed flux was $\sim 2 \text{ erg cm}^{-2} \text{ s}^{-1}$. However, the latter gives an unrealistic value of the effective polar cap radius, which makes the intrabinary shock scenario more likely than thermal emission from the NS surface. No optical counterpart has been found and the inferred

upper limits on the magnitudes allow us to derive an upper limit on the mass of the companion star of $0.2 M_{\odot}$, typical for black widow systems. No γ -ray emission from M22 core is found in the latest *Fermi*-LAT catalogues. Further studies of this X-ray source can be made with new generation of satellites, like *eRosita*, launched in 2019, *eXTP*, planned to flight earlier than 2027, and, of course, *Athena*.

With this regard, we performed a simulation with *Athena*/WFI to prove that this instrument will improve the quality of the data and to investigate whether and how a high soft proton flux can affect the scientific results. Starting from the best-fit power law model ($\Gamma = 1.5$), we simulate a new spectrum, using the most updated response and the background files for the WFI⁶. We used the background for an on-axis point-like source, with a $5''$ radius (equal to the WFI nominal psf), with the filter on. This background comprehends either the non-X-ray Background and the Celestial X-ray Background. We used the response file for an on-axis source, with the filter included. For an exposure of 10^5 s (of the same order of magnitude of the longest *Chandra* observation), we obtained a signal to noise ratio (S/N) of 19σ . The fit of the simulated data gave a precision of 11% in the photon index evaluation, with a significant improvement with respect to the best-fit value of the *Chandra* data ($\sim 50\%$). A fit with the black body model resulted in a $\chi_{red}^2(\text{d.o.f.}) = 2.286(27)$, against a $\chi_{red}^2(\text{d.o.f.}) = 1.015(27)$ for the power law model, thus allowing to distinguish clearly between the two models.

⁶Responses matrices and background file are available at https://www.mpe.mpg.de/ATHENA-WFI/response_matrices.html.

For the case of an increased soft proton component, we derived from Lotti et al. (2018) the soft proton spectrum for the model of an active magnetosphere and an exposure of the satellite to this flux equal to 90% of the overall time. Using the response matrix for the proton transmission at the focal plane of grazing incident telescopes (Lotti et al., 2018; Mineo et al., 2017), we obtained a soft proton spectrum that was added to the original background spectrum, where, according to the requirement, the soft proton component is only 10% of the non-X-ray background (i.e., 5×10^{-4} cts $\text{cm}^{-2} \text{s}^{-1} \text{keV}^{-1}$). This new simulation reduced the detection significance to 17σ , with no source signal above 5 keV, where the Fe $K\alpha$ line at 6.4 keV is typically found in many LMXBs. In this latter case, the best-fit photon index has a significance of 15%.

Chapter 7

Looking through the photoionisation wake: Vela X-1 at $\varphi_{\text{orb}} \approx 0.75$ with *Chandra*/HETG

7.1 Introduction

The eclipsing high-mass X-ray binary (HMXB) Vela X-1 (4U 0900-40) consists of a ~ 283 s period pulsar (McClintock et al., 1976) and a blue supergiant companion star (HD 77851, a B0.5Ia class star, Hiltner et al., 1972). With an X-ray luminosity of $\sim 4 \times 10^{36}$ erg s $^{-1}$ and a distance of ~ 2 kpc from Earth (Giménez-García et al., 2016), it is one of the brightest HMXBs in the sky. It is a high inclination system ($>73^\circ$, Joss and Rappaport, 1984), with an orbital period of ~ 8.9 d (Forman et al.,

1973; Kreykenbohm et al., 2008) and an orbital separation of about $53 R$ (Quaintrell et al., 2003). The donor star has a radius of $\sim 30 R$ (Quaintrell et al., 2003), so that the pulsar is constantly embedded in the wind environment of the companion. The geometry of the accreting stream of matter onto the compact object is complex, being made up of an accretion wake, a photoionisation wake, and possibly a tidal stream, as both simulations (e.g., Blondin et al., 1990; Manousakis, 2011) and observations in different wavebands show (e.g., Kaper et al., 1994; Malacaria et al., 2016; van Loon et al., 2001). A sketch of the binary system with the main features is given in Fig. 7.1. The line of sight intersects the different elements at different orbital phases, so that the observational data show strong changes in absorption along the whole orbital period (Doroshenko et al., 2013).

X-ray emission from Vela X-1 has already been detected and studied for several different orbital phases with different instruments (e.g., Fürst et al., 2010; Goldstein et al., 2004; Grinberg et al., 2017; Haberl and White, 1990; Watanabe et al., 2006). High-resolution X-ray studies of the system are of special interest, as they allow to draw conclusions on the properties of the complex plasma. High-resolution data from the High-Energy Transmission Grating Spectrometer (HETGS) (Canizares et al., 2005) of the *Chandra X-ray Observatory* (Weisskopf et al., 2000) of Vela X-1 during eclipse ($\varphi_{\text{orb}} \approx 0$) were studied by Schulz et al. (2002), who discovered and identified a variety of emission features, including radiative recombination continua (RRCs) and fluorescent lines, that led to the idea of the coexistence of a hot optically thin photoionised plasma and a colder optically thick one. Goldstein et al. (2004) investigated *Chandra*/HETGS data of the system at three different orbital

phases ($\varphi_{\text{orb}} \approx 0$, $\varphi_{\text{orb}} \approx 0.25$, $\varphi_{\text{orb}} \approx 0.5$), finding that the emission features revealed during the eclipse are obscured at $\varphi_{\text{orb}} \approx 0.25$, but then they appear again at $\varphi_{\text{orb}} \approx 0.5$, when the soft X-ray continuum diminishes. The simultaneous presence of H- and He-like emission lines and fluorescent lines of near-neutral ions can be originated in different regions: the warm photoionised wind of the companion star and smaller cooler regions, or clumps, of gas. Watanabe et al. (2006) compared the same *Chandra*/HETGS data sets to 3D Monte Carlo simulations of X-ray photons propagating through a smooth, undisturbed wind. Based on this assumption, they deduced that highly ionised ions, which give rise to the emission lines, are located mainly in the region between the neutron star (NS) and the companion star, while the fluorescent lines are produced in the extended stellar wind, from reflection of the stellar photosphere, and in the accretion wake. More recent results on the same orbital phase by Odaka et al. (2013) with *Suzaku* and by Martínez-Núñez et al. (2014) with *XMM-Newton*, respectively, highlighted flux variability and strong changes in absorption over periods of the order of ks. The same variability is found in *Chandra*/HETGS data at $\varphi_{\text{orb}} \approx 0.25$ from Grinberg et al. (2017), who attributed the changes in the overall absorption necessarily to the clumpy nature of the winds from the companion. Moreover, the high energy resolution of *Chandra* allowed the detection of line emission features from several ionised elements, corroborating the idea of a co-existence of cool and hot gas phases in the system.

Hydrodynamic simulations (El Mellah et al., 2019, 2018; Manousakis and Walter, 2015) suggest the presence of a more complex structure around the neutron star (NS), with a bow shock and eventually the for-

mation of a transient wind-captured accretion disk (Liao et al., 2020). Such features can influence the way clumps accrete onto the compact objects, i.e., reducing the amount of transferred angular momentum or introducing time lags and phase mixing when the clumps are stored in such structures.

In this work we present, for the first time, a high-resolution spectroscopic study of *Chandra*/HETG archival data of Vela X-1 at orbital phase $\phi_{\text{orb}} \approx 0.75$, i.e., when the line of sight is intersecting the photoionisation wake (see Fig. 7.1). The study of the X-ray spectrum at this specific orbital phase, where the absorption from the wind of the X-rays coming from the NS is high, allows the detection of a large number of lines from different elements in high ionisation states and, thus, the application of plasma diagnostic techniques to characterise the accretion environment. The paper is structured as follows: we first look for changes in the hardness of the flux in Section 7.2, finding none; then we proceed with a blind search for spectroscopic absorption/emission features, applying a Bayesian Block algorithm to the unbinned spectrum; we present the identification of all the detected features in Section 7.3, while in Section 7.4 we compare the observational data with two different photoionisation codes; in Section 7.5 we discuss the plasma properties and the geometry of the wind of the companion star; in Section 7.6 we perform simulations with future X-ray satellites; we present our conclusions in Section 7.7.

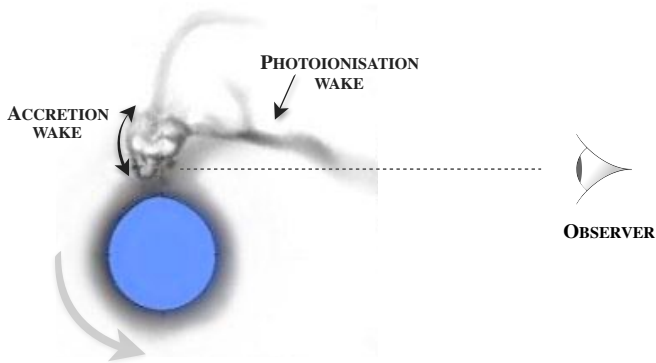


Fig. 7.1 A sketch of Vela X-1 from Grinberg et al. (2017) showing the accretion and photoionisation wakes. The blue circle represents the donor star HD 77851, while the pulsar is hidden in the accretion wake. The grey arrow indicates the verse of the rotation of the binary system. At the orbital phase $\varphi_{\text{orb}} \approx 0.75$, the observer is looking at the system from the right, so that the line of sight (dashed line) is crossing the photoionisation wake.

7.2 Data reduction and temporal analysis

We analysed the High Energy Grating (HEG) and Medium Energy Grating (MEG) data sets of the *Chandra*/HETG ObsID 14654, taken on 2013-07-30, with ACIS-S, in FAINT mode, for a total exposure time of 45.88 ks. According to the ephemeris of Kreykenbohm et al. (2008), the data set covers the orbital phase $\varphi_{\text{orb}} = 0.72 - 0.78$, where $\varphi_{\text{orb}} = 0$ is defined as mid-eclipse. Data were reprocessed using CIAO 4.11, with CALDB 4.8.2. We followed the standard *Chandra* data analysis threads, but we chose a narrower sky mask to avoid the overlapping of the extraction region and to improve the flux at the shortest wavelengths.

Following the work of Grinberg et al. (2017), who observed a change in the hardness of the source during phase $\varphi_{\text{orb}} \approx 0.25$, we extracted the light curve in two different energy bands, 0.5–3 keV (soft) and 3–10 keV (hard), and computed the hardness ratio, defined as the ratio between the counts in the hard band over the soft one. Fig. 7.2 shows the result, with data binned to the NS spin period of 283 s (errors at 1σ). The hardness ratio values at $\varphi_{\text{orb}} \approx 0.75$ are higher than the ones obtained by Grinberg et al. (2017) by at least a factor of ten, which is not surprising considered the high absorption expected at this orbital phase. Moreover, the hardness ratio is almost flat for the whole observation, in contrast to Grinberg et al. (2017), where a variability of a factor of three was observed. Hence, we extract only one spectrum, in the full energy range of 0.5–10 keV (Fig. 7.3).

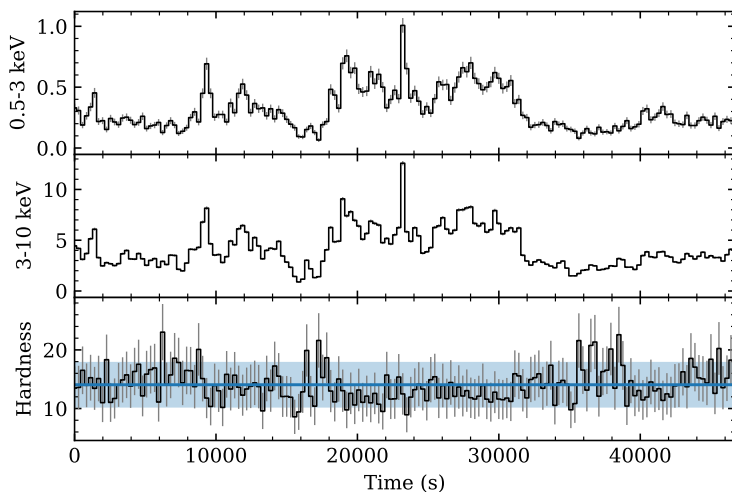


Fig. 7.2 Light curves in units of counts s^{-1} , in the soft 0.5-3 keV (*top panel*) and hard 3-10 keV (*middle panel*) energy bands, and corresponding hardness ratio $((3-10 \text{ keV})/(0.5-3 \text{ keV}))$, (*bottom panel*). The blue horizontal line indicates the mean value of the hardness ratio, with the 1σ uncertainty given by the blue area. Data are binned to the spin period of 238 s, error bars at 1σ .

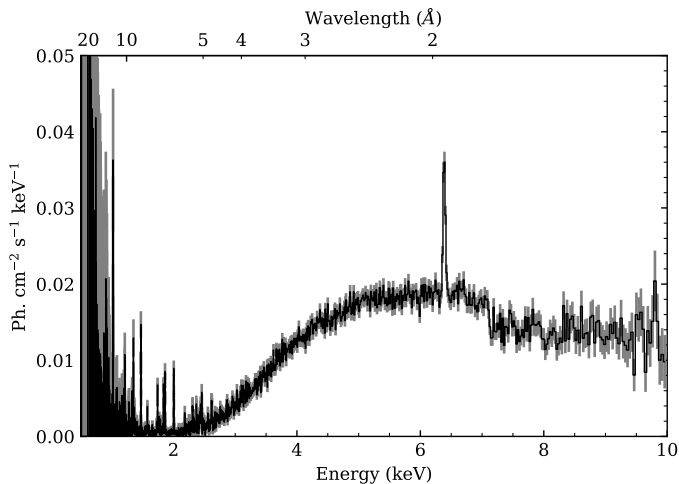


Fig. 7.3 Combined HEG and MEG spectrum of *Chandra* ObsID 14654 in the energy range 0.5-10 keV.

7.3 High-resolution spectroscopy

We used the Interactive Spectral Interpretation System (ISIS) 1.6.2-43 (Noble and Nowak, 2008a,b) to perform the spectroscopic analysis of the data, with the ISIS functions (ISISscripts) provided by ECAP/Remeis observatory and MIT¹, cross sections from Verner et al. (1996), and solar abundances from Wilms et al. (2000). We used Cash statistic (Cash, 1979) with the spectrum binned to the MEG resolution. All uncertainties are given at 90% confidence level.

We performed a blind search of spectral features, using a Bayesian Block (BB) algorithm (Scargle et al., 2013), as described in Young et al. (2007) and as applied to *Chandra*/HETGS data by Grinberg et al.

¹<http://www.sternwarte.uni-erlangen.de/isis/>.

(2017). To optimize the line detection algorithm, we divided the whole spectrum into five regions of interest, named after the most significant element detected in each of them, as reported in Tab. 7.1. These spectral regions were analysed one by one. We locally modelled the continuum with a simple power law and then looked for significant deviations in the residuals. The algorithm determines whether a data point is far from the model above a certain significant threshold, defined by a parameter, α , such that each detection has a significance of $p \sim \exp(-2\alpha)$, corresponding to a probability of $P \sim 1 - \exp(-2\alpha)$ of positive detection. For each new detection, we added to the model one or more Gaussian components for emission/absorption lines and the XSPEC (Arnaud, 1996) functions `redge` and `edge` for the RRCs and the Fe K-edge (Sect. 7.3.1, 7.5.1), respectively. After each addition, we fit the data and apply the algorithm once more. We iterate the process until the significance drops to 95%, corresponding to $\alpha \sim 1.5$. All the line detections with their corresponding values of α are listed in Tabs. 7.2–7.6, while Tab. 7.1 shows the best-fit values of the power law parameters for each spectral region and the goodness of the fit. Tab. 7.7 displays the best-fit values of the RRCs.

In some cases, lines that are too close to be clearly resolved by the algorithm, such as for example He-like triplets, are detected as a single block. In such cases, we use our knowledge of atomic physics to add the proper number of lines to the model. To improve the fit, we fixed the distance of known lines, such as the H-like $\text{Ly}\alpha$ and $\text{Ly}\beta$ lines (Erickson, 1977) and the He-like triplets (Drake, 1988), assuming that Doppler shifts are the same within the same ionic species. Whenever a line appeared unresolved, we fixed its width to 0.003 \AA , corresponding

to about one third of the MEG resolution (0.023 \AA FWHM)². Line identification for S and Si ions accounts for the most recent laboratory measurements from Hell et al. (2016), while for the other elements we use the AtomDB database³ (Foster et al., 2012, 2017).

For every detected He-triplet, we computed the density-sensitive ratio $R = f/i$ and the temperature-sensitive ratio $G = (i + f)/r$, where f represents the intensity of the forbidden line ($1s2s \ ^3S_1 - 1s^2 \ ^1S_0$), i the intensity of the intercombination line ($1s2p \ ^3P_1 - 1s^2 \ ^1S_0$) and r the intensity of the resonant line ($1s2p \ ^1P_1 - 1s^2 \ ^1S_0$) (Gabriel and Jordan, 1969; Porquet and Dubau, 2000)⁴. In our case, the intensities of the lines are linked to reproduce G and R as free parameters in the fit. Results are reported in Tab. 7.8.

In the following subsections, we present in detail the results of the BB procedure for each spectral region of interest.

7.3.1 Iron region

In the Fe region (wavelength range $1.6\text{-}2.5 \text{ \AA}$, cf. Tab. 7.1), the BB method found only one strong line that we identify with an Fe $K\alpha$ emission line (cfr. Sec. 7.5.1, for the corresponding ionisation stage) and one edge, identified with the Fe K-edge. Best-fit values for these features are reported in Tab. 7.2. Although the strong Fe $K\alpha$ line

²http://cxc.harvard.edu/cdo/about_chandra.

³<http://www.atomdb.org/index.php>.

⁴Gabriel (1972) refers to the transitions of the lines of the He-like triplets as w for the resonant line, x and y for the two components of the intercombination line and z for the forbidden line. With this notation, the ratios for plasma diagnostic are expressed as $R = z/(x + y)$ and $G = (z + (x + y))/w$.

Table 7.1 Best-fit values of the power laws used to model the continuum and values of the Cash statistic per degrees of freedom (d.o.f.) for each region of the spectrum.

Region	Wavelength range (Å)	Γ	Norm. ($\text{keV s}^{-1} \text{cm}^{-2}$)	Cash(d.o.f.)
Fe	1.6–2.5	$-0.082^{+0.004}_{-0.008}$	$0.0158^{+0.0023}_{-0.0018}$	1.03(179)
S	4.5–6.0	-5.38 ± 0.05	$(1.04^{+0.06}_{-0.16}) \times 10^{-5}$	1.14(279)
Si	6.0–7.4	-0.3 ± 0.1	$(3.4 \pm 0.2) \times 10^{-4}$	1.19(247)
Mg	7.5–10.0	$2.31^{+0.15}_{-0.16}$	$(1.27 \pm 0.07) \times 10^{-3}$	1.26(468)
Ne	10.0–14.5	0.1 ± 0.7	$(6.9^{+0.7}_{-0.6}) \times 10^{-4}$	0.99(892)

Table 7.2 Features detected in the Fe region (1.6–2.5 Å) with the detection parameter α and the best-fit values. The width of the Fe K α line was fixed to 0.003 Å.

Line	BB α	Ref. wavelength (Å)	Det. wavelength (Å)	Line flux ($\text{ph s}^{-1} \text{cm}^{-2} \times 10^{-4}$)	τ
Fe K α	157	1.9375 ^a	1.9388 ± 0.0006	9.4 ± 0.8	–
Fe K edge	47	1.7433 ^b	1.742 ± 0.003	–	0.31 ± 0.03

Notes. ^(a) Drake (1988). ^(b) Bearden and Burr (1967).

implies the presence of a strong Fe K β component, our approach did not detect it. We discuss the possible reasons in Sect. 7.5.

Given the overall strength of the Fe K α line, we attempted an additional fit, letting the line width free, instead of fixing it to 0.003 Å. We obtained a best-fit value of $\sigma = (3.4^{+0.9}_{-1.1}) \times 10^{-3}$ Å, consistent with our previous assumption and with results by Tzanavaris and Yaqoob (2018).

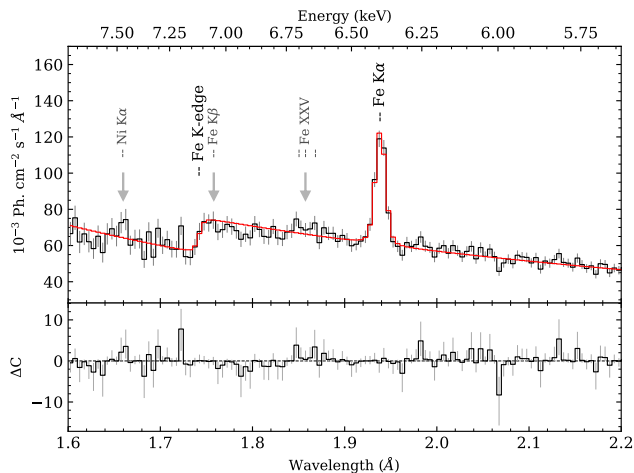


Fig. 7.4 Fe-region spectrum and best-fit model (red line), with residuals shown in the bottom panel. The only line detected by the BB algorithm is identified and marked as a FeK α emission line, as well as the detected Fe K-edge. Arrows mark the position of the expected Ni K α , Fe K β and He-like Fe XXV lines (in grey).

7.3.2 Sulphur region

We studied the S region in the wavelength range 4.5-6.0 Å (Tab. 7.1). Line identification is based on the recent laboratory measurements from Hell et al. (2016). The BB algorithm detected a single block between 5 Å and 5.4 Å, with $\alpha = 27$. We model this block with the S XV He-like triplet, the S XIV, the S XI and the blended fluorescence S II-VIII lines. The second run of the algorithm resulted in the detection of the S XVI Ly α , with $\alpha = 12$. Lastly, three more lines were detected: the Si XIII He β ($\alpha = 8$), the S IX ($\alpha = 2.7$) and an unidentified absorption line at ~ 5.457 Å ($\alpha = 2.2$). No reference wavelength was found for this

very last absorption line. Considering the low value of the parameter α and the lack of any other absorption feature in the whole spectrum, it is most likely that the line is just a statistical fluctuation.

In the same region we could also expect to find the Si XIV Ly β line, at 5.217 Å (Erickson, 1977). The lack of a significant detection of this line is probably due to the high continuum. However, since the Si XIV Ly α line is strong in the Si region (see Sect. 7.3.3), the Si XIV Ly β is most likely present and blended with the S XI line. In Fig. 7.5, we marked the line at 5.224 Å with both its possible identifications.

For this region, all the line widths were fixed to 0.003 Å. Best-fit values are reported in Tab. 7.3, together with the Doppler velocities computed with respect to laboratory reference values (Hell et al., 2016). Fig. 7.5 shows the spectrum, the best-fit model and the residuals of the fit. From the S XV triplet, we obtained the best-fit ratios $R = 9.9^{+2.4}_{-2.2}$ and $G = 0.48^{+0.14}_{-0.10}$ (Tab. 7.8).

7.3.3 Silicon region

We searched for Si lines in the region 6.0-7.4 Å (Tab. 7.1). The BB algorithm highlighted at the first trial ($\alpha = 190$) the Si XIV Ly α line and a whole block in the range 6.6-6.8 Å that we modelled with the He-like triplet Si XIII, at first. The fluorescent line blend Si II-VI is detected with $\alpha = 121$, while a whole block is detected at the wavelengths 6.9-7.1 Å, with $\alpha = 32$. We added three Gaussians to model this block, according to the laboratory measurements by Hell et al. (2016) (see also Grinberg et al., 2017), corresponding to the Si VII, Si VIII and Si IX lines. The last detections are identified as the Al XIII Ly α line ($\alpha = 9$), the Si X and Si XI lines ($\alpha = 5$) and the Si XII line ($\alpha = 1.8$).

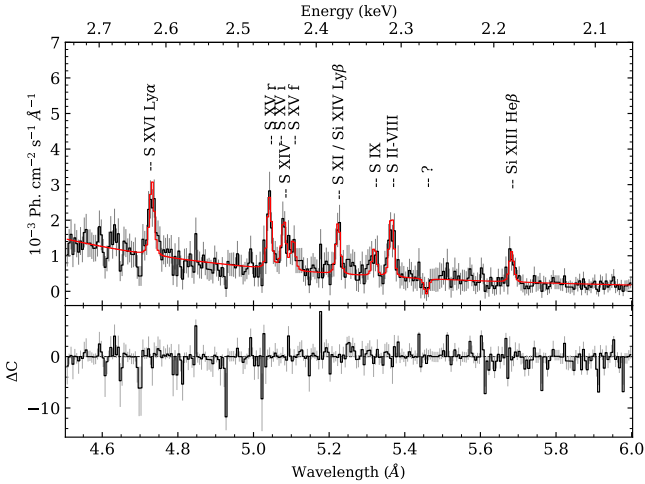


Fig. 7.5 S-region spectrum and best-fit model (red line), with residuals shown in the bottom panel. The detected lines are labelled if identified.

In the same region, also the RRC of Mg XII is detected, at a wavelength of 6.321 \AA ($1.961 \pm 0.002 \text{ keV}$), with a temperature of $4.5_{-2.5}^{+5.8} \text{ eV}$. Lastly, we added one more redden function to model the Mg XI RRC, expected at 7.037 \AA (Drake, 1988). It results in a temperature of $3.1_{-1.1}^{+1.6} \text{ eV}$, consistent with the one of Mg XII RRC.

The width of the lines was fixed to 0.003 \AA , except for the Si XIV Ly α line, which has a slightly larger width of $(7.3_{-1.1}^{+1.2}) \times 10^{-3} \text{ \AA}$. For each line, we computed the Doppler velocities with respect to the laboratory or literature reference wavelengths. All the best-fit values of the emission lines and RRCs are reported in Tab. 7.4 and Tab. 7.7, respectively, while the spectrum, the best-fit model and the residuals are shown in Fig. 7.6. The best-fit values of the R and G ratios of the S XIII triplet resulted in $R = 6.0 \pm 0.6$ and $G = 0.80_{-0.09}^{+0.10}$ (Tab. 7.8).

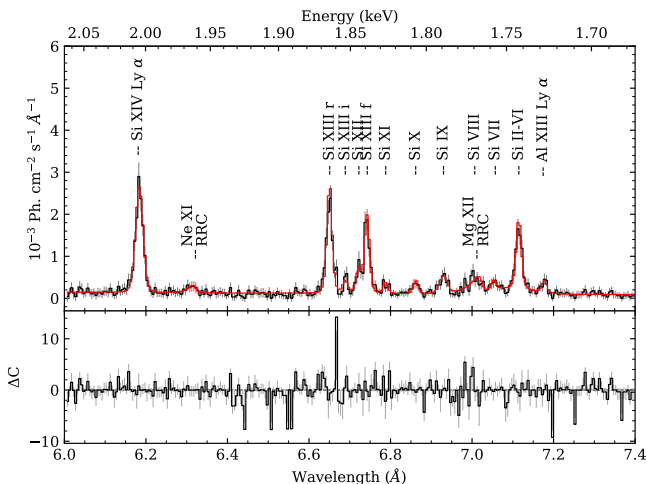


Fig. 7.6 Si-region spectrum and best-fit model (red line), with residuals shown in the bottom panel.

The BB algorithm did not detect the Mg XII Ly β emission line expected at $\sim 7.1037 \text{ \AA}$ (Erickson, 1977). Also in this case, the line is most likely embedded in the (near-)neutral fluorescence Si II-VI lines.

7.3.4 Magnesium region

The region we took into account to look for Mg emission lines ranges from 7.5 \AA to 10 \AA (Tab. 7.1). The first line detected corresponds to the Mg XII Ly α ($\alpha = 220$). The successive detection ($\alpha = 89$) consisted in a block in the range $\sim 9-9.4 \text{ \AA}$, which we modelled with three Gaussians for the He-like triplet Mg XI. In the same block, we insert the Ne X RRC (Goldstein et al., 2004; Schulz et al., 2002; Watanabe et al., 2006). We also detected and identified the Mg XI He β ($\alpha = 48$), the Ne X Ly γ

($\alpha = 15$), the Al XII *r* He α ($\alpha = 7$), the Ne X He δ ($\alpha = 4.4$), the Fe XX ($\alpha = 3.4$), and the Fe XXIV ($\alpha = 2.9$) emission lines. Best-fit values are reported in Tab. 7.5, while the spectrum, the best-fit model, and the residuals are shown in Fig. 7.7. A few lines show a broadening that required to let their widths free. This is the case for Mg XII Ly α whose width of $(7.4 \pm 1.2) \times 10^{-3}$ Å is in agreement with those of Si XIV (Sect. 7.3.3) and Ne X Ly α (Sect. 7.3.5) lines. Other broadened lines are the Mg XI *r* and the Ne X He δ , ~ 0.01 Å width, and a Fe XXIII line (~ 0.025 Å width). The Ne X RRC, at a wavelength of ~ 9.116 Å ($1.3600^{+0.0012}_{-0.0010}$ keV) indicates a temperature of $10.8^{+3.4}_{-2.5}$ eV (Tab. 7.7) consistent with previous findings at different orbital phases (Goldstein et al., 2004; Schulz et al., 2002). Doppler shifts of the Ly α , the He β and the triplet lines are around 150 km s^{-1} . From the intensities of the Mg XI triplet we obtained the ratios $R = 1.20^{+0.25}_{-0.23}$ and $G = 0.74^{+0.13}_{-0.14}$ (Tab. 7.8) for plasma diagnostic.

7.3.5 Neon region

The region for Ne emission lines goes from 10 Å to 14.5 Å (Tab. 7.1). We detected and identified 11 lines and two RRCs. Best-fit values are reported in Tab. 7.6 and 7.7, the spectrum, best-fit model, and residuals are shown in Fig. 7.8. The first line to be detected by the BB procedure ($\alpha = 49$) was the Ne X Ly α , at a wavelength of 12.1398 Å and with a width of $(9.6^{+3.0}_{-2.8}) \times 10^{-3}$ Å. The successive detection ($\alpha = 29$) was a line at ~ 10.24 Å, that we identified with the Ne X Ly β . Hence, we fixed the distance of the latter line with respect to the corresponding Ly α according to Erickson (1977). The next detection ($\alpha = 17$) was a block from 13.4 Å to 13.9 Å, that we modeled with the Ne IX triplet (Goldstein

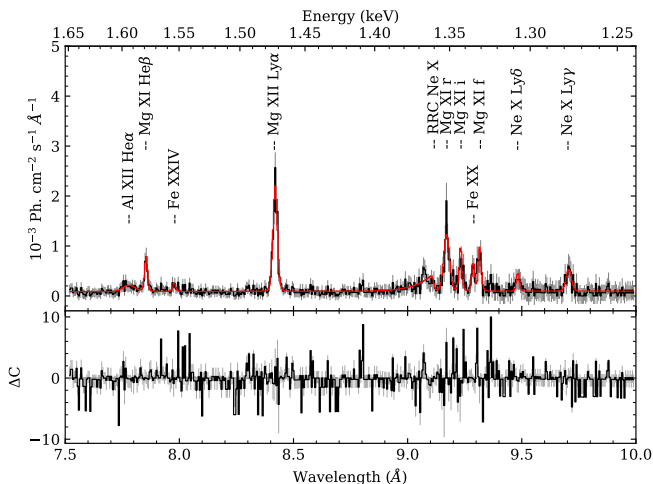


Fig. 7.7 Mg-region spectrum and best-fit model (red line), with residuals shown in the bottom panel.

et al., 2004; Grinberg et al., 2017; Watanabe et al., 2006). Lastly, we detected six more lines, corresponding to Ne IX He β , at 11.549 Å ($\alpha = 8$), Ne IX He γ at 11.005 Å ($\alpha = 7$), Ne IX He ϵ at 10.644 Å ($\alpha = 3.2$), Na XI Ly α at 10.023 Å ($\alpha = 2.5$), Fe XIX at 10.814 Å ($\alpha = 1.8$) and Fe XXI at 12.285 Å ($\alpha = 1.7$). The Ne IX RRC at 10.374 Å was detected with $\alpha = 8$ and resulted in a best-fit temperature of $4.5^{+3.4}_{-2.1}$ eV, while the O VIII RRC at 14.22 Å was detected with $\alpha = 2.8$ with a best-fit temperature of $0.9^{+4.2}_{-0.6}$ eV (Tab. 7.7). This is the first detection of the O VIII RRC for Vela X-1 in *Chandra* data. It was implied in ASCA observations (Sako et al., 1999), suggested by Schulz et al. (2002), and only recently detected using *XMM-Newton* data (Lomaeva et al., 2020). We note that the O VIII RRC might be also blended with a Fe XVIII line at 14.208 Å (Brown et al., 1998).

We computed Doppler shifts for all the lines, obtaining velocities consistent with each other (Tab. 7.6). The intensities of the lines of the Ne IX triplet gave diagnostic best-fit ratios of $R = 1.2^{+0.6}_{-0.5}$ and $G = 3.7^{+4.4}_{-1.7}$ (Tab. 7.8).

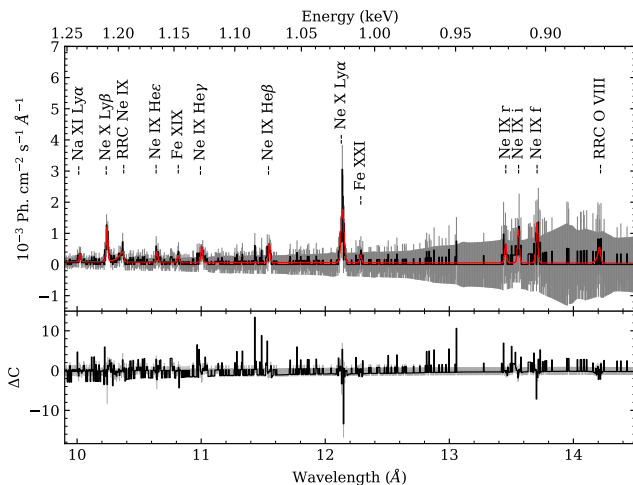


Fig. 7.8 Ne-region spectrum and best-fit model (red line), with residuals shown in the bottom panel.

7.4 Photoionisation models with CLOUDY and SPEX

We attempted a more physical modelling of the detected features using photoionisation models with the latest release of CLOUDY (Ferland et al., 2017) and SPEX (v3.05, Kaastra et al. 1996, Kaastra et al. 2018). In both cases we used proto-Solar abundances from Lodders et al.

(2009). Both these codes require an input ionising continuum. We approximated such a continuum with a sum of two components, as previously done in Grinberg et al. (2017) and Lomaeva et al. (2020). The emission from the star, that dominates in the UV, was modelled with a black body, while the emission from the accretion onto the NS with a power law modified by a Fermi-Dirac cutoff. Both components have the same parameters as employed in Lomaeva et al. (2020). In particular, the shape of the power law continuum cannot be well constrained at energies below 10 keV, especially when strongly affected by absorption, as is the case with our observations. We thus used parameters derived from non-simultaneous *NuSTAR* observations (Fürst et al., 2014). We note that there are some indirect hints that the illuminating continuum assumed here may not reflect the true continuum seen by the plasma in the system, such as, in particular, the large ratio between the Fe and Si/S fluorescence lines and the stability curves, which are unstable over wide ranges, especially at the ionization parameters of interest. This emphasizes the importance of strictly simultaneous observations at high resolution below 10 keV and at energies above this range for the future.

In our modelling, we investigate the electron density n_e (cm^{-3}), the ionisation parameter ξ (erg cm s^{-1}), the absorption coefficient N_{H} (10^{22} cm^{-2}), and the turbulent velocity v_{turb} (km s^{-1}). We explored the parameter space with CLOUDY in the ranges $5.0 \leq \log n_e \leq 11.5$, $0.0 \leq \log \xi \leq 4.0$, $20.9 \leq \log N_{\text{H}} \leq 22.3$, and $80 \text{ km s}^{-1} \leq v_{\text{turb}} \leq 160 \text{ km s}^{-1}$. For SPEX we assume a much larger parameter space since its PION model calculates the ionisation balance instantaneously and does not require a predefined grid of models.

We modeled our observed spectrum with an absorbed partially covered power law, with spectral index $\Gamma = 1$, corresponding to the input power law of our photoionisation models (Fürst et al., 2014), in addition to the CLOUDY/SPEX model. The absorption due to the interstellar medium was fixed to $3.7 \times 10^{21} \text{ cm}^{-2}$ (HI4PI Collaboration et al., 2016), the local absorption is left free to vary. We added three more Gaussians for the fluorescence Fe $K\alpha$ line, centered at 1.9388 \AA (cfr. Sect. 7.4), and for the near-neutral fluorescence emission lines of S II-VIII and Si II-VI, which are not reproduced by CLOUDY and SPEX.

The best-fit CLOUDY model resulted in $\log n_e = 8.180 \pm 0.017$, $\log \xi = 3.610 \pm 0.007$, with $N_H = (1.600 \pm 0.008) \times 10^{22} \text{ cm}^{-2}$ and a turbulent velocity of $159_{-16}^{+2} \text{ km s}^{-1}$. The model required a redshift, with a best-fit value of $z \sim 10^{-4}$, corresponding to a velocity of $v \sim 100 \text{ km s}^{-1}$, consistent with the Doppler shifts previously obtained. The Cash(d.o.f.) statistic value was 1.58(2584). The modelling of the whole spectrum with SPEX resulted in the best-fit values of $\log \xi = 3.867_{-0.009}^{+0.005}$ and $N_H = (4.3 \pm 0.3) \times 10^{21} \text{ cm}^{-2}$, with a line broadening of $160 \pm 16 \text{ km s}^{-1}$ and a Cash(d.o.f.) value of 1.57(2382). Also in this case the model is redshifted with respect to the data, with a best-fit velocity along the line of sight of $130_{-20}^{+15} \text{ km s}^{-1}$. Best fits are shown in Fig. 7.9.

We noticed that the electron density n_e is degenerate with the absorption of the interstellar medium (ISM): the larger the ISM N_H , the larger the n_e (see discussion in Sect. 7.5.2).

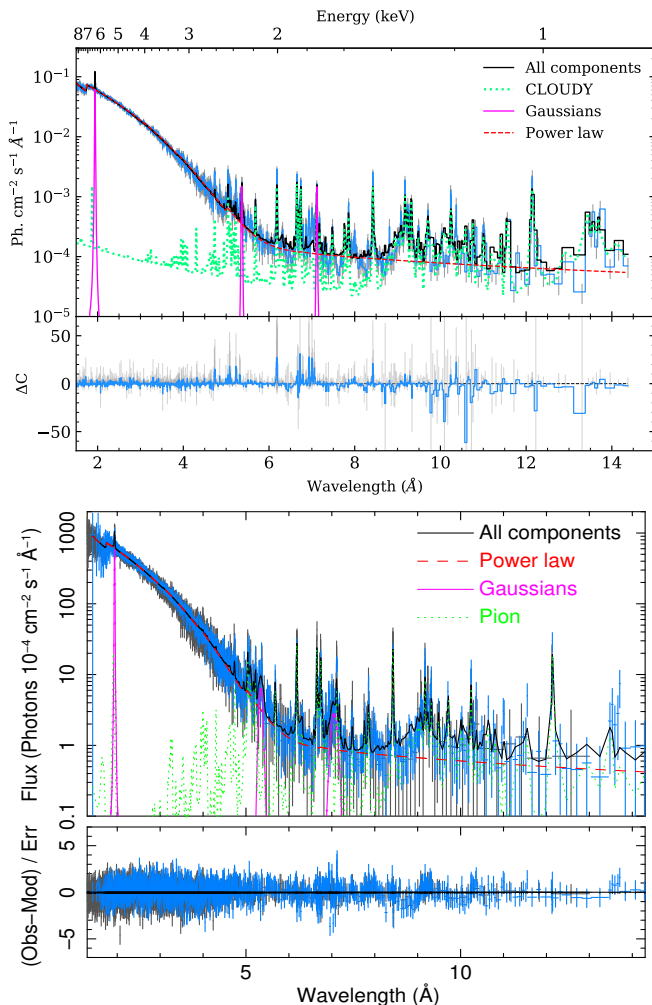


Fig. 7.9 Fit of the whole spectrum with the photoionisation model (dotted green line) from CLOUDY (*top panel*) and SPEX (*bottom panel*), plus a partially covered power law (dotted red line), and three Gaussians for the fluorescence lines of Fe K α , S II-VIII, and Si II-VI (solid magenta lines). The total fit function is represented in black. Spectra rebinned for an easy comparison.

7.5 Discussion

We performed, for the first time, high-resolution spectroscopy analysis of *Chandra*/HETGS data of Vela X-1 at the orbital phase $\phi_{\text{orb}} \approx 0.75$. A first look at the hardness ratio (Fig. 7.2) revealed no significant continuum spectral variability during the observation. The mainly flat shape of the hardness ratio is not surprising, since the line of sight at this orbital phase is expected to lie well within the photoionisation wake, a denser stream-like region that trails the NS (Doroshenko et al., 2013; Malacaria et al., 2016) and acts as a constant absorber (see Fig.7.1).

The analysis pointed out the presence of Fe, S, Si, Mg and Ne, as well as of less intense emission lines from Al and Na. Contrary to previous observations (Goldstein et al., 2004; Schulz et al., 2002; Watanabe et al., 2006), there is no evidence of the presence of Ar ($\lambda \sim 3.359 \text{ \AA}$), Ca ($\lambda \sim 4.186 \text{ \AA}$) and Ni ($\lambda \sim 1.660 \text{ \AA}$) fluorescence lines. Upper limits of their fluxes resulted in $5.2 \times 10^{-5} \text{ ph s}^{-1} \text{ cm}^{-2}$ for Ar, $2.3 \times 10^{-5} \text{ ph s}^{-1} \text{ cm}^{-2}$ for Ca and $3.1 \times 10^{-4} \text{ ph s}^{-1} \text{ cm}^{-2}$ for Ni.

In the next subsections, we discuss in details the Fe region (Sect. 7.5.1), carry out plasma diagnostic (Sect. 7.5.2) and investigate the geometry of the wind of the companion star (Sect. 7.5.3).

7.5.1 The Iron complex

The Fe region (1.6–2.5 \AA) is dominated by a Fe $K\alpha$ line, centered at $1.9388 \pm 0.0006 \text{ \AA}$. Assuming no Doppler shift for the line, the corresponding maximum ionisation state is Fe X (Palmeri et al., 2003), consistent with the results of Grinberg et al. (2017) (lower than Fe XII),

and different from the case of an irradiated wind, as showed by the hydrodynamical simulations of Sander et al. (2018) (where the wind is mainly driven by Fe III ions). However, the line may be redshifted so that a higher ionization state could be expected. A more refined calculation is well beyond the goal of this work.

The only other one relevant feature detected in this region is the Fe K-edge at $1.742 \pm 0.003 \text{ \AA}$ (see Tab. 7.2), which is not significantly Doppler shifted.

The BB algorithm did not detect the Fe K β line, expected at $\sim 1.758 \text{ \AA}$, most likely because of the proximity of the Fe K-edge. However, since the average flux ratio between the Fe K β and Fe K α lines is 0.13–0.14 (Palmeri et al., 2003, for the charge states Fe II–IX), we can estimate an expected flux of $(1.32 \pm 0.11) \times 10^{-4} \text{ ph cm}^{-2} \text{ s}^{-1}$, which might not be sufficient to let the line emerge from the continuum underneath. To verify this assertion, we generated 1000 Monte Carlo simulated spectra adding to the best-fit model a Gaussian at the correspondent wavelength of the Fe K β with the expected flux. We then run the BB algorithm on all the simulated spectra (cf. Sect. 7.3.1). In no case the line was detected, confirming its weakness with respect to the X-ray continuum and the K-edge, which precluded a detection in the observational data. The Fe K β /K α ratio depends on the ionization of iron (see the detailed discussions in Molendi et al. (2003) and Bianchi et al. (2005)). For higher charge states, the expected line ratio is even smaller, i.e., the Fe K β line would be even weaker than what our simulation showed as undetectable. Therefore, we cannot rule out that the ionization state is higher than what we assumed. We discuss the prospects of detecting Fe K β with future instruments in Sect. 7.6.

Results from Goldstein et al. (2004) at $\phi_{\text{orb}} \approx 0$ and $\phi_{\text{orb}} \approx 0.5$ show, in the same spectral region, the presence of the Ni Ly α line at $\lambda \sim 1.660 \text{ \AA}$, while Schulz et al. (2002) propose the presence of a Fe XXV emission line at $\lambda \sim 1.85 \text{ \AA}$ ($\phi_{\text{orb}} \approx 0$). The BB procedure did not detect any feature at those wavelengths, but after a visual inspection, we noted a marginal presence of residuals in emission. So we add two more Gaussians to the best-fit model of the Fe region, at $\lambda \sim 1.66 \text{ \AA}$ and $\lambda \sim 1.86 \text{ \AA}$, for the Ni Ly α and a Fe XXV respectively, and fit the spectrum again. The Fe XXV is actually a He-like triplet, but the resolution of the MEG of 0.023 \AA FWHM, adopted consistently through the paper, is not good enough to resolve the lines individually. Hence, we use just one Gaussian to fit the whole ion, letting the width free to vary. The width of the Ni Ly α line was fixed to the usual value of 0.003 \AA . The fluxes of these latter Gaussians resulted in $(1.8^{+1.3}_{-1.2}) \times 10^{-4} \text{ ph cm}^{-2} \text{ s}^{-1}$ for the Ni Ly α and $(3.1 \pm 1.2) \times 10^{-4} \text{ ph cm}^{-2} \text{ s}^{-1}$ for the Fe XXV lines, while the width of the He-like Fe XXV had a best-fit value of $0.018^{+0.013}_{-0.007} \text{ \AA}$.

From the Fe edge (Tab. 7.2), we computed the equivalent hydrogen column expressed as $N_{\text{H}} = \tau_{\text{edge}} / (Z_{\text{Fe}} \sigma_{\text{Fe}})$, where $Z_{\text{Fe}} = 2.69 \times 10^{-5}$ is the solar Fe abundance (Wilms et al., 2000) and $\sigma_{\text{Fe}} = 3.4 \times 10^{-20} \text{ cm}^2$ is the photoelectric absorption cross section for Fe XXV at the wavelength of the K-edge (Verner et al., 1996). Using the best-fit value optical depth $\tau_{\text{edge}} = 0.31 \pm 0.03$, we derive $N_{\text{H}} = (3.4 \pm 0.3) \times 10^{23} \text{ cm}^{-2}$, which is nearly consistent with the best-fit value of $N_{\text{H}} = (2.68 \pm 0.07) \times 10^{23} \text{ cm}^{-2}$ obtained fitting the spectrum in this region with a simple absorbed power law, with solar abundances and cross sections as specified in Sect. 7.3. These values are of the same order of magnitude

as the best-fit values found for observations using *MAXI* (Matsuoka et al., 2009) by Doroshenko et al. (2013) and *NuSTAR* (Harrison et al., 2013) by Fürst et al. (2014) at the same orbital period. However, we must bear in mind here that the model we used does not account for the Fe $K\beta$ line, which may contribute to larger uncertainties on the Fe K-edge parameters.

7.5.2 Plasma properties

The presence of five narrow RRCs (Mg XI, Mg XII, Ne IX, Ne X, and O VIII) suggests that the plasma is photoionised, with a temperature between ~ 1 and 10 eV ($(1 - 12.5) \times 10^4$ K), as reported in Tab. 7.7. A further indication of a photoionised plasma might be the value of $G = 3.7_{-1.7}^{+4.4}$ of the Ne IX triplet (Tab. 7.8), consistent with 4 in spite of the large uncertainties (Porquet and Dubau, 2000).

However, the G ratios of S XV ($G = 0.48_{-0.10}^{+0.14}$), Si XIII ($G = 0.80_{-0.09}^{+0.10}$) and Mg XI ($G = 0.74_{-0.14}^{+0.13}$) are all smaller than 1, indicating that collisional processes are not negligible and may even dominate (Porquet and Dubau, 2000; Porquet et al., 2010). Under the hypothesis of a collisional equilibrium plasma (CIE), we can estimate the temperature from the G ratio values (see, e.g., Porquet and Dubau, 2000). From the He-like Si XIII and Mg XI triplets we obtain temperatures of $\sim 1 \times 10^7$ K (861 eV) and $\sim 7 \times 10^6$ K (603 eV), respectively, which are two orders of magnitude higher than the ones from the Ne RRCs.

This inconsistency between temperatures derived from the RRCs and the He-like line ratios is likely due the known issue that relative level populations between the upper levels of the He-like triplet lines

can be shifted by other physical phenomena, which are likely present in HMXBs, thus making the G ratio unreliable.

In particular, two processes can enhance a resonant r line stronger than the intercombination i or forbidden f lines: photoexcitation and resonance line scatter. Photoexcitation can be important in photoionisation equilibrium (PIE) plasma, when many photons with the right energy excite the electrons to the resonant level. This clearly enhances the resonance line and, then, alters the G ratio with respect to the pure recombination case (see the comprehensive explanation in Kinkhabwala et al., 2002). The presence of a few weak iron L emission lines (Fe XIX-XXIV) also seems to point in this direction (Sako et al., 2000).

Resonant line scattering occurs when a photon is absorbed and re-emitted in the same wavelength, but in the direction of the lowest optical depth. This phenomenon is well explained by Wojdowski et al. (2003) for the HMXB Centaurus X-3, observed during eclipse. In the case of Vela X-1, though we are not in the eclipsing phase, the dense streams of matter surrounding the NS can act as a strong absorber, enhancing the resonance line scattering into the line of sight.

Concerning the R ratio, the values of Mg XI ($R = 1.2^{+0.3}_{-0.2}$) and Ne IX ($R = 1.2^{+0.6}_{-0.5}$) He-like lines implies an electron density of the plasma of $\sim 2 \times 10^{13} \text{ cm}^{-3}$ and $\sim 1.5 \times 10^{12} \text{ cm}^{-3}$, respectively, considering a plasma temperature of $7 \times 10^6 \text{ K}$ and $2 \times 10^6 \text{ K}$, as previously estimated⁵. On the other hand, the R ratios of Si XIII ($R = 6.0 \pm 0.6$) and S XV ($R = 9.9^{+2.4}_{-2.2}$) are much higher than the respective values at the

⁵We note here that the R ratio depends upon the relative ionic abundance of the H-like and He-like ions (χ_{ion} parameter), but in the range of our interest the dependence is so small that we can neglect it (see Fig. 9 of Porquet and Dubau, 2000).

low density limit, when the relative intensities of the He-like lines are in fact independent of the electron density of the plasma. In the case of Si, for instance, the low density limit value is $R = 3$, corresponding to a maximum density of the order of 10^{12} cm^{-3} (Porquet and Dubau, 2000), which can be addressed here as upper limit. On the other hand, the fit with CLOUDY and SPEX photoionisation models highlighted the degeneracy of the electron density n_e with the model chosen for the continuum, and, in particular, with the absorption from the ISM. The best-fit value of $n_e = 1.5 \times 10^8 \text{ cm}^{-3}$, for instance, can be treated only as a lower limit. The analysis underlines that the estimate of the density is pulled between the R ratio and the continuum and the real value is somewhere in between those limits.

Also the UV radiation of the companion star can alter the plasma (the so-called “UV-pumping” mechanism, Blumenthal et al., 1972; Gabriel and Jordan, 1969; Mewe and Schrijver, 1978; Porquet et al., 2001). UV radiation mimics a high density plasma, favouring the population of the 3P levels against the 3S_1 level, leading to an increase of the intensity of the intercombination line, against the forbidden line and, hence, to smaller values of the R ratio. The influence of the UV emission is taken into account in both, CLOUDY and SPEX based photoionisation models, through our choice of the continuum. Such models should also, if applicable to the given data at all, give better constraints on the underlying plasma parameters than the more empirical consideration of G and R ratios. The quality of our fits in Sect. 7.4 imply that this is the case.

Overall, both the self-consistent photoionisation codes provided a satisfactory fit of the data (Fig. 7.9), implying that, at this specific

orbital phase, the plasma is mainly photoionised. However, a closer inspection at the residuals hints to the presence of at least another phase of the plasma. The near-neutral emission lines of S II-VIII and Si II-VI, as well as the Fe $K\alpha$ line are not reproduced by the photoionisation models that are driven by the presence of highly ionized lines. This naturally suggests that the plasma cannot be a single component plasma.

In a possible scenario, colder and denser clumps of plasma, from either the wind or larger scale accretion structures such as wakes, can cross unevenly the line of sight, adding to the PIE emission of the wind of the companion star a further component with a lower ionization. Our data do not allow to constrain the origin of this component that could be, for example, a further, colder PIE component, a collisionally ionized component or a more complex mix with a temperature gradient as is the case, e.g., in Cyg X-1 (Hirsch et al., 2019). We also note that our results emphasize the necessity of an accurate treatment of intermediate and low ionization ions in atomic codes used for high resolution X-ray spectroscopy.

7.5.3 Wind geometry

Doppler velocities at different orbital phases can reveal the location and dynamics of the line emitting material. Fig. 7.10 shows the velocities for the ions of Si VI-IX from Schulz et al. (2002) and Goldstein et al. (2004) at the orbital phases $\phi_{\text{orb}} \approx 0$ and $\phi_{\text{orb}} \approx 0.5$, adjusted with respect to the laboratory measurements of Hell et al. (2016), together with the ones from Grinberg et al. (2017) at the orbital phase $\phi_{\text{orb}} \approx 0.25$ and with those in the present work ($\phi_{\text{orb}} \approx 0.75$). Velocities at $\phi_{\text{orb}} \approx 0.25$ are negative (blueshift), while velocities at the other

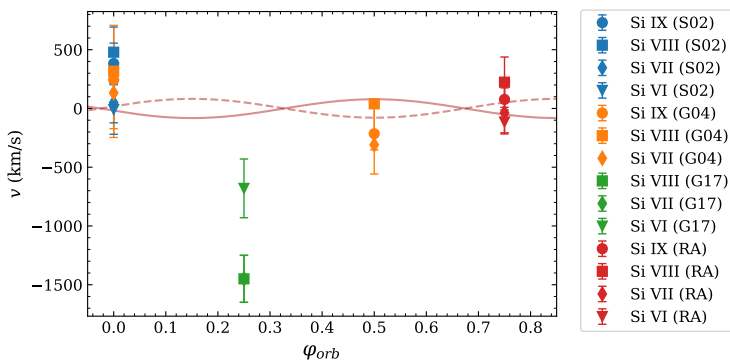


Fig. 7.10 Doppler velocities at different orbital phases of Si IX (circles), Si VIII (squares), Si VII (diamonds) and Si VI (reverse triangles), from Schulz et al. (2002) (S02, *blue*) and Goldstein et al. (2004) (G04, *orange*), as adjusted for laboratory reference values by Hell et al. (2016), from Grinberg et al. (2017) (G17, *green*) and from the present work (RA, *red*). The solid and dashed lines stand for the radial velocities of the NS and the giant star, respectively.

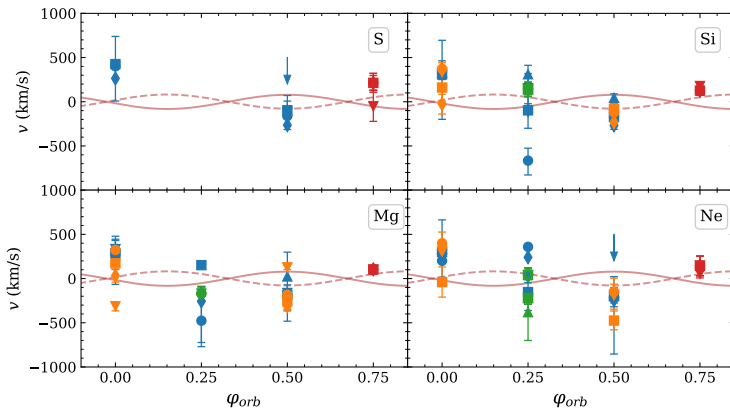


Fig. 7.11 Doppler velocities at different orbital phases of Ly α lines and He-like triplets of S, Si, Mg and Ne from Schulz et al. (2002) (*blue*) and Goldstein et al. (2004) (*orange*), from Grinberg et al. (2017) (*green*) and from the present work (*red*). Different symbols stands for different ionisation stages. The solid and dashed lines represent the radial velocities of the NS and of the companion star, respectively.

orbital phases are positive (redshift) and/or consistent with no shift. The same behaviour is observed also for all the others lines of S, Si, Mg and Ne (Fig. 7.11), even though there are no recent laboratory measurements that allow us to validate the Doppler shifts found by the previous studies (Goldstein et al., 2004; Grinberg et al., 2017; Schulz et al., 2002; Watanabe et al., 2006). Most of the velocities are consistent with the radial velocity of the NS, as well as of the companion star (solid and dashed lines in Figs. 7.10-7.11), computed as $v_{rad} = 2\pi a \sin i [\cos(\vartheta + \omega) + e \cos \omega] / (T\sqrt{1 - e^2})$, where a is the semimajor axis, i is the inclination, T is the orbital period, e is the eccentricity, ϑ and ω are the true anomaly and the argument of periapsis, respectively.

The overall behaviour is consistent with the material co-moving with the NS, though the lack of more observational data for each orbital phase prevent us to assert it definitively. However, this behavior has already been observed for the black hole HMXB Cygnus X-1 (Hirsch et al., 2019; Miškovičová et al., 2016), where the Doppler shifts show a clear modulation with the orbital phase. It has already been suggested for Vela X-1 that the wind velocity at the distance of the NS is $\sim 100 \text{ km s}^{-1}$ and lower than typically estimated from prescribed simple β -laws (Sander et al., 2018). The large spread in the range of observed Doppler shifts within the same orbital phases may be due radiation coming from regions further downstream the wind or due to a more complex velocity structure in the accretion region.

7.6 Future perspectives with *XRISM/Resolve* and *Athena/X-IFU*

High-resolution spectroscopy is a powerful tool to study X-ray emission from any kind of astrophysical plasma. Currently, the only limitations of X-ray satellites are due to their intrinsic resolution and sensibility. New generation X-ray satellites will go beyond these limits. The X-Ray Imaging and Spectroscopy Mission (*XRISM*, formerly *XARM*, Tashiro et al., 2018) and the Advanced Telescope for High Energy Astrophysics (*Athena*, Nandra et al., 2013) will host on-board microcalorimeters with an energy resolution down to a few eV, thus exceeding the resolution of the *Chandra* gratings in the Fe K region.

We performed simulations of this region (1.6–2.2 Å, see Sect. 7.5.1), including the Fe K-edge and the Fe K α as detected in the *Chandra* observation, and the Fe K β , the He-like Fe XXV and the Ni K α with the upper limit on the flux as in Sect. 7.5.1. Both microcalorimeters should be able to resolve the Fe K α doublet and the Fe XXV triplet. To assess this in more detail, the input spectrum of our simulation included two Gaussians for the Fe K α , at 1.9399 Å for the Fe K α_1 and at 1.9357 Å for Fe K α_2 , respectively, with a 1:2 ratio (Kaastra and Mewe, 1993), and four Gaussians for the Fe XXV, with line centroids as in Drake (1988) and a flux ratio of 2:1:1:2 ($w:x:y:z$). The width of all the lines was fixed to 0.0007 Å (~ 2 eV).

XRISM will be provided with the soft X-ray spectrometer *Resolve*, with a nominal energy resolution of 5–7 eV in the 0.3–12 keV bandpass. We used the ancillary and response files of *Hitomi/SXS* (Kelley et al., 2016) for the energy resolution requirement of 7 eV. Simulations show

that an exposure of only 300 s (comparable with the pulse period of 293 s) is sufficient to clearly detect the Fe $K\beta$ line with a significance of $\alpha = 1.8$, corresponding to 83% of positive detection probability, with a measured Fe $K\beta/K\alpha$ ratio of $0.17_{-0.09}^{+0.11}$. With an exposure of 2.5 ks, the probability of a positive detection of the Fe $K\beta$ line raises up to $> 99.99\%$ ($\alpha = 22$). The Fe $K\alpha$ doublet is resolved, while amongst the lines of Fe XXV only the f line is clearly resolved.

Athena will be equipped with the X-ray Integral Field Unit (X-IFU, Barret et al., 2018), a cryogenic X-ray spectrometer working in the energy range 0.2–12 keV, with a nominal energy resolution of 2.5 eV up to 7 keV. Moreover, thanks to the higher collecting area of *Athena* (1.4 m² at 1 keV), high quality spectra will be acquired in much shorter exposures. Also for the *Athena/X-IFU*, we simulated the Fe region with an exposure of 300 s, for time-resolved spectroscopy purposes, considering the pulse period of the NS of 293 s (Fig. 7.12). Running the BB algorithm on the simulated spectrum, the $K\beta$ line is detected with $\alpha = 9$, corresponding to 99.99% probability of positive detection. If the exposure times is increased up to 2.5 ks, then the $K\beta$ line is detected with a significance of $\alpha = 69$. The measured intensity ratio between the Fe $K\beta$ and Fe $K\alpha$ is $0.16_{-0.08}^{+0.10}$. The Fe $K\alpha$ doublet is fully resolved, as well as the f line of Fe XXV. The i line, which is made by two lines ($(x+y)$) in the nomenclature of Gabriel, 1972), is partially resolved, with the most energetic one blended with the r line.

Athena's capabilities will significantly improve also plasma diagnostic, even at shorter exposures. To test how well we can determine R and G ratios, we performed simulations with *Athena/X-IFU* at different exposure times. Fig. 7.13 shows the ratios of the Si regions at different

exposures, in comparison with the ratios obtained from the analysis of the 45.88 ks *Chandra*/HETGS observational data set. With an exposure of only 2.5 ks the uncertainties on R and G are reduced of the $\sim 50\%$. Longer exposures reduce consistently the errors on R and G , from $\sim 10\%$ up to 2% of their absolute values.

Overall, the achievement of good-quality spectra with such short exposure times implies that the lines can be traced on shorter timescales, i.e., of the same order of magnitude as the pulsar period. Moreover, because of *Athena*'s resolution, the energy of the Fe $K\alpha$ line can be better constrained so that we can be able to determine the ionisation stage of iron with a higher precision. It is clear, then, that upcoming satellites will considerably improve the knowledge of HMXBs, of stellar winds and, in general, of any kind of astrophysical plasma, as well remarked by XRISM Science Team (2020).

7.7 Conclusions

We conducted, for the first time, X-ray high-resolution spectroscopy of Vela X-1 at the orbital phase $\phi_{\text{orb}} \approx 0.75$, i.e., when the line of sight is intersecting the photoionisation wake that trails the neutron star along the orbit.

The data did not show any significant variability of the continuum for the duration of the observation. A blind search for spectral features led us to detect emission lines from Fe, S, Si, Mg, Ne, and, to a lesser degree, from Al and Na. We clearly detected and identified five narrow RRCs (Mg XI-XII, Ne IX-X, O VIII) and He-like triplets of S, Si, Mg and Ne.

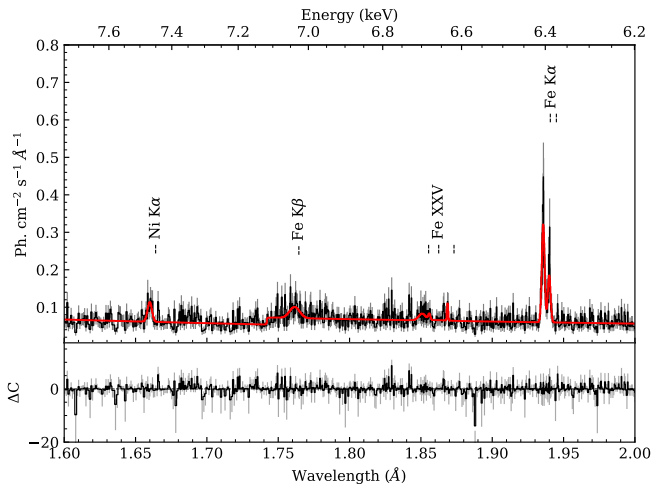


Fig. 7.12 Simulated spectrum of the Fe region with the *Athena*/X-IFU and best-fit model, with residuals in the lower panel. Exposure time of 300 s, data binned with a minimum of 15 counts/bin.

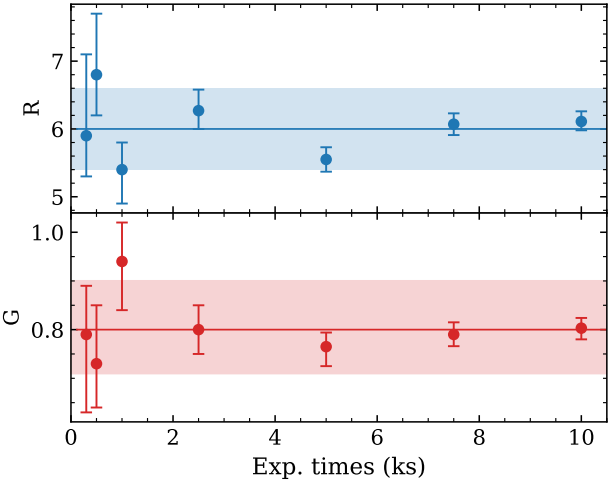


Fig. 7.13 R and G ratios for the He-like triplet of Si as obtained from simulations with *Athena*/X-IFU with different exposure times. Solid lines correspond to the best-fit values with the error ranges given by the colored areas obtained from the present work.

From plasma diagnostic techniques and from fits with photoionisation models from CLOUDY and SPEX, we conclude that the plasma at this orbital phase is mainly photoionised, but data suggest the presence of at least another component, with a smaller ionisation parameter. The presence of a collisional component cannot be excluded, as well as a mixture of ionised and collisional phases. This is in agreement with the idea of colder and denser clumps of matter, embedded in the hot, optically-thin wind of the donor star. The complex geometry of the system is also reflected by the spread of the distribution of the Doppler velocities.

The future X-ray instruments *Athena*/X-IFU and *XRISM*/Resolve will considerably enhance the detection and the resolution of spectral features. We showed through simulations that, thanks to higher energy resolutions, they will resolve single lines in the Fe $K\alpha$ doublet and Fe XXV triplet and, thanks to higher collecting areas, allow for plasma diagnostic for time scales as short as few hundreds of seconds.

Table 7.3 Spectral features detected in the S region. For each feature we report the detection parameter α , the best-fit values (wavelength and line flux) and the Doppler velocities, computed using reference wavelengths measured by Hell et al. (2016). Line widths fixed to 0.003 Å for all the lines.

Line	BB	Ref. wavelength (Å)	Det. wavelength (Å)	Line flux (10^{-5} ph s $^{-1}$ cm $^{-2}$)	Velocity (km s $^{-1}$)
S XVI Ly α	12	4.7329 ^a	4.731 \pm 0.003	3.5 $^{+1.0}_{-0.9}$	-50 $^{+180}_{-170}$
S XV <i>r</i>	27	5.0386	5.0422 $^{+0.0018}_{-0.0014}$	3.18 $^{+1.07}_{-0.99}$	210 $^{+110}_{-80}$
S XV <i>i</i>	27	5.0666	5.0682 $^{+0.0018}_{-0.0014}$ ^b	0.14 \pm 0.03	= $v_{(S XV r)}$
S XV <i>f</i>	27	5.1013	5.1049 $^{+0.0018}_{-0.0014}$ ^b	0.06 $^{+0.04}_{-0.07}$	= $v_{(S XV r)}$
S XIV	27	5.0858	5.081 \pm 0.003	2.3 \pm 0.8	-310 $^{+180}_{-160}$
S XI/Si XIV Ly β ^c	27	5.2250	5.224 \pm 0.002	2.3 $^{+0.8}_{-0.7}$	-70 \pm 140
S IX	2.7	5.3163	5.320 $^{+0.006}_{-0.009}$	1.3 $^{+0.8}_{-0.7}$	210 $^{+340}_{-510}$
S II-VIII	27	5.3616	5.365 \pm 0.003	2.8 $^{+0.9}_{-0.8}$	200 \pm 150
	2.2	-	5.457 $^{+0.002}_{-0.003}$	-0.69 $^{+0.011}_{-0.24}$	-
Si XIII He β	8	5.681 ^d	5.683 \pm 0.003	1.4 $^{+0.6}_{-0.5}$	80 $^{+150}_{-160}$

Notes. Hell et al. (2016) reports the statistical uncertainties for each energy, which correspond to an error in wavelength of the order of 10^{-4} – 10^{-5} Å. However, authors state that there is also a systematic uncertainty of 0.23 eV for S lines, which results in an error on the wavelength of 0.0008 Å.

^a Garcia and Mack (1965). ^b Distances between the *r* line and the *i* and *f* lines computed from Drake (1988). ^c The reference wavelength of Si XIV Ly β is 5.217 Å (Erickson, 1977).

^d Kelly (1987).

Table 7.4 Spectral features detected in the Si region. For each of them, we report the detection parameter α , the best-fit values (wavelength and line flux). Line widths fixed to 0.003 \AA , if not stated otherwise. Doppler velocities of the Si lines, computed with respect to the reference wavelengths measured by Hell et al. (2016).

Line	BB α	Ref. wavelength (\AA)	Det. wavelength (\AA)	Line flux ($\text{ph s}^{-1} \text{ cm}^{-2} \times 10^{-5}$)	Velocity (km s^{-1})
Si XIV Ly α	190	6.1817 ^a	6.184 ± 0.001	6.2 ± 0.6^b	100 ± 50
Si XIII <i>r</i>	190	6.6483	6.6506 ± 0.0007	$4.5^{+0.8}_{-0.7}$	100 ± 30
Si XIII <i>i</i>	190	6.7195	6.6887 ± 0.0007^c	$0.51^{+0.05}_{-0.04}$	$= v_{(\text{Si XIII } r)}$
Si XIII <i>f</i>	190	6.7405	6.7427 ± 0.0007^c	3.1 ± 0.4	$= v_{(\text{Si XIII } r)}$
Si XII	1.8	6.7197	6.722 ± 0.003	0.9 ± 0.3	110 ± 110
Si XI	5	6.7841	6.788 ± 0.004	$0.42^{+0.18}_{-0.16}$	170 ± 180
Si X	5	6.8558	6.862 ± 0.004	$0.49^{+0.19}_{-0.17}$	270 ± 180
Si IX	32	6.9279	6.930 ± 0.003	1.1 ± 0.3	80 ± 120
Si VIII	32	7.0008	7.006 ± 0.005	1.6 ± 0.3	220 ± 210
Si VII	32	7.0577	$7.057^{+0.005}_{-0.004}$	0.5 ± 0.2	-40^{+210}_{-170}
Si II-VI ^d	121	7.1172	7.115 ± 0.001	2.6 ± 0.4	-120 ± 40
Al XIII Ly α	9	7.1764 ^e	7.177 ± 0.003	0.6 ± 0.2	20^{+110}_{-120}

Notes. Hell et al. (2016) report a systematic uncertainty of 0.13 eV for Si lines, corresponding to an error on the wavelength of 0.0005 \AA .

^a Garcia and Mack (1965). ^b This line results in a best line width of $7.3^{+1.2}_{-1.1} \times 10^{-3} \text{ \AA}$.

^c Distances between the *r* line and the *i* and *f* lines computed from Drake (1988).

^d The Mg Ly β (7.1037 \AA , Erickson, 1977) might be blended with the Si II-VI line.

^e Erickson (1977).

Table 7.5 Spectral features detected in the Mg region (7.5-10 Å). For each of them, we report the detection parameter α , the best-fit values (wavelength and line flux) and the Doppler velocities, computed with respect to reference wavelength from literature. Line widths fixed to 0.003 Å, if not stated otherwise.

Line	BB α	Ref. wavelength (Å)	Det. wavelength (Å)	Line flux (ph s ⁻¹ cm ⁻² × 10 ⁻⁵)	Velocity (km s ⁻¹)
Al XII He α	7	7.7573 ^a	7.782 ^{+0.012} _{-0.011}	0.9 ± 0.3 ^b	960 ⁺⁴⁶⁰ ₋₄₃₀
Mg XI He β	48	7.850 ^c	7.8565 ± 0.0017	1.2 ± 0.3	250 ± 70
Fe XXIV	2.9	7.985 ^d	7.980 ^{+0.008} _{-0.005}	0.30 ^{+0.17} _{-0.14}	-190 ⁺³⁰⁰ ₋₁₉₀
Mg XII Ly α	220	8.42101 ^e	8.4226 ± 0.0011	5.3 ^{+0.6f} _{-0.5}	180 ± 40
Mg XI <i>r</i>	89	9.16896 ^a	9.1728 ± 0.0015	3.7 ± 0.8 ^g	130 ± 50
Mg XI <i>i</i>	89	9.2312 ^a	9.2343 ± 0.0015 ^a	1.51 ^{+0.14} _{-0.23}	= $v_{(\text{Mg XI } r)}$
Mg XI <i>f</i>	89	9.3143 ^a	9.3188 ± 0.0015 ^a	1.5 ± 0.4	= $v_{(\text{Mg XI } r)}$
Fe XX ^h	3.4	9.282 ⁱ	9.290 ± 0.004	1.0 ± 0.4	260 ± 130
Ne X Ly δ	4.4	9.481 ^e	9.485 ± 0.006	0.6 ± 0.3	130 ± 190
Ne X Ly γ	15	9.708 ^e	9.708 ± 0.005	1.3 ^{+0.5j} _{-0.4}	0 ± 150

Notes. ^a Drake (1988). ^b Line width of 0.025^{+0.012}_{-0.008} Å.

^c Kelly (1987). ^d Wargelin et al. (1998). ^e Erickson (1977). ^f For this line the best-fit line width value was $(7.4 \pm 1.2) \times 10^{-3}$ Å. ^g Line width of 0.011 ± 0.003 Å. ^h Close to the same wavelength there is also the Ne X Ly ζ emission line at 9.291 Å, but with a lower intensity ratio. In this case the resulting Doppler velocity would be (-32 ± 129) km s⁻¹.

ⁱ Unpublished atomic data from Liedahl (1997). ^j Line width of 0.010^{+0.005}_{-0.004} Å.

Table 7.6 Spectral features detected in the Mg region (10-14 Å). For each of them, we report the detection parameter α , the best-fit values (wavelength and line flux) and the Doppler velocities, computed with respect to reference wavelength from literature. Line widths fixed to 0.003 Å, if not stated otherwise.

Line	BB α	Ref. wavelength (Å)	Det. wavelength (Å)	Line flux ($\text{ph s}^{-1} \text{cm}^{-2} \times 10^{-5}$)	Velocity (km s^{-1})
Na XI Ly α^a	2.5	10.023 ^b	10.023 ± 0.005	0.5 ^{+0.3} _{-0.2}	0 ± 150
Ne X Ly β	29	10.23887 ^c	10.2408 ± 0.0017 ^d	2.1 ^{+0.6} _{-0.5}	60 ± 50
Ne IX He ϵ^e	3.2	10.643 ^b	10.644 ± 0.006	0.7 ^{+0.4} _{-0.3}	30 ± 170
Fe XIX	1.8	10.816 ^b	10.814 ^{+0.006} _{-0.005}	0.4 ^{+0.3} _{-0.2}	-60 ⁺¹⁷⁰ ₋₁₄₀
Ne IX He γ^f	7	11.001 ^g	11.005 ^{+0.006} _{-0.007}	1.0 ^{+0.5} _{-0.4}	110 ⁺¹⁶⁰ ₋₁₉₀
Ne IX He β^h	8	11.544 ^g	11.549 ^{+0.005} _{-0.006}	2.1 ^{+0.6} _{-0.5}	130 ⁺¹³⁰ ₋₁₆₀
Ne X Ly α	49	12.132 ^c	12.1398 ± 0.0017	5.3 ^{+1.2} _{-1.1} ⁱ	190 ± 40
Fe XXI	1.7	12.284 ^b	12.285 ^{+0.008} _{-0.007}	0.5 ^{+0.5} _{-0.4}	20 ⁺²⁰⁰ ₋₁₇₀
Ne IX <i>r</i>	17	13.4476 ^j	13.454 ± 0.005	1.3 ^{+1.6} _{-0.7}	140 ± 110
Ne IX <i>i</i>	17	13.553 ^j	13.557 ± 0.005	2.2 ^{+0.8} _{-0.6}	= $v_{(\text{Ne IX } r)}$
Ne IX <i>f</i>	17	13.699 ^j	13.706 ± 0.005	2.6 ^{+1.6} _{-1.3}	= $v_{(\text{Ne IX } r)}$

Notes. ^a Possible line blends include Fe XX at 10.024 Å and Ni XXIV at 10.027 Å.

^b Reference wavelength taken from AtomDB database (<http://www.atomdb.org/index.php>).

^c Erickson (1977). ^d Computed from the Ne X Ly α best-fit wavelength, as from Erickson (1977).

^e Another possible identification is the Fe XIX at 10.648 Å. ^f Possible line blends are: Fe XX at 11.007 Å, Na X HeI at 11.003 Å and Fe XIX at 11.002 Å. ^g Kelly (1987). ^h Another possible line is Fe XX at 11.546 Å. ⁱ Best-fit value of the line width of $(9.6^{+3.0}_{-2.8}) \times 10^{-3}$ Å.

^j Drake (1988).

Table 7.7 Best-fit values of the RRCs in each region, with temperature reported in K and eV. The wavelengths in the last column are simply the conversion of the threshold energy from keV to Å and are meant for convenience to the reader.

RRC	Region	Threshold energy (keV)	Temp. (10^4 K)	Temp. (eV)	Wavelength (Å)
Mg XII	Si	1.768 ± 0.001	$3.6^{+1.9}_{-1.3}$	$3.1^{+1.6}_{-1.1}$	7.022
Mg XI	Si	1.961 ± 0.002	$5.2^{+6.7}_{-2.9}$	$4.5^{+5.8}_{-2.5}$	6.321
Ne X	Mg	$1.3600^{+0.0012}_{-0.0010}$	$12.5^{+3.9}_{-2.9}$	$10.8^{+3.4}_{-2.5}$	9.116
Ne IX	Ne	$1.1950^{+0.0006}_{-0.0007}$	$5.2^{+3.9}_{-2.4}$	$4.5^{+3.4}_{-2.1}$	10.374
O VIII	Ne	0.8720 ± 0.0006	$1.0^{+4.8}_{-0.7}$	$0.9^{+4.2}_{-0.6}$	14.218

Table 7.8 Best-fit values of the G and R ratios of the He-like triplets and correspondent electron temperatures and densities (Porquet and Dubau, 2000). The electron density of the He-like Si XIII triplet (marked as *) is an upper limit.

Element	G	R	Temp. (K)	Temp. (eV)	Electron density n_e (cm^{-3})
S XV	$0.48^{+0.14}_{-0.10}$	$9.9^{+2.4}_{-2.2}$	—	—	
Si XIII	$0.80^{+0.10}_{-0.09}$	6.0 ± 0.6	1×10^7	860	1×10^{12} *
Mg XI	$0.74^{+0.13}_{-0.14}$	$1.2^{+0.3}_{-0.2}$	7×10^6	600	2×10^{13}
Ne IX	$3.7^{+4.4}_{-1.7}$	$1.2^{+0.6}_{-0.5}$	$1 - 3 \times 10^6$	90–260	1.5×10^{12}

Conclusions

This PhD thesis explored the role of low energy protons as a component of the non-X-ray background for X-ray missions with grazing incidence telescopes. Low energy protons, also known as ‘soft protons’, are pseudo-focused and funnelled by X-ray optics towards the focal plane when impacting on the mirrors at grazing incident angles. After crossing the filters, they reach the detectors, producing a signal difficult to disentangle from that of X-ray photons, so that when the soft proton flux is too high, observational data must be entirely discarded.

The issue represented by soft protons is crucial for the future ESA’s X-ray mission *Athena*. Amongst the goals of the mission, a primary role is reserved to faint sources at cosmological distances, which can be detected only if the particle background is low. Hence, a correct evaluation of the expected flux at the focal plane of the satellite is fundamental during the project and design phases of the mission.

The interaction of soft protons within X-ray satellites at grazing incidence can be thought as made of two successive steps: first with the optics and then with the instrumental focal plane. My PhD project mainly focused on the first step, with a modelling of old and new exper-

imental data of scattering of low-energy protons at grazing incidence from different X-ray mirror samples. The second step, i.e., the interaction of soft protons with the focal plane, was studied through a Geant4 simulation of *XMM-Newton* focal plane assembly. Hereafter, I will briefly recall the activities illustrated in this PhD thesis, highlighting the main results and conclusions, and the future improvements that *Athena* will bring to X-ray astronomy.

As said above, the first step to estimate the expected soft proton flux at the focal plane of any X-ray imaging satellite is understanding the interaction of soft protons with the optics. To this aim, I used a double approach: on one hand, I analysed and modeled old experimental measurements of scattering efficiency of protons at grazing incidence from *eROSITA* and *XMM-Newton* mirror samples; on the other hand, I performed new measurements of the scattering efficiency from an *Athena*'s Silicon Pore Optics (SPO) sample.

All the experimental scattering efficiencies can be modeled starting from the formula proposed by Remizovich et al. (1980) for charged particles at grazing incidence in non-elastic approximation. The Remizovich model relies on a physical parameter, σ , which encloses the micro-physics of the interaction of the impinging particle with the reflecting lattice. This parameter depends on the physical properties of the material and of the incident particle. However, the theoretical formulas proposed in literature to compute the value of σ do not lead to scattering efficiencies consistent with the experimentally ones. Hence, my approach consisted in directly fit the experimental data. The fit can be made only if energy losses are also taken into account, which

is why I used only the data from Diebold et al. (2015), where at each scattering efficiency corresponds an energy loss measurement.

In doing so, I obtained new values of the parameter σ , which resulted in a new semi-empirical analytical model able to reproduce the scattering efficiencies of all the experimental data sets.

New data were taken directly from a SPO sample during dedicated experimental campaigns, as part of the EXACRAD project. Two data sets were delivered, at two different incident energies, 172 ± 30 keV and 471 ± 25 keV, and at four different incident angles, 0.6° , 0.8° , 1.0° , and 1.2° . Each data set contains both on-axis and off-axis measurements.

A general comparison of the new data with the old *eROSITA* ones and with the semi-empirical model based on the Remizovich formula leads to the following conclusions:

- the scattering efficiencies show the trend expected from Remizovich et al. (1980). The on-axis data peak close to the specular reflection, while the off-axis data show peaks shifted to higher Ψ ; as expected, the off-axis data reach lower efficiencies than the on-axis ones; higher incident angles resulted in slightly higher scattering efficiencies;
- the scattering efficiency weakly depends on the energy of the incident beam;
- the semi-empirical model developed from *eROSITA* experimental data is able to acceptably reproduce the SPO low-energy data set, while it results in higher efficiencies for the high-energy data set.

Despite this positive result, it is necessary to develop a model specific for the SPO, with the σ derived from a direct fit of the data. This can be done by retrieving the energy losses from the raw experimental data.

The second step of the interaction of soft protons with the satellite takes place when the protons cross the eventual filters, reach the focal plane, and deposit their energy into the detectors. This part was studied by a simulation of the focal plane assembly of *XMM-Newton* with the Monte Carlo-based toolkit Geant4. The choice of *XMM-Newton* was not casual. It is well known, indeed, that the satellite experiences soft proton flares that strongly contaminate the observational data. Hence, *XMM-Newton* can provide actual data of soft protons, so that the results of the simulation can be compared with real scientific data. The tool that can make this comparison possible is a response matrix specific for protons. Therefore, the simulation represents also the first step to build a proton response matrix for *XMM-Newton*. If the entire procedure is successful, then a similar response matrix can be built for *Athena*. This activity is part of the 2-years AHEAD2020 project, started in the mid-2020.

The Geant4 simulation consisted in a simplified geometry of the focal plane assembly of *XMM-Newton*, but in a detailed reproduction of its filters and of the EPIC MOS camera. Protons with energy between 8 keV and 200 keV impact perpendicularly the medium filter. The transmission efficiency, computed as the probability that a proton crosses the filter and releases in the MOS camera an energy between 0.2 keV and 10 keV, i.e., in the MOS working range, shows two peaks due to the two different types of electrodes.

Finally, in the second part of this thesis, I presented observational data analysis of two different types of X-ray sources, to give a hint of the current limitations of X-ray astronomy and of the improvements that *Athena* could bring.

The first source is the radio millisecond pulsar M22A, for which I searched for counterparts in the γ -ray (*Fermi*/LAT), optical (HST), and X-ray (*Chandra*, *XMM-Newton*, and *Swift*/XRT) wavebands. The lack of any optical detection led to an upper limit on the mass of the companion star of $0.2 M_{\odot}$, consistent with the nature of black widow of this system, rather than redback. The X-ray spectrum, extracted from archival *Chandra* observations, is well modeled either with a hard power law, with a photon index of ~ 1.5 , or with a black-body model with a temperature of ~ 0.8 keV. However, the latter gives an unrealistic value of the effective polar cap radius, which makes the intrabinary shock scenario more likely than thermal emission from the neutron star surface.

Low levels of instrumental background, and especially of soft protons, for *Athena*/WFI will improve the detectability threshold (down to a nominal flux 10^{-17} erg s $^{-1}$), so that more faint and very-faint sources like M22A could be discovered, enhancing the knowledge we currently have of black widow and redback X-ray binary systems. However, a high level of soft proton flux can affect spectroscopic studies, especially at energies above 5 keV.

The second source is the wind-fed high-mass X-ray binary Vela X-1, for which I conducted a X-ray high-resolution spectroscopy study with the system at the orbital phase $\phi_{\text{orb}} \approx 0.75$, i.e., when the line of sight is intersecting the photoionisation wake that trails the neutron

star along the orbit. Through a blind search for spectral features with a Bayesian Blocks algorithm, I detected and identified emission lines from Fe, S, Si, Mg, Ne, and, to a lesser degree, from Al and Na, as well as five narrow radiative recombination continua from Mg XI-XII, Ne IX-X, O VIII, and He-like triplets of S, Si, Mg, and Ne.

Combining traditional plasma diagnostic techniques with simulations from more recent photoionisation models, as CLOUDY and PION in SPEX, I concluded that the plasma at this orbital phase is mainly photoionised, with the presence of at least another component. Indeed, the presence of a collisional component cannot be entirely excluded, as well as a mixture of ionised and collisional phases. This is in agreement with the idea of a clumpy wind, where colder and denser bubbles of matter are embedded in the hot, optically-thin photoionised wind accreting from the donor star into the compact object.

Athena will considerably enhance the detection and the resolution of spectral features, as showed by simulations with the instrument *Athena*/X-IFU. Thanks to higher energy resolutions, the cryogenic spectrometer X-IFU will resolve single lines in the Fe K α doublet and Fe XXV triplet and, thanks to the higher collecting area of the satellite, will allow plasma diagnostic for time scales as short as few hundreds of seconds.

References

Abdo, A. A., Ackermann, M., Ajello, M., Baldini, L., Ballet, J., Barbiellini, G., Bastieri, D., Bellazzini, R., Blandford, R. D., Bloom, E. D., Bonamente, E., Borgland, A. W., Bouvier, A., Brandt, T. J., Bregeon, J., Brigida, M., Bruel, P., Buehler, R., Buson, S., Caliandro, G. A., Cameron, R. A., Caraveo, P. A., Carrigan, S., Casandjian, J. M., Charles, E., Chaty, S., Chekhtman, A., Cheung, C. C., Chiang, J., Ciprini, S., Claus, R., Cohen-Tanugi, J., Conrad, J., Decesar, M. E., Dermer, C. D., de Palma, F., Digel, S. W., Silva, E. D. C. E., Drell, P. S., Dubois, R., Dumora, D., Favuzzi, C., Fortin, P., Frailis, M., Fukazawa, Y., Fusco, P., Gargano, F., Gasparrini, D., Gehrels, N., Germani, S., Giglietto, N., Giordano, F., Glanzman, T., Godfrey, G., Grenier, I., Grondin, M.-H., Grove, J. E., Guillemot, L., Guiriec, S., Hadasch, D., Harding, A. K., Hays, E., Jean, P., Jóhannesson, G., Johnson, T. J., Johnson, W. N., Kamae, T., Katagiri, H., Kataoka, J., Kerr, M., Knödlseeder, J., Kuss, M., Lande, J., Latronico, L., Lee, S.-H., Lemoine-Goumard, M., Llana Garde, M., Longo, F., Loparco, F., Lovellette, M. N., Lubrano, P., Makeev, A., Mazziotta, M. N., Michelson, P. F., Mitthumsiri, W., Mizuno, T., Monte, C., Monzani, M. E., Morselli, A., Moskalenko, I. V., Murgia, S., Naumann-Godo, M., Nolan, P. L., Norris, J. P., Nuss, E., Ohsugi, T., Omodei, N., Orlando, E., Ormes, J. F., Pancrazi, B., Parent, D., Pepe, M., Pescerollins, M., Piron, F., Porter, T. A., Rainò, S., Rando, R., Reimer, A., Reimer, O., Reposeur, T., Ripken, J., Romani, R. W., Roth, M., Sadrozinski, H. F.-W., Saz Parkinson, P. M., Sgrò, C., Siskind, E. J., Smith, D. A., Spinelli, P., Strickman, M. S., Suson, D. J., Takahashi, H., Takahashi, T., Tanaka, T., Thayer, J. B., Thayer, J. G., Tibaldo,

- L., Torres, D. F., Tosti, G., Tramacere, A., Uchiyama, Y., Usher, T. L., Vasileiou, V., Venter, C., Vilchez, N., Vitale, V., Waite, A. P., Wang, P., Webb, N., Winer, B. L., Yang, Z., Ylinen, T., Ziegler, M., and Fermi LAT Collaboration (2010). A population of gamma-ray emitting globular clusters seen with the Fermi Large Area Telescope. *Astronomy and Astrophysics*, 524:A75.
- Acero, F., Ackermann, M., Ajello, M., Albert, A., Atwood, W. B., Axelsson, M., Baldini, L., Ballet, J., Barbiellini, G., Bastieri, D., Belfiore, A., Bellazzini, R., Bissaldi, E., Blandford, R. D., Bloom, E. D., Bogart, J. R., Bonino, R., Bottacini, E., Bregeon, J., Britto, R. J., Bruel, P., Buehler, R., Burnett, T. H., Buson, S., Caliandro, G. A., Cameron, R. A., Caputo, R., Caragiulo, M., Caraveo, P. A., Casandjian, J. M., Cavazzuti, E., Charles, E., Chaves, R. C. G., Chekhtman, A., Cheung, C. C., Chiang, J., Chiaro, G., Ciprini, S., Claus, R., Cohen-Tanugi, J., Cominsky, L. R., Conrad, J., Cutini, S., D'Ammando, F., de Angelis, A., DeKlotz, M., de Palma, F., Desiante, R., Digel, S. W., Di Venere, L., Drell, P. S., Dubois, R., Dumora, D., Favuzzi, C., Fegan, S. J., Ferrara, E. C., Finke, J., Franckowiak, A., Fukazawa, Y., Funk, S., Fusco, P., Gargano, F., Gasparrini, D., Giebels, B., Giglietto, N., Giommi, P., Giordano, F., Giroletti, M., Glanzman, T., Godfrey, G., Grenier, I. A., Grondin, M.-H., Grove, J. E., Guillemot, L., Guiriec, S., Hadasch, D., Harding, A. K., Hays, E., Hewitt, J. W., Hill, A. B., Horan, D., Iafrate, G., Jogler, T., Jóhannesson, G., Johnson, R. P., Johnson, A. S., Johnson, T. J., Johnson, W. N., Kamae, T., Kataoka, J., Katsuta, J., Kuss, M., La Mura, G., Landriu, D., Larsson, S., Latronico, L., Lemoine-Goumard, M., Li, J., Li, L., Longo, F., Loparco, F., Lott, B., Lovellette, M. N., Lubrano, P., Madejski, G. M., Massaro, F., Mayer, M., Mazziotta, M. N., McEnery, J. E., Michelson, P. F., Mirabal, N., Mizuno, T., Moiseev, A. A., Mongelli, M., Monzani, M. E., Morselli, A., Moskalenko, I. V., Murgia, S., Nuss, E., Ohno, M., Ohsugi, T., Omodei, N., Orienti, M., Orlando, E., Ormes, J. F., Paneque, D., Panetta, J. H., Perkins, J. S., Pesce-Rollins, M., Piron, F., Pivato, G., Porter, T. A., Racusin, J. L., Rando, R., Razzano, M., Razzaque, S., Reimer, A., Reimer, O., Reposeur, T., Rochester, L. S., Romani, R. W., Salvetti, D., Sánchez-Conde, M., Saz Parkinson,

- P. M., Schulz, A., Siskind, E. J., Smith, D. A., Spada, F., Spandre, G., Spinelli, P., Stephens, T. E., Strong, A. W., Suson, D. J., Takahashi, H., Takahashi, T., Tanaka, Y., Thayer, J. G., Thayer, J. B., Thompson, D. J., Tibaldo, L., Tibolla, O., Torres, D. F., Torresi, E., Tosti, G., Troja, E., Van Klaveren, B., Vianello, G., Winer, B. L., Wood, K. S., Wood, M., Zimmer, S., and Fermi-LAT Collaboration (2015). Fermi Large Area Telescope Third Source Catalog. *Astrophysical Journal, Supplement*, 218:23.
- Agostinelli, S., Allison, J., Amako, K., Apostolakis, J., Araujo, H., Arce, P., Asai, M., Axen, D., Banerjee, S., Barrand, G., Behner, F., Bellagamba, L., Boudreau, J., Broglia, L., Brunengo, A., Burkhardt, H., Chauvie, S., Chuma, J., Chytracek, R., Cooperman, G., Cosmo, G., Degtyarenko, P., Dell'Acqua, A., Depaola, G., Dietrich, D., Enami, R., Feliciello, A., Ferguson, C., Fesefeldt, H., Folger, G., Foppiano, F., Forti, A., Garelli, S., Giani, S., Giannitrapani, R., Gibin, D., Gómez Cadenas, J. J., González, I., Gracia Abril, G., Greeniaus, G., Greiner, W., Grichine, V., Grossheim, A., Guatelli, S., Gumplinger, P., Hamatsu, R., Hashimoto, K., Hasui, H., Heikkinen, A., Howard, A., Ivanchenko, V., Johnson, A., Jones, F. W., Kallenbach, J., Kanaya, N., Kawabata, M., Kawabata, Y., Kawaguti, M., Kelner, S., Kent, P., Kimura, A., Kodama, T., Kokoulin, R., Kossov, M., Kurashige, H., Lamanna, E., Lampén, T., Lara, V., Lefebure, V., Lei, F., Liendl, M., Lockman, W., Longo, F., Magni, S., Maire, M., Medernach, E., Minamimoto, K., Mora de Freitas, P., Morita, Y., Murakami, K., Nagamatu, M., Nartallo, R., Nieminen, P., Nishimura, T., Ohtsubo, K., Okamura, M., O'Neale, S., Oohata, Y., Paech, K., Perl, J., Pfeiffer, A., Pia, M. G., Ranjard, F., Rybin, A., Sadilov, S., Di Salvo, E., Santin, G., Sasaki, T., Savvas, N., Sawada, Y., Scherer, S., Sei, S., Sirotenko, V., Smith, D., Starkov, N., Stoecker, H., Sulkimo, J., Takahata, M., Tanaka, S., Tcherniaev, E., Safai Tehrani, E., Tropeano, M., Truscott, P., Uno, H., Urban, L., Urban, P., Verderi, M., Walkden, A., Wander, W., Weber, H., Wellisch, J. P., Wenaus, T., Williams, D. C., Wright, D., Yamada, T., Yoshida, H., Zschesche, D., and G EANT4 Collaboration (2003). GEANT4 - A simulation toolkit. *Nuclear Instruments and Methods in Physics Research A*, 506:250–303.

- Allison, J., Amako, K., Apostolakis, J., Araujo, H., Dubois, P. A., Asai, M., Barrand, G., Capra, R., Chauvie, S., Chytracek, R., Cirrone, G. A. P., Cooperman, G., Cosmo, G., Cuttone, G., Daquino, G. G., Donszelmann, M., Dressel, M., Folger, G., Foppiano, F., Generowicz, J., Grichine, V., Guatelli, S., Gumplinger, P., Heikkinen, A., Hrivnacova, I., Howard, A., Incerti, S., Ivanchenko, V., Johnson, T., Jones, F., Koi, T., Kokoulin, R., Kossov, M., Kurashige, H., Lara, V., Larsson, S., Lei, F., Link, O., Longo, F., Maire, M., Mantero, A., Mascialino, B., McLaren, I., Lorenzo, P. M., Minamimoto, K., Murakami, K., Nieminen, P., Pandola, L., Parlati, S., Peralta, L., Perl, J., Pfeiffer, A., Pia, M. G., Ribon, A., Rodrigues, P., Russo, G., Sadilov, S., Santin, G., Sasaki, T., Smith, D., Starkov, N., Tanaka, S., Tcherniaev, E., Tome, B., Trindade, A., Truscott, P., Urban, L., Verderi, M., Walkden, A., Wellisch, J. P., Williams, D. C., Wright, D., and Yoshida, H. (2006). Geant4 developments and applications. *IEEE Transactions on Nuclear Science*, 53:270–278.
- Allison, J., Amako, K., Apostolakis, J., Arce, P., Asai, M., Aso, T., Bagli, E., Bagulya, A., Banerjee, S., Barrand, G., Beck, B. R., Bogdanov, A. G., Brandt, D., Brown, J. M. C., Burkhardt, H., Canal, P., Cano-Ott, D., Chauvie, S., Cho, K., Cirrone, G. A. P., Cooperman, G., Cortés-Giraldo, M. A., Cosmo, G., Cuttone, G., Depaola, G., Desorgher, L., Dong, X., Dotti, A., Elvira, V. D., Folger, G., Francis, Z., Galoyan, A., Garnier, L., Gayer, M., Genser, K. L., Grichine, V. M., Guatelli, S., Guèye, P., Gumplinger, P., Howard, A. S., Hřivnáčová, I., Hwang, S., Incerti, S., Ivanchenko, A., Ivanchenko, V. N., Jones, F. W., Jun, S. Y., Kaitaniemi, P., Karakatsanis, N., Karamitrosi, M., Kelsey, M., Kimura, A., Koi, T., Kurashige, H., Lechner, A., Lee, S. B., Longo, F., Maire, M., Mancusi, D., Mantero, A., Mendoza, E., Morgan, B., Murakami, K., Nikitina, T., Pandola, L., Paprocki, P., Perl, J., Petrović, I., Pia, M. G., Pokorski, W., Quesada, J. M., Raine, M., Reis, M. A., Ribon, A., Ristić Fira, A., Romano, F., Russo, G., Santin, G., Sasaki, T., Sawkey, D., Shin, J. I., Strakovsky, I. I., Taborda, A., Tanaka, S., Tomé, B., Toshito, T., Tran, H. N., Truscott, P. R., Urban, L., Uzhinsky, V., Verbeke, J. M., Verderi, M., Wendt, B. L., Wenzel, H., Wright, D. H., Wright, D. M., Yamashita, T., Yarba, J., and Yoshida, H. (2016). Recent developments

- in GEANT4. *Nuclear Instruments and Methods in Physics Research A*, 835:186–225.
- Alonso-García, J., Mateo, M., Sen, B., Banerjee, M., Catelan, M., Minniti, D., and von Braun, K. (2012). Uncloaking Globular Clusters in the Inner Galaxy. *Astronomical Journal*, 143:70.
- Alpar, M. A., Cheng, A. F., Ruderman, M. A., and Shaham, J. (1982). A new class of radio pulsars. *Nature*, 300:728–730.
- Amato, R., D’A1, A., Del Santo, M., de Martino, D., Marino, A., Di Salvo, T., Iaria, R., and Mineo, T. (2019). Search for multiwavelength emission from the binary millisecond pulsar PSR J1836-2354A in the globular cluster M22. *Monthly Notices of the RAS*, 486(3):3992–4000.
- Amato, R., Mineo, T., D’A1, A., Diebold, S., Fioretti, V., Guzman, A., Lotti, S., Macculi, C., Molendi, S., Perinati, E., Tenzer, C., and Santangelo, A. (2020). Soft proton scattering at grazing incidence from X-ray mirrors: analysis of experimental data in the framework of the non-elastic approximation. *Experimental Astronomy*, 49(3):115–140.
- Archibald, A. M., Stairs, I. H., Ransom, S. M., Kaspi, V. M., Kondratiev, V. I., Lorimer, D. R., McLaughlin, M. A., Boyles, J., Hessels, J. W. T., Lynch, R., van Leeuwen, J., Roberts, M. S. E., Jenet, F., Champion, D. J., Rosen, R., Barlow, B. N., Dunlap, B. H., and Remillard, R. A. (2009). A Radio Pulsar/X-ray Binary Link. *Science*, 324:1411.
- Arnaud, K. A. (1996). XSPEC: The First Ten Years. In Jacoby, G. H. and Barnes, J., editors, *Astronomical Data Analysis Software and Systems V*, volume 101 of *Astronomical Society of the Pacific Conference Series*, page 17.
- Arumugasamy, P., Pavlov, G. G., and Garmire, G. P. (2015). X-Ray Emission from J1446–4701, J1311–3430, and Other Black Widow Pulsars. *Astrophysical Journal*, 814:90.

- Baraffe, I., Homeier, D., Allard, F., and Chabrier, G. (2015). New evolutionary models for pre-main sequence and main sequence low-mass stars down to the hydrogen-burning limit. *Astronomy and Astrophysics*, 577:A42.
- Barret, D., den Herder, J. W., Piro, L., Ravera, L., Den Hartog, R., Macculi, C., Barcons, X., Page, M., Paltani, S., Rauw, G., Wilms, J., Ceballos, M., Duband, L., Gottardi, L., Lotti, S., de Plaa, J., Pointecouteau, E., Schmid, C., Akamatsu, H., Bagliani, D., Bandler, S., Barbera, M., Bastia, P., Biasotti, M., Branco, M., Camon, A., Cara, C., Cobo, B., Colasanti, L., Costa-Kramer, J. L., Corcione, L., Doriese, W., Duval, J. M., Fabrega, L., Gatti, F., de Gerone, M., Guttridge, P., Kelley, R., Kilbourne, C., van der Kuur, J., Mineo, T., Mitsuda, K., Natalucci, L., Ohashi, T., Peille, P., Perinati, E., Pigot, C., Pizzigoni, G., Pobes, C., Porter, F., Renotte, E., Sauvageot, J. L., Sciortino, S., Torrioli, G., Valenziano, L., Willingale, D., de Vries, C., and van Weers, H. (2013). The Hot and Energetic Universe: The X-ray Integral Field Unit (X-IFU) for Athena+. *arXiv e-prints*, page arXiv:1308.6784.
- Barret, D., Lam Trong, T., den Herder, J.-W., Piro, L., Cappi, M., Houvelin, J., Kelley, R., Mas-Hesse, J. M., Mitsuda, K., Paltani, S., Rauw, G., Rozanska, A., Wilms, J., Bandler, S., Barbera, M., Barcons, X., Bozzo, E., Ceballos, M. T., Charles, I., Costantini, E., Decourchelle, A., den Hartog, R., Duband, L., Duval, J.-M., Fiore, F., Gatti, F., Goldwurm, A., Jackson, B., Jonker, P., Kilbourne, C., Macculi, C., Mendez, M., Molendi, S., Orleanski, P., Pajot, F., Pointecouteau, E., Porter, F., Pratt, G. W., Prêle, D., Ravera, L., Sato, K., Schaye, J., Shinozaki, K., Thibert, T., Valenziano, L., Valette, V., Vink, J., Webb, N., Wise, M., Yamasaki, N., Douchin, F., Mesnager, J.-M., Pontet, B., Pradines, A., Branduardi-Raymont, G., Bulbul, E., Dadina, M., Etori, S., Finoguenov, A., Fukazawa, Y., Janiuk, A., Kaastra, J., Mazzotta, P., Miller, J., Miniutti, G., Naze, Y., Nicastro, F., Scioritino, S., Simonescu, A., Torrejon, J. M., Frezouls, B., Geoffray, H., Peille, P., Aicardi, C., André, J., Daniel, C., Clénet, A., Etcheverry, C., Gloaguen, E., Hervet, G., Jolly, A., Ledot, A., Paillet, I., Schmisser, R., Vella, B., Damery, J.-C., Boyce,

- K., Dipirro, M., Lotti, S., Schwander, D., Smith, S., Van Leeuwen, B.-J., van Weers, H., Clerc, N., Cobo, B., Dauser, T., Kirsch, C., Cucchetti, E., Eckart, M., Ferrando, P., and Natalucci, L. (2018). The ATHENA X-ray Integral Field Unit (X-IFU). In *Proceedings of the SPIE*, volume 10699 of *Society of Photo-Optical Instrumentation Engineers (SPIE) Conference Series*, page 106991G.
- Bassa, C. G., Patruno, A., Hessels, J. W. T., Keane, E. F., Monard, B., Mahony, E. K., Bogdanov, S., Corbel, S., Edwards, P. G., Archibald, A. M., Janssen, G. H., Stappers, B. W., and Tendulkar, S. (2014). A state change in the low-mass X-ray binary XSS J12270-4859. *Monthly Notices of the RAS*, 441:1825–1830.
- Bearden, J. A. and Burr, A. F. (1967). Reevaluation of X-Ray Atomic Energy Levels. *Reviews of Modern Physics*, 39(1):125–142.
- Becker, W. and Trümper, J. (1999). The X-ray emission properties of millisecond pulsars. *Astronomy and Astrophysics*, 341:803–817.
- Bhattacharya, D. and van den Heuvel, E. P. J. (1991a). Formation and evolution of binary and millisecond radio pulsars. *Physics Reports*, 203(1-2):1–124.
- Bhattacharya, D. and van den Heuvel, E. P. J. (1991b). Formation and evolution of binary and millisecond radio pulsars. *Physics Reports*, 203:1–124.
- Bhattacharya, S., Heinke, C. O., Chugunov, A. I., Freire, P. C. C., Ridolfi, A., and Bogdanov, S. (2017). Chandra studies of the globular cluster 47 Tucanae: A deeper X-ray source catalogue, five new X-ray counterparts to millisecond radio pulsars, and new constraints to r-mode instability window. *Monthly Notices of the RAS*, 472:3706–3721.
- Bianchi, S., Miniutti, G., Fabian, A. C., and Iwasawa, K. (2005). The XMM-Newton view of Mrk 3 and IXO 30. *Monthly Notices of the RAS*, 360(1):380–389.

- Blondin, J. M., Kallman, T. R., Fryxell, B. A., and Taam, R. E. (1990). Hydrodynamic Simulations of Stellar Wind Disruption by a Compact X-Ray Source. *Astrophysical Journal*, 356:591.
- Blumenthal, G. R., Drake, G. W. F., and Tucker, W. H. (1972). Ratio of Line Intensities in Helium-Like Ions as a Density Indicator. *Astrophysical Journal*, 172:205.
- Bogdanov, S. (2018). X-rays from Radio Millisecond Pulsars. In Weltevrede, P., Perera, B. B. P., Preston, L. L., and Sanidas, S., editors, *Pulsar Astrophysics the Next Fifty Years*, volume 337, pages 116–119.
- Bogdanov, S., Grindlay, J. E., Heinke, C. O., Camilo, F., Freire, P. C. C., and Becker, W. (2006). Chandra X-Ray Observations of 19 Millisecond Pulsars in the Globular Cluster 47 Tucanae. *Astrophysical Journal*, 646:1104–1115.
- Bogdanov, S., Grindlay, J. E., and van den Berg, M. (2005). An X-Ray Variable Millisecond Pulsar in the Globular Cluster 47 Tucanae: Closing the Link to Low-Mass X-Ray Binaries. *Astrophysical Journal*, 630:1029–1036.
- Brown, G. V., Beiersdorfer, P., Liedahl, D. A., Widmann, K., and Kahn, S. M. (1998). Laboratory Measurements and Modeling of the Fe XVII X-Ray Spectrum. *Astrophysical Journal*, 502(2):1015–1026.
- Burderi, L., Possenti, A., D’Antona, F., Di Salvo, T., Burgay, M., Stella, L., Menna, M. T., Iaria, R., Campana, S., and d’Amico, N. (2001). Where May Ultrafast Rotating Neutron Stars Be Hidden? *Astrophysical Journal, Letters*, 560:L71–L74.
- Burrows, D. N., Hill, J. E., Nousek, J. A., Kennea, J. A., Wells, A., and Osborne (2005). The Swift X-Ray Telescope. *Space Science Reviews*, 120:165–195.
- Canizares, C. R., Davis, J. E., Dewey, D., Flanagan, K. A., Galton, E. B., Huenemoerder, D. P., Ishibashi, K., Markert, T. H., Marshall, H. L., McGuirk, M., Schattenburg, M. L., Schulz, N. S., Smith,

- H. I., and Wise, M. (2005). The Chandra High-Energy Transmission Grating: Design, Fabrication, Ground Calibration, and 5 Years in Flight. *Publications of the ASP*, 117(836):1144–1171.
- Caraveo, P. A. (2014). Gamma-Ray Pulsar Revolution. *Annual Review of Astron. and Astrophys.*, 52:211–250.
- Cash, W. (1979). Parameter estimation in astronomy through application of the likelihood ratio. *Astrophysical Journal*, 228:939–947.
- Chabrier, G., Baraffe, I., Allard, F., and Hauschildt, P. (2000). Evolutionary Models for Very Low-Mass Stars and Brown Dwarfs with Dusty Atmospheres. *Astrophysical Journal*, 542:464–472.
- Chaty, S., Fortin, F., García, F., and Fogantini, F. (2019). The dark side of supergiant High-Mass X-ray Binaries. *arXiv e-prints*, page arXiv:1901.03593.
- Chen, K. (1991). Gamma-ray emission from millisecond pulsars in globular clusters. *Nature*, 352:695–697.
- Cheng, Z., Li, Z., Xu, X., and Li, X. (2018). A Chandra Survey of Milky Way Globular Clusters. I. Emissivity and Abundance of Weak X-Ray Sources. *Astrophysical Journal*, 858:33.
- Conti, G., Mattaini, E., Santambrogio, E., Sacco, B., Cusumano, G., Citterio, O., Braeuninger, H. W., and Burkert, W. (1994). X-ray characteristics of the Italian X-Ray Astronomy Satellite (SAX) flight mirror units. In Hoover, R. B. and Walker, A. B., editors, *Advances in Multilayer and Grazing Incidence X-Ray/EUV/FUV Optics*, volume 2279 of *Society of Photo-Optical Instrumentation Engineers (SPIE) Conference Series*, pages 101–109.
- Corbel, S. (2011). Microquasars: an observational review. In Romero, G. E., Sunyaev, R. A., and Belloni, T., editors, *Jets at All Scales*, volume 275 of *IAU Symposium*, pages 205–214.
- Cusumano, G., Campana, S., Romano, P., Mangano, V., Moretti, A., Abbey, A. F., Angelini, L., Beardmore, A. P., Burrows, D. N., Capalbi, M., Chincarini, G., Citterio, O., Giommi, P., Goad, M. R.,

- Godet, O., Hartner, G. D., Hill, J. E., Kennea, J. A., La Parola, V., Mineo, T., Morris, D., Nousek, J. A., Osborne, J. P., Page, K., Pagani, C., Perri, M., Tagliaferri, G., Tamburelli, F., and Wells, A. (2006). In-flight calibration of the Swift XRT effective area. In Holt, S. S., Gehrels, N., and Nousek, J. A., editors, *Gamma-Ray Bursts in the Swift Era*, volume 836 of *American Institute of Physics Conference Series*, pages 664–667.
- Davidson, K. and Ostriker, J. P. (1973). Neutron-Star Accretion in a Stellar Wind: Model for a Pulsed X-Ray Source. *Astrophysical Journal*, 179:585–598.
- de Martino, D., Papitto, A., Belloni, T., Burgay, M., De Ona Wilhelmi, E., Li, J., Pellizzoni, A., Possenti, A., Rea, N., and Torres, D. F. (2015). Multiwavelength observations of the transitional millisecond pulsar binary XSS J12270-4859. *Monthly Notices of the RAS*, 454:2190–2198.
- Diebold, S., Hanschke, S., Perinati, E., Smith, R., Tenzer, C., Santangelo, A., and Jochum, J. (2017). Updates on experimental grazing angle soft proton scattering. In *Society of Photo-Optical Instrumentation Engineers (SPIE) Conference Series*, volume 10397 of *Society of Photo-Optical Instrumentation Engineers (SPIE) Conference Series*, page 103970W.
- Diebold, S., Tenzer, C., Perinati, E., Santangelo, A., Freyberg, M., Friedrich, P., and Jochum, J. (2015). Soft proton scattering efficiency measurements on x-ray mirror shells. *Experimental Astronomy*, 39:343–365.
- Doroshenko, V., Santangelo, A., Nakahira, S., Mihara, T., Sugizaki, M., Matsuoka, M., Nakajima, M., and Makishima, K. (2013). Footprints in the wind of Vela X-1 traced with MAXI. *Astronomy and Astrophysics*, 554:A37.
- Drake, G. W. (1988). Theoretical energies for the $n = 1$ and 2 states of the helium isoelectronic sequence up to $Z = 100$. *Canadian Journal of Physics*, 66:586.

- Eggleton, P. P. (1983). Approximations to the radii of Roche lobes. *Astrophysical Journal*, 268:368.
- El Mellah, I., Sander, A. A. C., Sundqvist, J. O., and Keppens, R. (2019). Formation of wind-captured disks in supergiant X-ray binaries. Consequences for Vela X-1 and Cygnus X-1. *Astronomy and Astrophysics*, 622:A189.
- El Mellah, I., Sundqvist, J. O., and Keppens, R. (2018). Accretion from a clumpy massive-star wind in supergiant X-ray binaries. *Monthly Notices of the RAS*, 475(3):3240–3252.
- Erickson, G. W. (1977). Energy levels of one-electron atoms. *Journal of Physical and Chemical Reference Data*, 6(3):831–870.
- Fabian, A. C., Pringle, J. E., and Rees, M. J. (1975). Tidal capture formation of binary systems and X-ray sources in globular clusters. *Monthly Notices of the RAS*, 172:15p–18p.
- Ferland, G. J., Chatzikos, M., Guzmán, F., Lykins, M. L., van Hoof, P. A. M., Williams, R. J. R., Abel, N. P., Badnell, N. R., Keenan, F. P., Porter, R. L., and Stancil, P. C. (2017). The 2017 Release Cloudy. *Revista Mexicana de Astronomía y Astrofísica*, 53:385–438.
- Firsov, O. B. (1958). Scattering of ions by atoms. *JEPT*, 34:447–452.
- Firsov, O. B. (1972). Motion of High Energy Particles in a Medium in the Diffusion Approximation in Velocity Space. *Soviet Journal of Experimental and Theoretical Physics*, 34:773.
- Forbes, D. A. and Bridges, T. (2010). Accreted versus in situ Milky Way globular clusters. *Monthly Notices of the RAS*, 404:1203–1214.
- Forestell, L. M., Heinke, C. O., Cohn, H. N., Lugger, P. M., Sivakoff, G. R., Bogdanov, S., Cool, A. M., and Anderson, J. (2014). A Chandra look at the X-ray faint millisecond pulsars in the globular cluster NGC 6752. *Monthly Notices of the RAS*, 441:757–768.

- Forman, W., Jones, C., Tananbaum, H., Gursky, H., Kellogg, E., and Giacconi, R. (1973). UHURU Observations of the Binary X-Ray Source 2u 0900-40. *Astrophysical Journal*, 182:L103.
- Foster, A. R., Ji, L., Smith, R. K., and Brickhouse, N. S. (2012). Updated Atomic Data and Calculations for X-Ray Spectroscopy. *Astrophysical Journal*, 756(2):128.
- Foster, A. R., Smith, R. K., and Brickhouse, N. S. (2017). Data for non equilibrium modeling with AtomDB. In *Atomic Processes in Plasmas (APiP 2016)*, volume 1811 of *American Institute of Physics Conference Series*, page 190005.
- Fraser, G. W., Read, A. M., Sembay, S., Carter, J. A., and Schyns, E. (2014). Potential solar axion signatures in X-ray observations with the XMM-Newton observatory. *Monthly Notices of the RAS*, 445(2):2146–2168.
- Friedrich, P., Bräuninger, H., Budau, B., Burkert, W., Eder, J., Freyberg, M. J., Hartner, G., Mühlegger, M., Predehl, P., Erhard, M., Gutruf, S., Jugler, D., Kampf, D., Borghi, G., Citterio, O., Rossi, M., Valsecchi, G., Vernani, D., and Zimmermann, M. (2008). Design and development of the eROSITA x-ray mirrors. In *Proceedings of the SPIE*, volume 7011 of *Society of Photo-Optical Instrumentation Engineers (SPIE) Conference Series*, page 70112T.
- Fürst, F., Kreykenbohm, I., Pottschmidt, K., Wilms, J., Hanke, M., Rothschild, R. E., Kretschmar, P., Schulz, N. S., Huenemoerder, D. P., Klochkov, D., and Staubert, R. (2010). X-ray variation statistics and wind clumping in Vela X-1. *Astronomy and Astrophysics*, 519:A37.
- Fürst, F., Pottschmidt, K., Wilms, J., Tomsick, J. A., Bachetti, M., Boggs, S. E., Christensen, F. E., Craig, W. W., Grefenstette, B. W., Hailey, C. J., Harrison, F., Madsen, K. K., Miller, J. M., Stern, D., Walton, D. J., and Zhang, W. (2014). NuSTAR Discovery of a Luminosity Dependent Cyclotron Line Energy in Vela X-1. *Astrophysical Journal*, 780(2):133.

- Gabriel, A. H. (1972). Dielectronic satellite spectra for highly-charged helium-like ionlines. *Monthly Notices of the RAS*, 160:99.
- Gabriel, A. H. and Jordan, C. (1969). Interpretation of solar helium-like ion line intensities. *Monthly Notices of the RAS*, 145:241.
- Garcia, J. D. and Mack, J. E. (1965). Energy Level and Line Tables for One-Electron Atomic Spectra. *Journal of the Optical Society of America (1917-1983)*, 55(6):654.
- Gastaldello, F., Ghizzardi, S., Marelli, M., Salvetti, D., Molendi, S., De Luca, A., Moretti, A., Rossetti, M., and Tiengo, A. (2017). A systematic analysis of the XMM-Newton background: IV. Origin of the unfocused and focused components. *Experimental Astronomy*, 44:321–336.
- Gehrels, N., Chincarini, G., Giommi, P., Mason, K. O., Nousek, J. A., Wells, A. A., and White, N. E. (2004). The Swift Gamma-Ray Burst Mission. *Astrophysical Journal*, 611:1005–1020.
- Geller, A. M., Leiner, E. M., Bellini, A., Gleisinger, R., Haggard, D., Kamann, S., Leigh, N. W. C., Mathieu, R. D., Sills, A., Watkins, L. L., and Zurek, D. (2017). On the Origin of Sub-subgiant Stars. I. Demographics. *Astrophysical Journal*, 840:66.
- Gentile, P. A., Roberts, M. S. E., McLaughlin, M. A., Camilo, F., Hessels, J. W. T., Kerr, M., Ransom, S. M., Ray, P. S., and Stairs, I. H. (2014). X-Ray Observations of Black Widow Pulsars. *Astrophysical Journal*, 783:69.
- Ghizzardi, S., Marelli, M., Salvetti, D., Gastaldello, F., Molendi, S., De Luca, A., Moretti, A., Rossetti, M., and Tiengo, A. (2017). A systematic analysis of the XMM-Newton background: III. Impact of the magnetospheric environment. *Experimental Astronomy*, 44:273–285.
- Giacconi, R., Gursky, H., Kellogg, E., Schreier, E., and Tananbaum, H. (1971). Discovery of Periodic X-Ray Pulsations in Centaurus X-3 from UHURU. *Astrophysical Journal, Letters*, 167:L67.

- Giménez-García, A., Shenar, T., Torrejón, J. M., Oskinova, L., Martínez-Núñez, S., Hamann, W. R., Rodes-Roca, J. J., González-Galán, A., Alonso-Santiago, J., González-Fernández, C., Bernabeu, G., and Sander, A. (2016). Measuring the stellar wind parameters in IGR J17544-2619 and Vela X-1 constrains the accretion physics in supergiant fast X-ray transient and classical supergiant X-ray binaries. , 591:A26.
- Goldstein, G., Huenemoerder, D. P., and Blank, D. (2004). Variation in Emission and Absorption Lines and Continuum Flux by Orbital Phase in Vela X-1. *Astronomical Journal*, 127(4):2310–2321.
- Grinberg, V., Hell, N., El Mellah, I., Neilsen, J., Sander, A. A. C., Leutenegger, M., Fürst, F., Huenemoerder, D. P., Kretschmar, P., Kühnel, M., Martínez-Núñez, S., Niu, S., Pottschmidt, K., Schulz, N. S., Wilms, J., and Nowak, M. A. (2017). The clumpy absorber in the high-mass X-ray binary Vela X-1. *Astronomy and Astrophysics*, 608:A143.
- Guainazzi, M. and Tashiro, M. S. (2018). The Hot Universe with XRISM and Athena. *arXiv e-prints*, page arXiv:1807.06903.
- Haberl, F. and White, N. E. (1990). The X-Ray Absorption Spectrum of VELA X-1. *Astrophysical Journal*, 361:225.
- Harding, A. K., Usov, V. V., and Muslimov, A. G. (2005). High-Energy Emission from Millisecond Pulsars. *Astrophysical Journal*, 622:531–543.
- Harris, W. E. (1996). A Catalog of Parameters for Globular Clusters in the Milky Way. *Astronomical Journal*, 112:1487.
- Harrison, F. A., Craig, W. W., Christensen, F. E., Hailey, C. J., Zhang, W. W., Boggs, S. E., Stern, D., Cook, W. R., Forster, K., Giommi, P., Grefenstette, B. W., Kim, Y., Kitaguchi, T., Koglin, J. E., Madson, K. K., Mao, P. H., Miyasaka, H., Mori, K., Perri, M., Pivovarov, M. J., Puccetti, S., Rana, V. R., Westergaard, N. J., Willis, J., Zoglauer, A., An, H., Bachetti, M., Barrière, N. M., Bellm, E. C.,

- Bhalerao, V., Brejnholt, N. F., Fuerst, F., Liebe, C. C., Markwardt, C. B., Nynka, M., Vogel, J. K., Walton, D. J., Wik, D. R., Alexander, D. M., Cominsky, L. R., Hornschemeier, A. E., Hornstrup, A., Kaspi, V. M., Madejski, G. M., Matt, G., Molendi, S., Smith, D. M., Tomsick, J. A., Ajello, M., Ballantyne, D. R., Baloković, M., Barret, D., Bauer, F. E., Blandford, R. D., Brandt, W. N., Brennerman, L. W., Chiang, J., Chakrabarty, D., Chenevez, J., Comastri, A., Dufour, F., Elvis, M., Fabian, A. C., Farrah, D., Fryer, C. L., Gotthelf, E. V., Grindlay, J. E., Helfand, D. J., Krivonos, R., Meier, D. L., Miller, J. M., Natalucci, L., Ogle, P., Ofek, E. O., Ptak, A., Reynolds, S. P., Rigby, J. R., Tagliaferri, G., Thorsett, S. E., Treister, E., and Urry, C. M. (2013). The Nuclear Spectroscopic Telescope Array (NuSTAR) High-energy X-Ray Mission. *Astrophysical Journal*, 770(2):103.
- Heinke, C. O. (2010). X-ray Sources in Galactic Globular Clusters. In Kalogera, V. and van der Sluys, M., editors, *American Institute of Physics Conference Series*, volume 1314 of *American Institute of Physics Conference Series*, pages 135–142.
- Heinke, C. O., Rybicki, G. B., Narayan, R., and Grindlay, J. E. (2006). A Hydrogen Atmosphere Spectral Model Applied to the Neutron Star X7 in the Globular Cluster 47 Tucanae. *Astrophysical Journal*, 644:1090–1103.
- Hell, N., Brown, G. V., Wilms, J., Grinberg, V., Clementson, J., Liedahl, D., Porter, F. S., Kelley, R. L., Kilbourne, C. A., and Beiersdorfer, P. (2016). Laboratory Measurements of the K-shell Transition Energies in L- shell Ions of SI and S. *Astrophysical Journal*, 830(1):26.
- Hertz, P. and Grindlay, J. E. (1983). An X-ray survey of globular clusters and their X-ray luminosity function. *Astrophysical Journal*, 275:105–119.
- HI4PI Collaboration, Ben Bekhti, N., Flöer, L., Keller, R., Kerp, J., Lenz, D., Winkel, B., Bailin, J., Calabretta, M. R., Dedes, L., Ford, H. A., Gibson, B. K., Haud, U., Janowiecki, S., Kalberla, P. M. W., Lockman, F. J., McClure-Griffiths, N. M., Murphy, T., Nakanishi,

- H., Pisano, D. J., and Staveley-Smith, L. (2016). HI4PI: A full-sky HI survey based on EBHIS and GASS. *Astronomy and Astrophysics*, 594:A116.
- Hills, J. G. (1976). The formation of binaries containing black holes by the exchange of companions and the X-ray sources in globular clusters. *Monthly Notices of the RAS*, 175:1P–4P.
- Hiltner, W. A., Werner, J., and Osmer, P. (1972). Binary Nature of the B Supergiant in the Error Box of the VELA X-Ray Source. *Astrophysical Journal, Letters*, 175:L19.
- Hiraga, J., Tsunemi, H., Short, A. D., Abbey, A. F., Bennie, P. J., and Turner, M. J. L. (2001). Direct measurement of sub-pixel structure of the EPIC MOS CCD on-board the XMM//NEWTON satellite. *Nuclear Instruments and Methods in Physics Research A*, 465(2-3):384–393.
- Hirsch, M., Hell, N., Grinberg, V., Ballhausen, R., Nowak, M. A., Pottschmidt, K., Schulz, N. S., Dauser, T., Hanke, M., Kallman, T. R., Brown, G. V., and Wilms, J. (2019). Chandra X-ray spectroscopy of the focused wind in the Cygnus X-1 system. III. Dipping in the low/hard state. *Astronomy and Astrophysics*, 626:A64.
- Jansen, F., Lumb, D., Altieri, B., Clavel, J., Ehle, M., Erd, C., Gabriel, C., Guainazzi, M., Gondoin, P., Much, R., Munoz, R., Santos, M., Schartel, N., Texier, D., and Vacanti, G. (2001). XMM-Newton observatory. I. The spacecraft and operations. *Astronomy and Astrophysics*, 365:L1–L6.
- Johnston, H. M., Verbunt, F., and Hasinger, G. (1994). ROSAT PSPC observations of globular clusters. *Astronomy and Astrophysics*, 289:763–774.
- Joss, P. C. and Rappaport, S. A. (1984). Neutron Stars in Interacting Binary Systems. *Annual Review of Astron. and Astrophys.*, 22:537–592.

- Kaastra, J. S. and Mewe, R. (1993). X-ray emission from thin plasmas. I - Multiple Auger ionisation and fluorescence processes for Be to Zn. *Astronomy and Astrophysics, Supplement*, 97(2):443–482.
- Kaastra, J. S., Mewe, R., and Nieuwenhuijzen, H. (1996). SPEX: a new code for spectral analysis of X UV spectra. In Yamashita, K. and Watanabe, T., editors, *UV and X-ray Spectroscopy of Astrophysical and Laboratory Plasmas*, pages 411–414.
- Kaastra, J. S., Raassen, A. J. J., de Plaa, J., and Gu, L. (2018). Spex x-ray spectral fitting package. Zenodo. 10.5281/zenodo.2419563.
- Kaper, L., Hammerschlag-Hensberge, G., and Zuiderwijk, E. J. (1994). Spectroscopic evidence for photo-ionization wakes in VELA X-1 and 4U 1700–37. *Astronomy and Astrophysics*, 289:846–854.
- Kelley, R. L., Akamatsu, H., Azzarello, P., Bialas, T., Boyce, K. R., Brown, G. V., Canavan, E., Chiao, M. P., Costantini, E., DiPirro, M. J., Eckart, M. E., Ezoë, Y., Fujimoto, R., Haas, D., den Herder, J.-W., Hoshino, A., Ishikawa, K., Ishisaki, Y., Iyomoto, N., Kilbourne, C. A., Kimball, M. O., Kitamoto, S., Konami, S., Koyama, S., Leutenegger, M. A., McCammon, D., Mitsuda, K., Mitsuishi, I., Moseley, H., Murakami, H., Murakami, M., Noda, H., Ogawa, M., Ohashi, T., Okamoto, A., Ota, N., Paltani, S., Porter, F. S., Sakai, K., Sato, K., Sato, Y., Sawada, M., Seta, H., Shinozaki, K., Shirron, P. J., Sneiderman, G. A., Sugita, H., Szymkowiak, A. E., Takei, Y., Tamagawa, T., Tashiro, M., Terada, Y., Tsujimoto, M., de Vries, C. P., Yamada, S., Yamasaki, N. Y., and Yatsu, Y. (2016). *The Astro-H high resolution soft x-ray spectrometer*, volume 9905 of *Society of Photo-Optical Instrumentation Engineers (SPIE) Conference Series*, page 99050V.
- Kelly, R. L. (1987). Atomic and ionic spectrum lines below 2000 Angstroms. Hydrogen through Krypton. *Journal of Physical and Chemical Reference Data*, 17.
- King, A. R. (1988). The evolution of compact binaries. *Quarterly Journal of the RAS*, 29:1–25.

- Kinkhabwala, A., Sako, M., Behar, E., Kahn, S. M., Paerels, F., Brinkman, A. C., Kaastra, J. S., Gu, M. F., and Liedahl, D. A. (2002). XMM-Newton Reflection Grating Spectrometer Observations of Discrete Soft X-Ray Emission Features from NGC 1068. *Astrophysical Journal*, 575(2):732–746.
- Kretschmar, P., Fürst, F., Sidoli, L., Bozzo, E., Alfonso-Garzón, J., Bodaghee, A., Chaty, S., Chernyakova, M., Ferrigno, C., Manousakis, A., Negueruela, I., Postnov, K., Paizis, A., Reig, P., Rodes-Roca, J. J., Tsygankov, S., Bird, A. J., Bissinger né Kühnel, M., Blay, P., Caballero, I., Coe, M. J., Domingo, A., Doroshenko, V., Ducci, L., Falanga, M., Grebenev, S. A., Grinberg, V., Hemphill, P., Kreykenbohm, I., Kreykenbohm né Fritz, S., Li, J., Lutovinov, A. e. A., Martínez-Núñez, S., Mas-Hesse, J. M., Masetti, N., McBride, V. A., Neronov, A., Pottschmidt, K., Rodriguez, J., Romano, P., Rothschild, R. E., Santangelo, A., Sguera, V., Staubert, R., Tomsick, J. A., Torrejón, J. M., Torres, D. F., Walter, R., Wilms, J., Wilson-Hodge, C. A., and Zhang, S. (2019). Advances in Understanding High-Mass X-ray Binaries with INTEGRAL and Future Directions. *New Astronomy Review*, 86:101546.
- Kreykenbohm, I., Wilms, J., Kretschmar, P., Torrejón, J. M., Pottschmidt, K., Hanke, M., Santangelo, A., Ferrigno, C., and Staubert, R. (2008). High variability in Vela X-1: giant flares and off states. *Astronomy and Astrophysics*, 492(2):511–525.
- Lamb, F. K., Pethick, C. J., and Pines, D. (1973). A Model for Compact X-Ray Sources: Accretion by Rotating Magnetic Stars. *Astrophysical Journal*, 184:271–290.
- Liao, Z., Liu, J., Zheng, X., and Gou, L. (2020). Spectral evidence of an accretion disc in wind-fed X-ray pulsar Vela X-1 during an unusual spin-up period. *Monthly Notices of the RAS*, 492(4):5922–5929.
- Linares, M. (2014). X-Ray States of Redback Millisecond Pulsars. *Astrophysical Journal*, 795:72.
- Lodders, K., Palme, H., and Gail, H. P. (2009). Abundances of the Elements in the Solar System. *Landolt Börnrstein*, 4B:712.

- Lomaeva, M., Grinberg, V., Guainazzi, M., Hell, N., Bianchi, S., Kühnel, M. B. n., Fürst, F., Kretschmar, P., Martínez-Chicharro, M., Martínez-Núñez, S., and Torrejón, J. M. (2020). High-resolution X-ray spectroscopy of the stellar wind in Vela X-1 during a flare. *arXiv e-prints*, page arXiv:2007.07260.
- Longair, M. S. (2011). *High Energy Astrophysics*.
- Lorimer, D. R. and Kramer, M. (2004). *Handbook of Pulsar Astronomy*.
- Lotti, S., Mineo, T., Jacquy, C., Laurenza, M., Fioretti, V., Minervini, G., Santin, G., Molendi, S., Alberti, T., Dondero, P., Mantero, A., Ivanchenko, V., Macculi, C., and Piro, L. (2018). Soft proton flux on ATHENA focal plane and its impact on the magnetic diverter design. *Experimental Astronomy*, 45(3):411–428.
- Lotti, S., Mineo, T., Jacquy, C., Molendi, S., D’Andrea, M., Macculi, C., and Piro, L. (2017). The particle background of the X-IFU instrument. *Experimental Astronomy*, 44:371–385.
- Lynch, R. S., Ransom, S. M., Freire, P. C. C., and Stairs, I. H. (2011). Six New Recycled Globular Cluster Pulsars Discovered with the Green Bank Telescope. *Astrophysical Journal*, 734:89.
- Macculi, C., Argan, A., Brienza, D., D’Andrea, M., Lotti, S., Minervini, G., Piro, L., Biasotti, M., Ferrari Barusso, L., Gatti, F., Rigano, M., Torrioli, G., Fiorini, M., Molendi, S., Uslenghi, M., Cavazzuti, E., and Volpe, A. (2020). The Cryogenic AntiCoincidence Detector for ATHENA X-IFU: The Project Status. *Journal of Low Temperature Physics*, 199(1-2):416–424.
- Malacaria, C., Mihara, T., Santangelo, A., Makishima, K., Matsuoka, M., Morii, M., and Sugizaki, M. (2016). Probing the stellar wind environment of Vela X-1 with MAXI. *Astronomy and Astrophysics*, 588:A100.
- Manchester, R. N. and Taylor, J. H. (1977). *Pulsars*.
- Manousakis, A. (2011). *Accretion in High Mass X-ray Binaries*. Dissertation, Université de Genève.

- Manousakis, A. and Walter, R. (2015). Origin of the X-ray off-states in Vela X-1. *Astronomy and Astrophysics*, 575:A58.
- Marelli, M., Salvetti, D., Gastaldello, F., Ghizzardi, S., Molendi, S., Luca, A. D., Moretti, A., Rossetti, M., and Tiengo, A. (2017). A systematic analysis of the XMM-Newton background: I. Dataset and extraction procedures. *Experimental Astronomy*, 44:297–308.
- Martínez-Núñez, S., Torrejón, J. M., Kühnel, M., Kretschmar, P., Stuhlinger, M., Rodes-Roca, J. J., Fürst, F., Kreykenbohm, I., Martín-Carrillo, A., Pollock, A. M. T., and Wilms, J. (2014). The accretion environment in Vela X-1 during a flaring period using XMM-Newton. *Astronomy and Astrophysics*, 563:A70.
- Mashkova, E. and Molchanov, V. (1985). *Medium-Energy Ion Reflection from Solids*. Modern Problems in Condensed Matter Sciences. Elsevier Science.
- Matsuoka, M., Kawasaki, K., Ueno, S., Tomida, H., Kohama, M., Suzuki, M., Adachi, Y., Ishikawa, M., Mihara, T., Sugizaki, M., Isobe, N., Nakagawa, Y., Tsunemi, H., Miyata, E., Kawai, N., Kataoka, J., Morii, M., Yoshida, A., Negoro, H., Nakajima, M., Ueda, Y., Chujo, H., Yamaoka, K., Yamazaki, O., Nakahira, S., You, T., Ishiwata, R., Miyoshi, S., Eguchi, S., Hiroi, K., Katayama, H., and Ebisawa, K. (2009). The MAXI Mission on the ISS: Science and Instruments for Monitoring All-Sky X-Ray Images. *Publications of the ASJ*, 61:999.
- McClintock, J. E., Rappaport, S., Joss, P. C., Bradt, H., Buff, J., Clark, G. W., Hearn, D., Lewin, W. H. G., Matilsky, T., Mayer, W., and Primini, F. (1976). Discovery of a 283-second periodic variation in the X-ray source 3U 0900-40. *Astrophysical Journal, Letters*, 206:L99–L102.
- Meidinger, N., Barbera, M., Emberger, V., Fürmetz, M., Manhart, M., Müller-Seidlitz, J., Nandra, K., Plattner, M., Rau, A., and Treberspurg, W. (2017). The Wide Field Imager instrument for Athena. In

- Society of Photo-Optical Instrumentation Engineers (SPIE) Conference Series*, volume 10397 of *Society of Photo-Optical Instrumentation Engineers (SPIE) Conference Series*, page 103970V.
- Merloni, A., Predehl, P., Becker, W., Böhringer, H., Boller, T., Brunner, H., Brusa, M., Dennerl, K., Freyberg, M., and Friedrich, P. (2012). eROSITA Science Book: Mapping the Structure of the Energetic Universe. *arXiv e-prints*, page arXiv:1209.3114.
- Mewe, R. and Schrijver, J. (1978). Heliumlike ion line intensities. I - Stationary plasmas. II - Non-stationary plasmas. *Astronomy and Astrophysics*, 65:99–121.
- Mineo, T., Lotti, S., Molendi, S., and Ghizzardi, S. (2017). An XMM-Newton proton response matrix. *Experimental Astronomy*, 44(3):287–296.
- Mirabel, I. F., Rodriguez, L. F., Cordier, B., Paul, J., and Lebrun, F. (1992). A double-sided radio jet from the compact Galactic Centre annihilator 1E1740.7-2942. *Nature*, 358(6383):215–217.
- Miškovičová, I., Hell, N., Hanke, M., Nowak, M. A., Pottschmidt, K., Schulz, N. S., Grinberg, V., Duro, R., Madej, O. K., Lohfink, A. M., Rodriguez, J., Cadolle Bel, M., Bodaghee, A., Tomsick, J. A., Lee, J. C., Brown, G. V., and Wilms, J. (2016). Chandra X-ray spectroscopy of focused wind in the Cygnus X-1 system. II. The non-dip spectrum in the low/hard state - modulations with orbital phase. *Astronomy and Astrophysics*, 590:A114.
- Molendi, S., Bianchi, S., and Matt, G. (2003). Iron and nickel line properties in the X-ray-reflecting region of the Circinus galaxy. *Monthly Notices of the RAS*, 343(1):L1–L4.
- Nandra, K., Barret, D., Barcons, X., Fabian, A., den Herder, J.-W., Piro, L., Watson, M., Adami, C., Aird, J., Afonso, J. M., Alexander, D., Argiroffi, C., Amati, L., Arnaud, M., Atteia, J.-L., Audard, M., Badenes, C., Ballet, J., Ballo, L., Bamba, A., Bhardwaj, A., Stefano Battistelli, E., Becker, W., De Becker, M., Behar, E., Bianchi, S.,

Biffi, V., Bîrzan, L., Bocchino, F., Bogdanov, S., Boirin, L., Boller, T., Borgani, S., Borm, K., Bouché, N., Bourdin, H., Bower, R., Braitto, V., Branchini, E., Branduardi-Raymont, G., Bregman, J., Brenneman, L., Brightman, M., Brügger, M., Buchner, J., Bulbul, E., Brusa, M., Bursa, M., Caccianiga, A., Cackett, E., Campana, S., Cappelluti, N., Cappi, M., Carrera, F., Ceballos, M., Christensen, F., Chu, Y.-H., Churazov, E., Clerc, N., Corbel, S., Corral, A., Comastri, A., Costantini, E., Croston, J., Dadina, M., D’Ai, A., Decourchelle, A., Della Ceca, R., Dennerl, K., Dolag, K., Done, C., Dovciak, M., Drake, J., Eckert, D., Edge, A., Etori, S., Ezoe, Y., Feigelson, E., Fender, R., Feruglio, C., Finoguenov, A., Fiore, F., Galeazzi, M., Gallagher, S., Gandhi, P., Gaspari, M., Gastaldello, F., Georgakakis, A., Georgantopoulos, I., Gilfanov, M., Gitti, M., Gladstone, R., Goosmann, R., Gosset, E., Grosso, N., Guedel, M., Guerrero, M., Haberl, F., Hardcastle, M., Heinz, S., Alonso Herrero, A., Hervé, A., Holmstrom, M., Iwasawa, K., Jonker, P., Kaastra, J., Kara, E., Karas, V., Kastner, J., King, A., Kosenko, D., Koutroumpa, D., Kraft, R., Kreykenbohm, I., Lallement, R., Lanzuisi, G., Lee, J., Lemoine-Goumard, M., Lobban, A., Lodato, G., Lovisari, L., Lotti, S., McCharthy, I., McNamara, B., Maggio, A., Maiolino, R., De Marco, B., de Martino, D., Mateos, S., Matt, G., Maughan, B., Mazzotta, P., Mendez, M., Merloni, A., Micela, G., Miceli, M., Mignani, R., Miller, J., Miniutti, G., Molendi, S., Montez, R., Moretti, A., Motch, C., Nazé, Y., Nevalainen, J., Nicastro, F., Nulsen, P., Ohashi, T., O’Brien, P., Osborne, J., Oskinova, L., Pacaud, F., Paerels, F., Page, M., Papadakis, I., Pareschi, G., Petre, R., Petrucci, P.-O., Piconcelli, E., Pillitteri, I., Pinto, C., de Plaa, J., Pointecouteau, E., Ponman, T., Ponti, G., Porquet, D., Pounds, K., Pratt, G., Predehl, P., Proga, D., Psaltis, D., Rafferty, D., Ramos-Ceja, M., Ranalli, P., Rasia, E., Rau, A., Rauw, G., Rea, N., Read, A., Reeves, J., Reiprich, T., Renaud, M., Reynolds, C., Risaliti, G., Rodriguez, J., Rodriguez Hidalgo, P., Roncarelli, M., Rosario, D., Rossetti, M., Rozanska, A., Rovilos, E., Salvaterra, R., Salvato, M., Di Salvo, T., Sanders, J., Sanz-Forcada, J., Schawinski, K., Schaye, J., Schwobe, A., Sciortino, S., Severgnini, P., Shankar, F., Sijacki, D., Sim, S., Schmid, C., Smith, R., Steiner, A., Stelzer, B., Stewart, G., Strohmayer, T.,

- Strüder, L., Sun, M., Takei, Y., Tatischeff, V., Tiengo, A., Tombesi, F., Trinchieri, G., Tsuru, T. G., Ud-Doula, A., Ursino, E., Valencic, L., Vanzella, E., Vaughan, S., Vignali, C., Vink, J., Vito, F., Volonteri, M., Wang, D., Webb, N., Willingale, R., Wilms, J., Wise, M., Worrall, D., Young, A., Zampieri, L., In't Zand, J., Zane, S., Zezas, A., Zhang, Y., and Zhuravleva, I. (2013). The Hot and Energetic Universe: A White Paper presenting the science theme motivating the Athena+ mission. *arXiv e-prints*, page arXiv:1306.2307.
- Nardiello, D., Libralato, M., Piotto, G., Anderson, J., Bellini, A., Aparicio, A., Bedin, L. R., Cassisi, S., Granata, V., King, I. R., Lucertini, F., Marino, A. F., Milone, A. P., Ortolani, S., Platais, I., and van der Marel, R. P. (2018). The Hubble Space Telescope UV Legacy Survey of Galactic Globular Clusters - XVII. Public Catalogue Release. *Monthly Notices of the RAS*, 481:3382–3393.
- Noble, M. S. and Nowak, M. A. (2008a). Beyond XSPEC: Toward Highly Configurable Astrophysical Analysis. *Publications of the ASP*, 120(869):821.
- Noble, M. S. and Nowak, M. A. (2008b). Beyond XSPEC: Toward Highly Configurable Astrophysical Analysis. *Publications of the ASP*, 120(869):821.
- Odaka, H., Khangulyan, D., Tanaka, Y. T., Watanabe, S., Takahashi, T., and Makishima, K. (2013). Short-term Variability of X-Rays from Accreting Neutron Star Vela X-1. I. Suzaku Observations. *Astrophysical Journal*, 767(1):70.
- Palmeri, P., Mendoza, C., Kallman, T. R., Bautista, M. A., and Meléndez, M. (2003). Modeling of iron K lines: Radiative and Auger decay data for Fe II-Fe IX. *Astronomy and Astrophysics*, 410:359–364.
- Papitto, A., Ferrigno, C., Bozzo, E., Rea, N., Pavan, L., Burderi, L., Burgay, M., Campana, S., di Salvo, T., Falanga, M., Filipović, M. D., Freire, P. C. C., Hessels, J. W. T., Possenti, A., Ransom, S. M., Riggio, A., Romano, P., Sarkissian, J. M., Stairs, I. H., Stella, L., Torres, D. F., Wieringa, M. H., and Wong, G. F. (2013). Swings

- between rotation and accretion power in a binary millisecond pulsar. *Nature*, 501:517–520.
- Pavlov, G. G., Kargaltsev, O., Garmire, G. P., and Wolszczan, A. (2007). X-Ray Emission from the Planet Pulsar B1257+12. *Astrophysical Journal*, 664:1072–1078.
- Piotto, G., Milone, A. P., Bedin, L. R., Anderson, J., King, I. R., Marino, A. F., Nardiello, D., Aparicio, A., Barbuy, B., Bellini, A., Brown, T. M., Cassisi, S., Cool, A. M., Cunial, A., Dalessandro, E., D’Antona, F., Ferraro, F. R., Hidalgo, S., Lanzoni, B., Monelli, M., Ortolani, S., Renzini, A., Salaris, M., Sarajedini, A., van der Marel, R. P., Vesperini, E., and Zoccali, M. (2015). The Hubble Space Telescope UV Legacy Survey of Galactic Globular Clusters. I. Overview of the Project and Detection of Multiple Stellar Populations. *Astronomical Journal*, 149:91.
- Porquet, D. and Dubau, J. (2000). X-ray photoionized plasma diagnostics with helium-like ions. Application to warm absorber-emitter in active galactic nuclei. *Astronomy and Astrophysics, Supplement*, 143:495–514.
- Porquet, D., Dubau, J., and Grosso, N. (2010). He-like Ions as Practical Astrophysical Plasma Diagnostics: From Stellar Coronae to Active Galactic Nuclei. *Space Science Reviews*, 157(1-4):103–134.
- Porquet, D., Mewe, R., Dubau, J., Raassen, A. J. J., and Kaastra, J. S. (2001). Line ratios for helium-like ions: Applications to collision-dominated plasmas. *Astronomy and Astrophysics*, 376:1113–1122.
- Predehl, P., Andritschke, R., Arefiev, V., Babyshkin, V., Batanov, O., Becker, W., Böhringer, H., Bogomolov, A., Boller, T., Borm, K., Bornemann, W., Bräuninger, H., Brüggem, M., Brunner, H., Brusa, M., Bulbul, E., Buntov, M., Burwitz, V., Burkert, W., Clerc, N., Churazov, E., Coutinho, D., Dauser, T., Dennerl, K., Doroshenko, V., Eder, J., Emberger, V., Eraerds, T., Finoguenov, A., Freyberg, M., Friedrich, P., Friedrich, S., Fürmetz, M., Georgakakis, A., Gilfanov, M., Granato, S., Grossberger, C., Gueguen, A., Gureev, P., Haberl,

- F., Hälker, O., Hartner, G., Hasinger, G., Huber, H., Ji, L., Kienlin, A. v., Kink, W., Korotkov, F., Kreykenbohm, I., Lamer, G., Lomakin, I., Lapshov, I., Liu, T., Maitra, C., Meidinger, N., Menz, B., Merloni, A., Mernik, T., Mican, B., Mohr, J., Müller, S., Nandra, K., Nazarov, V., Pacaud, F., Pavlinsky, M., Perinati, E., Pfeffermann, E., Pietschner, D., Ramos-Ceja, M. E., Rau, A., Reiffers, J., Reiprich, T. H., Robrade, J., Salvato, M., Sanders, J., Santangelo, A., Sasaki, M., Scheuerle, H., Schmid, C., Schmitt, J., Schwöpe, A., Shirshakov, A., Steinmetz, M., Stewart, I., Strüder, L., Sunyaev, R., Tenzer, C., Tiedemann, L., Trümper, J., Voron, V., Weber, P., Wilms, J., and Yaroshenko, V. (2020). The eROSITA X-ray telescope on SRG. *arXiv e-prints*, page arXiv:2010.03477.
- Prigozhin, G. Y., Kissel, S. E., Bautz, M. W., Grant, C., LaMarr, B., Foster, R. F., Ricker, G. R., and Garmire, G. P. (2000). Radiation damage in the Chandra x-ray CCDs. In Truemper, J. E. and Aschenbach, B., editors, *X-Ray Optics, Instruments, and Missions III*, volume 4012 of *Society of Photo-Optical Instrumentation Engineers (SPIE) Conference Series*, pages 720–730.
- Pringle, J. E. and Rees, M. J. (1972). Accretion Disc Models for Compact X-Ray Sources. *Astronomy and Astrophysics*, 21:1.
- Quaintrell, H., Norton, A. J., Ash, T. D. C., Roche, P., Willems, B., Bedding, T. R., Baldry, I. K., and Fender, R. P. (2003). The mass of the neutron star in Vela X-1 and tidally induced non-radial oscillations in GP Vel. *Astronomy and Astrophysics*, 401:313–323.
- Rasmussen, A., Chervinsky, J., and Golovchenko, J. (1999). Proton scattering off of XMM optics: XMM mirror and RGS grating sample. Rgs-col-cal-99009, Columbia Astrophysics Laboratory.
- Rau, A., Meidinger, N., Nandra, K., Porro, M., Barret, D., Santangelo, A., Schmid, C., Strüder, L., Tenzer, C., Wilms, J., Amorós, C., Andritschke, R., Aschauer, F., Bahr, A., Günther, B., Furmetz, M., Ott, B., Perinati, E., Rambaudo, D., Reiffers, J., Treis, J., von Kienlin, A., and Weidenspointner, G. (2013). The Hot and Energetic Universe:

- The Wide Field Imager (WFI) for Athena+. *arXiv e-prints*, page arXiv:1308.6785.
- Remizovich, V. S., Ryazanov, M. I., and Tilinin, I. S. (1980). Energy and angular distributions of particles reflected in glancing incidence of a beam of ions on the surface of a material. *Soviet Journal of Experimental and Theoretical Physics*, 52:225.
- Roberts, M. S. E. (2011). New Black Widows and Redbacks in the Galactic Field. In Burgay, M., D’Amico, N., Esposito, P., Pellizzoni, A., and Possenti, A., editors, *American Institute of Physics Conference Series*, volume 1357 of *American Institute of Physics Conference Series*, pages 127–130.
- Roberts, M. S. E. (2013). Surrounded by spiders! New black widows and redbacks in the Galactic field. In van Leeuwen, J., editor, *Neutron Stars and Pulsars: Challenges and Opportunities after 80 years*, volume 291 of *IAU Symposium*, pages 127–132.
- Roberts, M. S. E., Al Noori, H., Torres, R. A., McLaughlin, M. A., Gentile, P. A., Hessels, J. W. T., Ransom, S. M., Ray, P. S., Kerr, M., and Breton, R. P. (2018). X-Ray and Optical Properties of Black Widows and Redbacks. In Weltevrede, P., Perera, B. B. P., Preston, L. L., and Sanidas, S., editors, *Pulsar Astrophysics the Next Fifty Years*, volume 337 of *IAU Symposium*, pages 43–46.
- Roberts, M. S. E., McLaughlin, M. A., Gentile, P. A., Ray, P. S., Ransom, S. M., and Hessels, J. W. T. (2015). X-Ray Studies of Redbacks. *ArXiv e-prints*.
- Romani, R. W. and Sanchez, N. (2016). Intra-binary Shock Heating of Black Widow Companions. *Astrophysical Journal*, 828:7.
- Sako, M., Kahn, S. M., Paerels, F., and Liedahl, D. A. (2000). The Chandra High-Energy Transmission Grating Observation of an X-Ray Ionization Cone in Markarian 3. *Astrophysical Journal, Letters*, 543(2):L115–L118.

- Sako, M., Liedahl, D. A., Kahn, S. M., and Paerels, F. (1999). The X-Ray Spectrum and Global Structure of the Stellar Wind in VELA X-1. *Astrophysical Journal*, 525:921–934.
- Salveti, D., Marelli, M., Gastaldello, F., Ghizzardi, S., Molendi, S., Luca, A. D., Moretti, A., Rossetti, M., and Tiengo, A. (2017). A systematic analysis of the XMM-Newton background: II. Properties of the in-Field-Of-View excess component. *Experimental Astronomy*, 44:309–320.
- Sander, A. A. C., Fürst, F., Kretschmar, P., Oskinova, L. M., Todt, H., Hainich, R., Shenar, T., and Hamann, W. R. (2018). Coupling hydrodynamics with comoving frame radiative transfer. II. Stellar wind stratification in the high-mass X-ray binary Vela X-1. *Astronomy and Astrophysics*, 610:A60.
- Scargle, J. D., Norris, J. P., Jackson, B., and Chiang, J. (2013). Studies in Astronomical Time Series Analysis. VI. Bayesian Block Representations. *Astrophysical Journal*, 764(2):167.
- Schulz, N. S., Canizares, C. R., Lee, J. C., and Sako, M. (2002). The Ionized Stellar Wind in Vela X-1 during Eclipse. *Astrophysical Journal, Letters*, 564(1):L21–L25.
- Shishkovsky, L., Strader, J., Chomiuk, L., Bahramian, A., Tremou, E., Li, K.-L., Salinas, R., Tudor, V., Miller-Jones, J. C. A., Maccarone, T. J., Heinke, C. O., and Sivakoff, G. R. (2018). The MAVERIC Survey: A Red Straggler Binary with an Invisible Companion in the Galactic Globular Cluster M10. *Astrophysical Journal*, 855:55.
- Simioni, M., Bedin, L. R., Aparicio, A., Piotto, G., Milone, A. P., Nardiello, D., Anderson, J., Bellini, A., Brown, T. M., Cassisi, S., Cunial, A., Granata, V., Ortolani, S., van der Marel, R. P., and Vesperini, E. (2018). The Hubble Space Telescope UV Legacy Survey of Galactic globular clusters - XIII. ACS/WFC parallel-field catalogues. *Monthly Notices of the RAS*, 476:271–299.
- Sirianni, M., Jee, M. J., Benítez, N., Blakeslee, J. P., Martel, A. R., Meurer, G., Clampin, M., De Marchi, G., Ford, H. C., Gilliland,

- R., Hartig, G. F., Illingworth, G. D., Mack, J., and McCann, W. J. (2005). The Photometric Performance and Calibration of the Hubble Space Telescope Advanced Camera for Surveys. *Publications of the ASP*, 117:1049–1112.
- Spiga, D., Cusumano, G., and Pareschi, G. (2007). HEW simulations and quantification of the microroughness requirements for x-ray telescopes by means of numerical and analytical methods. In *Proceedings of the SPIE*, volume 6688 of *Society of Photo-Optical Instrumentation Engineers (SPIE) Conference Series*, page 66880H.
- Stappers, B. W., Archibald, A. M., Hessels, J. W. T., Bassa, C. G., Bogdanov, S., Janssen, G. H., Kaspi, V. M., Lyne, A. G., Patruno, A., Tendulkar, S., Hill, A. B., and Glanzman, T. (2014). A State Change in the Missing Link Binary Pulsar System PSR J1023+0038. *Astrophysical Journal*, 790:39.
- Stockman, Y., Barzin, P., Domken, I., Valenzuela, A., and Grossi, G. (2001). Environmental Testing of XMM-Newton Optics (Invited Paper). In Schürmann, B., editor, *Fourth International Symposium Environmental Testing for Space Programmes*, volume 467 of *ESA Special Publication*, page 11.
- Strader, J., Swihart, S., Chomiuk, L., Bahramian, A., Britt, C., Cheung, C. C., Dage, K., Halpern, J., Li, K.-L., Mignani, R. P., Orosz, J. A., Peacock, M., Salinas, R., Shishkovsky, L., and Tremou, E. (2019). Optical Spectroscopy and Demographics of Redback Millisecond Pulsar Binaries. *Astrophysical Journal*, 872:42.
- Strohmayer, T. E., Zhang, W., Swank, J. H., Smale, A., Titarchuk, L., Day, C., and Lee, U. (1996). Millisecond X-Ray Variability from an Accreting Neutron Star System. *Astrophysical Journal, Letters*, 469:L9.
- Strüder, L., Briel, U., Dennerl, K., Hartmann, R., Kendziorra, E., Meindinger, N., Pfeiffermann, E., Reppin, C., Aschenbach, B., Bornemann, W., Bräuninger, H., Burkert, W., Elender, M., Freyberg, M., Haberl,

- F., Hartner, G., Heuschmann, F., Hippmann, H., Kastelic, E., Kemmer, S., Kettenring, G., Kink, W., Krause, N., Müller, S., Oppitz, A., Pietsch, W., Popp, M., Predehl, P., Read, A., Stephan, K. H., Stötter, D., Trümper, J., Holl, P., Kemmer, J., Soltau, H., Stötter, R., Weber, U., Weichert, U., von Zanthier, C., Carathanassis, D., Lutz, G., Richter, R. H., Solc, P., Böttcher, H., Kuster, M., Staubert, R., Abbey, A., Holland, A., Turner, M., Balasini, M., Bignami, G. F., La Palombara, N., Villa, G., Buttler, W., Gianini, F., Lainé, R., Lumb, D., and Dhez, P. (2001). The European Photon Imaging Camera on XMM-Newton: The pn-CCD camera. *Astronomy and Astrophysics*, 365:L18–L26.
- Sutantyo, W. (1975). The formation of globular cluster X-ray sources through neutron star-giant collisions. *Astronomy and Astrophysics*, 44:227–230.
- Tashiro, M., Maejima, H., Toda, K., Kelley, R., Reichenthal, L., Lobell, J., Petre, R., Guainazzi, M., Costantini, E., Edison, M., Fujimoto, R., Grim, M., Hayashida, K., den Herder, J.-W., Ishisaki, Y., Paltani, S., Matsushita, K., Mori, K., Sneiderman, G., Takei, Y., Terada, Y., Tomida, H., Akamatsu, H., Angelini, L., Arai, Y., Awaki, H., Babyk, I., Bamba, A., Barfknecht, P., Barnstable, K., Bialas, T., Blagojevic, B., Bonafede, J., Brambora, C., Brenneman, L., Brown, G., Brown, K., Burns, L., Canavan, E., Carnahan, T., Chiao, M., Comber, B., Corrales, L., de Vries, C., Dercksen, J., Diaz-Trigo, M., Dillard, T., DiPirro, M., Done, C., Dotani, T., Ebisawa, K., Eckart, M., Enoto, T., Ezoe, Y., Ferrigno, C., Fukazawa, Y., Fujita, Y., Furuzawa, A., Gallo, L., Graham, S., Gu, L., Hagino, K., Hamaguchi, K., Hatsukade, I., Hawes, D., Hayashi, T., Hegarty, C., Hell, N., Hiraga, J., Hodges-Kluck, E., Holland, M., Hornschemeier, A., Hoshino, A., Ichinohe, Y., Iizuka, R., Ishibashi, K., Ishida, M., Ishikawa, K., Ishimura, K., James, B., Kallman, T., Kara, E., Katsuda, S., Kenyon, S., Kilbourne, C., Kimball, M., Kitaguti, T., Kitamoto, S., Kobayashi, S., Kohmura, T., Koyama, S., Kubota, A., Leutenegger, M., Lockard, T., Loewenstein, M., Maeda, Y., Marbley, L., Markevitch, M., Matsumoto, H., Matsuzaki, K., McCammon, D., McNamara, B., Miko, J., Miller, E., Miller, J., Minesugi, K., Mitsuishi, I., Mizuno, T., Mori, H., Mukai,

- K., Murakami, H., Mushotzky, R., Nakajima, H., Nakamura, H., Nakashima, S., Nakazawa, K., Natsukari, C., Nigo, K., Nishioka, Y., Nobukawa, K., Nobukawa, M., Noda, H., Odaka, H., Ogawa, M., Ohashi, T., Ohno, M., Ohta, M., Okajima, T., Okamoto, A., Onizuka, M., Ota, N., Ozaki, M., Plucinsky, P., Porter, F. S., Pottschmidt, K., Sato, K., Sato, R., Sawada, M., Seta, H., Shelton, K., Shibano, Y., Shida, M., Shidatsu, M., Shirron, P., Simionescu, A., Smith, R., Someya, K., Soong, Y., Suagawara, Y., Szymkowiak, A., Takahashi, H., Tamagawa, T., Tamura, T., Tanaka, T., Terashima, Y., Tsuboi, Y., Tsujimoto, M., Tsunemi, H., Tsuru, T., Uchida, H., Uchiyama, H., Ueda, Y., Uno, S., Walsh, T., Watanabe, S., Williams, B., Wolfs, R., Wright, M., Yamada, S., Yamaguchi, H., Yamaoka, K., Yamasaki, N., Yamauchi, S., Yamauchi, M., Yanagase, K., Yaqoob, T., Yasuda, S., Yoshioka, N., Zabala, J., and Irina, Z. (2018). Concept of the X-ray Astronomy Recovery Mission. In *Proceedings of the SPIE*, volume 10699 of *Society of Photo-Optical Instrumentation Engineers (SPIE) Conference Series*, page 1069922.
- Tauris, T. M. and van den Heuvel, E. P. J. (2006). *Formation and evolution of compact stellar X-ray sources*, volume 39, pages 623–665.
- The Fermi-LAT collaboration (2019). Fermi Large Area Telescope Fourth Source Catalog. *arXiv e-prints*, page arXiv:1902.10045.
- Tiengo, A. (2007). Reduction of soft protons background in Simbol-X: effects of thermal blankets and magnetic diverter. Tech Report SX-IASFMI-TN-0001.
- Turner, M. J. L., Abbey, A., Arnaud, M., Balasini, M., Barbera, M., Belsole, E., Bennie, P. J., Bernard, J. P., Bignami, G. F., Boer, M., Briel, U., Butler, I., Cara, C., Chabaud, C., Cole, R., Collura, A., Conte, M., Cros, A., Denby, M., Dhez, P., Di Coco, G., Dowson, J., Ferrando, P., Ghizzardi, S., Gianotti, F., Goodall, C. V., Gretton, L., Griffiths, R. G., Hainaut, O., Hochedez, J. F., Holland, A. D., Jourdain, E., Kendziorra, E., Lagostina, A., Laine, R., La Palombara, N., Lortholary, M., Lumb, D., Marty, P., Molendi, S., Pigot, C., Poindron, E., Pounds, K. A., Reeves, J. N., Reppin, C., Rothenflug,

- R., Salvétat, P., Sauvageot, J. L., Schmitt, D., Sembay, S., Short, A. D. T., Spragg, J., Stephen, J., Strüder, L., Tiengo, A., Trifoglio, M., Trümper, J., Vercellone, S., Vigroux, L., Villa, G., Ward, M. J., Whitehead, S., and Zonca, E. (2001). The European Photon Imaging Camera on XMM-Newton: The MOS cameras : The MOS cameras. *Astronomy and Astrophysics*, 365:L27–L35.
- Tzanavaris, P. and Yaqoob, T. (2018). New Constraints on the Geometry and Kinematics of Matter Surrounding the Accretion Flow in X-Ray Binaries from Chandra High-energy Transmission Grating X-Ray Spectroscopy. *Astrophysical Journal*, 855(1):25.
- van den Heuvel, E. P. J. and Heise, J. (1972). Centaurus X-3, Possible Reactivation of an Old Neutron Star by Mass Exchange in a Close Binary. *Nature Physical Science*, 239(92):67–69.
- van Loon, J. T., Kaper, L., and Hammerschlag-Hensberge, G. (2001). Modelling the orbital modulation of ultraviolet resonance lines in high-mass X-ray binaries. *Astronomy and Astrophysics*, 375:498–526.
- Verner, D. A., Ferland, G. J., Korista, K. T., and Yakovlev, D. G. (1996). Atomic Data for Astrophysics. II. New Analytic FITS for Photoionization Cross Sections of Atoms and Ions. *Astrophysical Journal*, 465:487.
- Wadiasingh, Z., Harding, A. K., Venter, C., Böttcher, M., and Baring, M. G. (2017). Constraining Relativistic Bow Shock Properties in Rotation-powered Millisecond Pulsar Binaries. *Astrophysical Journal*, 839:80.
- Walter, R., Lutovinov, A. A., Bozzo, E., and Tsygankov, S. S. (2015). High-mass X-ray binaries in the Milky Way. A closer look with INTEGRAL. *Astronomy and Astrophysics Reviews*, 23:2.
- Wargelin, B. J., Beiersdorfer, P., Liedahl, D. A., Kahn, S. M., and von Goeler, S. (1998). Observation and Modeling of High-n Iron L-Shell Lines from Intermediate Ion Stages. *Astrophysical Journal*, 496(2):1031–1043.

- Watanabe, S., Sako, M., Ishida, M., Ishisaki, Y., Kahn, S. M., Kohmura, T., Nagase, F., Paerels, F., and Takahashi, T. (2006). X-Ray Spectral Study of the Photoionized Stellar Wind in Vela X-1. *Astrophysical Journal*, 651(1):421–437.
- Watts, A. L. (2012). Thermonuclear Burst Oscillations. *Annual Review of Astron. and Astrophys.*, 50:609–640.
- Webb, N. A., Gendre, B., and Barret, D. (2002). First XMM-Newton observations of the globular cluster M 22. *Astronomy and Astrophysics*, 381:481–486.
- Webb, N. A., Serre, D., Gendre, B., Barret, D., Lasota, J.-P., and Rizzi, L. (2004). X-ray sources and their optical counterparts in the globular cluster <ASTROBJ>M 22</ASTROBJ>. *Astronomy and Astrophysics*, 424:133–143.
- Webb, N. A. and Servillat, M. (2013). CV1 in the globular cluster M 22: confirming its nature through X-ray observations and optical spectroscopy. *Astronomy and Astrophysics*, 551:A60.
- Weisskopf, M. C., Tananbaum, H. D., Van Speybroeck, L. P., and O’Dell, S. L. (2000). Chandra X-ray Observatory (CXO): overview. In Truemper, J. E. and Aschenbach, B., editors, *X-Ray Optics, Instruments, and Missions III*, volume 4012 of *Proceedings of the SPIE*, pages 2–16.
- Willingale, R., Pareschi, G., Christensen, F., and den Herder, J.-W. (2013). The Hot and Energetic Universe: The Optical Design of the Athena+ Mirror. *arXiv e-prints*, page arXiv:1307.1709.
- Wilms, J., Allen, A., and McCray, R. (2000). On the Absorption of X-Rays in the Interstellar Medium. *Astrophysical Journal*, 542:914–924.
- Wojdowski, P. S., Liedahl, D. A., Sako, M., Kahn, S. M., and Paerels, F. (2003). Resolving the Effects of Resonant X-Ray Line Scattering in Centaurus X-3 with Chandra. *Astrophysical Journal*, 582(2):959–971.

- XRISM Science Team (2020). Science with the x-ray imaging and spectroscopy mission (xrism).
- Young, A. J., Nowak, M. A., Markoff, S., Marshall, H. L., and Canizares, C. R. (2007). High-Resolution X-Ray Spectroscopy of a Low-Luminosity Active Galactic Nucleus: The Structure and Dynamics of M81*. *Astrophysical Journal*, 669(2):830–840.
- Zavlin, V. E. (2007). Studying millisecond pulsars in X-rays. *Astrophysics and Space Science*, 308:297–307.
- Zavlin, V. E., Pavlov, G. G., and Shibano, Y. A. (1996). Model neutron star atmospheres with low magnetic fields. I. Atmospheres in radiative equilibrium. *Astronomy and Astrophysics*, 315:141–152.
- Zhou, J. N., Zhang, P. F., Huang, X. Y., Li, X., Liang, Y. F., Fu, L., Yan, J. Z., and Liu, Q. Z. (2015). Gamma-ray emission from globular clusters 2MS-GC01, IC 1257, FSR 1735, NGC 5904 and 6656. *Monthly Notices of the RAS*, 448:3215–3220.
- Ziegler, J. F., Ziegler, M. D., and Biersack, J. P. (2010). SRIM - The stopping and range of ions in matter (2010). *Nuclear Instruments and Methods in Physics Research B*, 268(11-12):1818–1823.

Appendix A

Overall fits with the semi-empirical model

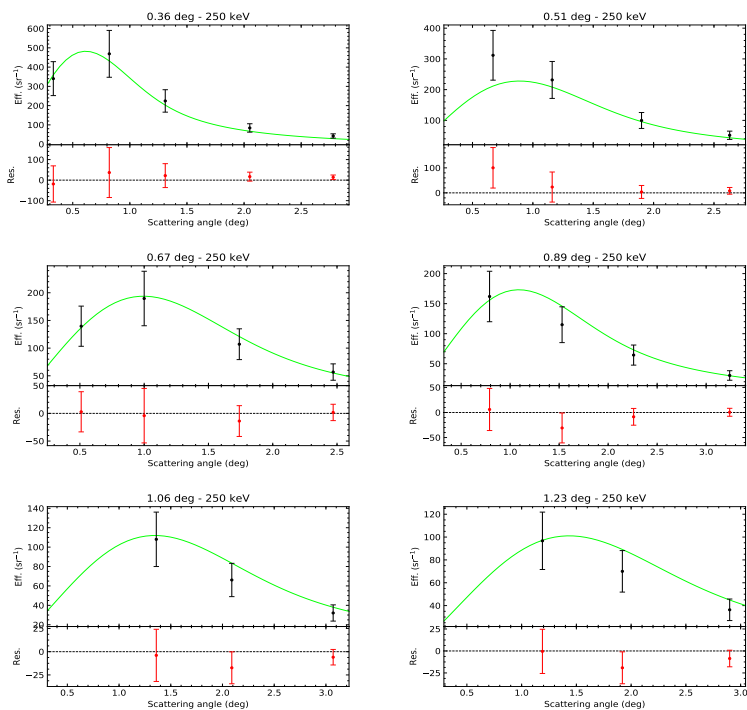


Fig. A.1 Fits of the scattering efficiencies from Diebold et al. (2015) with the Remizovich formula (Eq. 2.7) in non-elastic approximation. Incident energy of 250 keV.

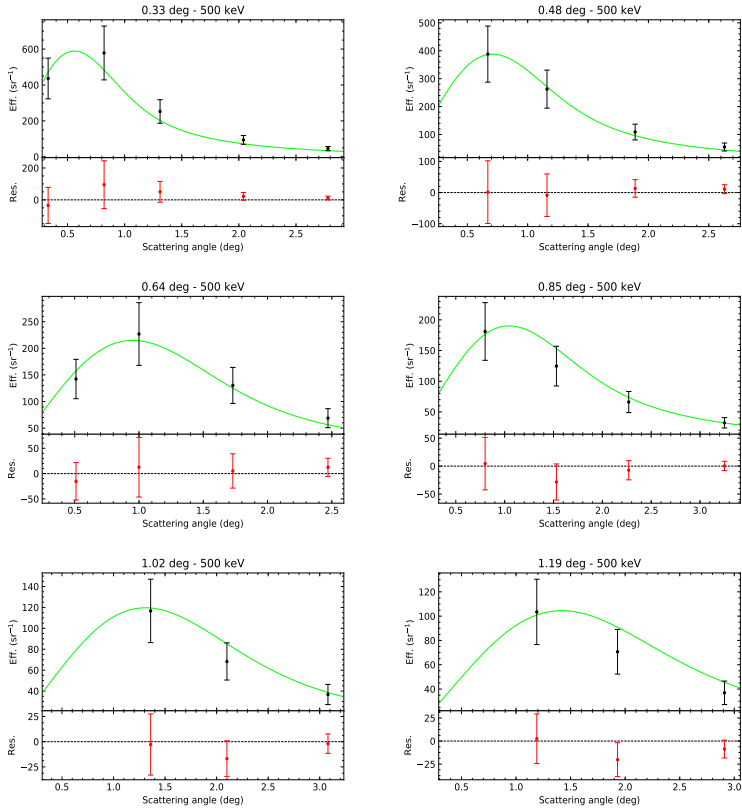


Fig. A.2 As before, for the incident energy of 500 keV.

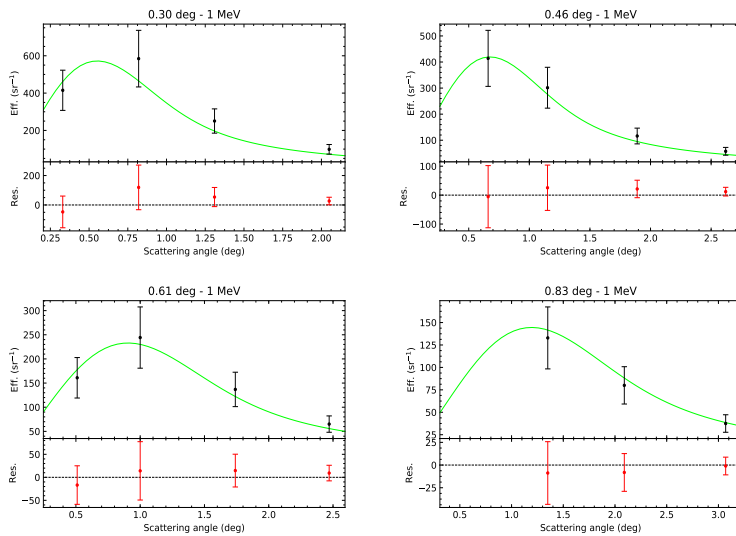


Fig. A.3 As before, for the incident energy of 1 MeV.

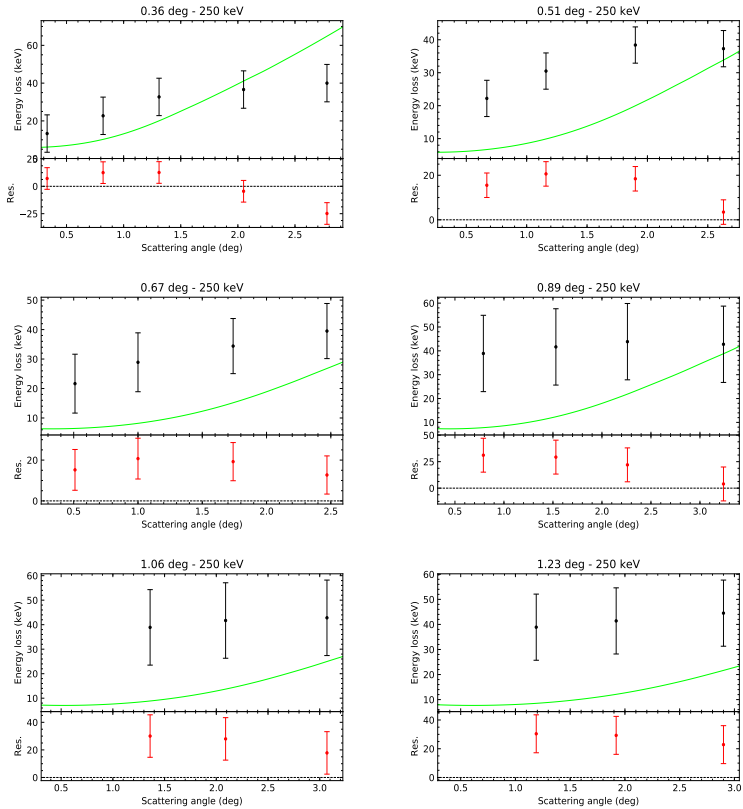


Fig. A.4 Fits of the energy losses from Diebold et al. (2015) with the Remizovich formula (Eq. 2.7) in non-elastic approximation. Incident energy of 250 keV.

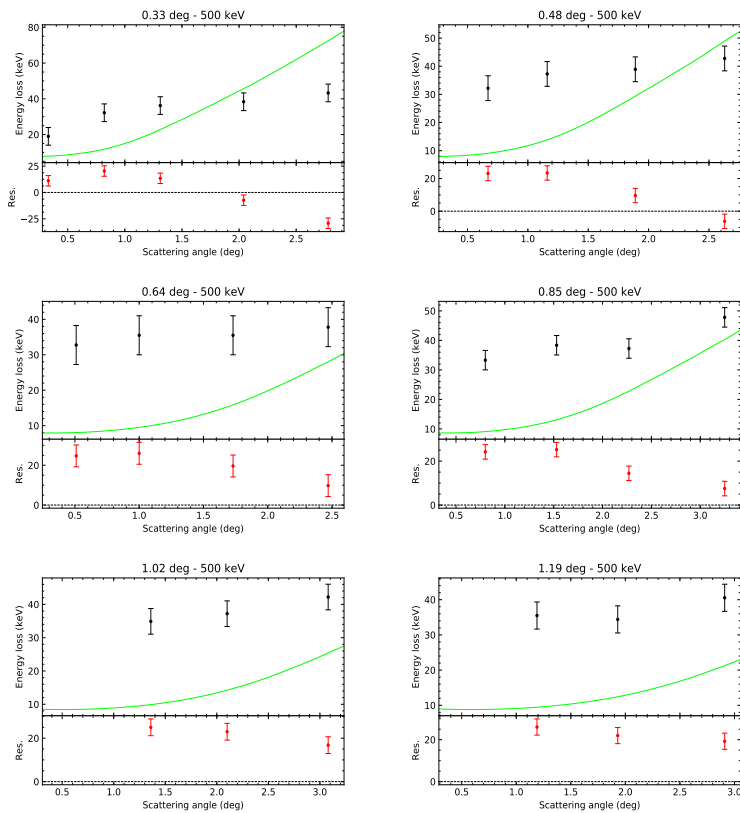


Fig. A.5 As before, for the incident energy of 500 keV.

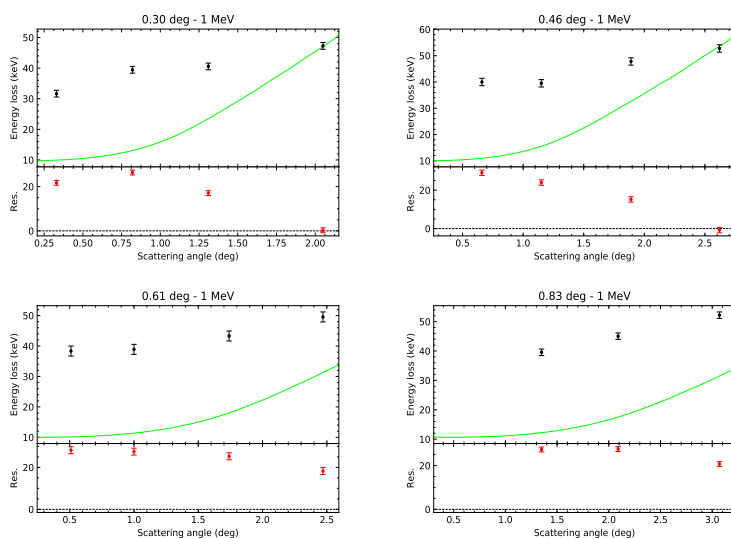


Fig. A.6 As before, for the incident energy of 1 MeV.

Appendix B

Comparison of SPO data with the semi-empirical model

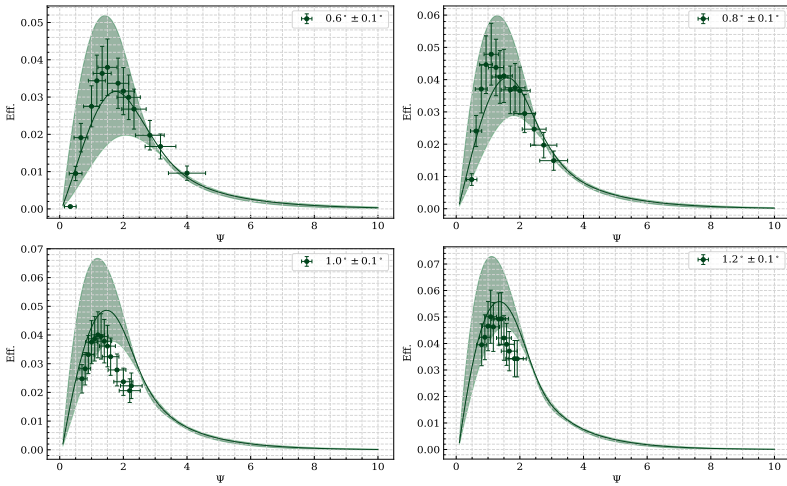


Fig. B.1 Comparison of the experimental scattering efficiency from the SPO sample (data points) with the semi-empirical model (solid line), for all the incident angles (0.6° , 0.8° , 1.0° , and 1.2°), at the low incident energy of 172 keV, and for the on-axis configuration. The green area above and under the solid curve correspond to the minimum and the maximum efficiency of the model, computed considering the upper and lower error at 2.7σ confidence level on the best-fit parameter σ .

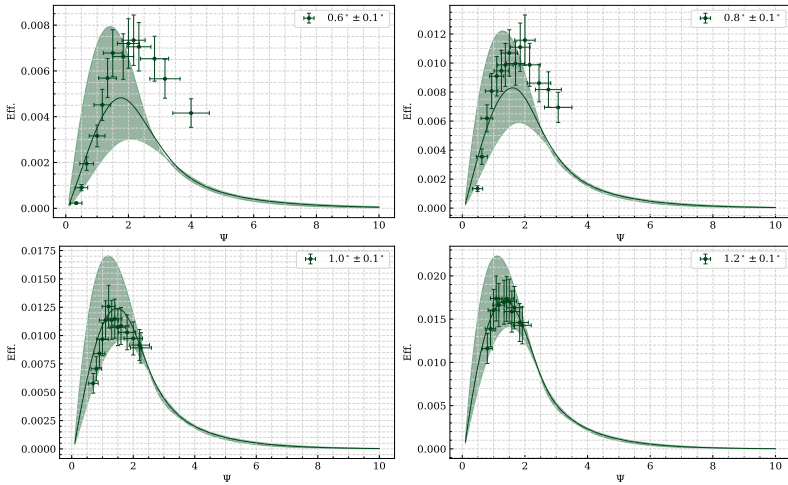


Fig. B.2 As before, for the off-axis configuration.

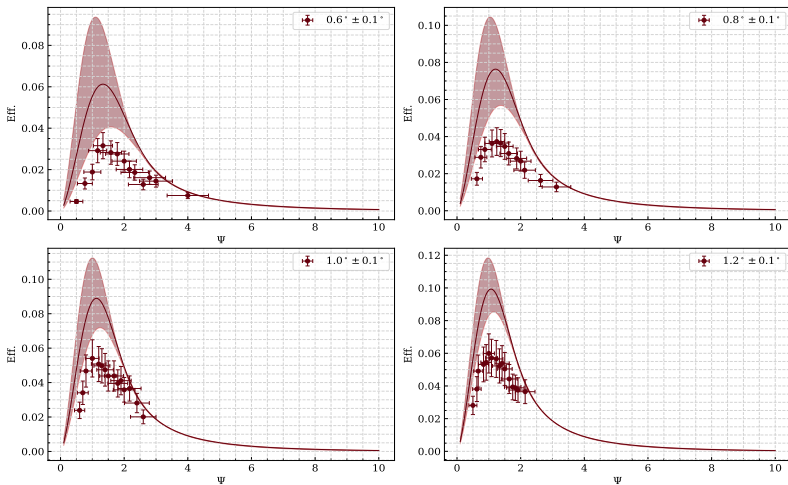


Fig. B.3 As before, for the high incident energy of 471 keV and the on-axis configuration.

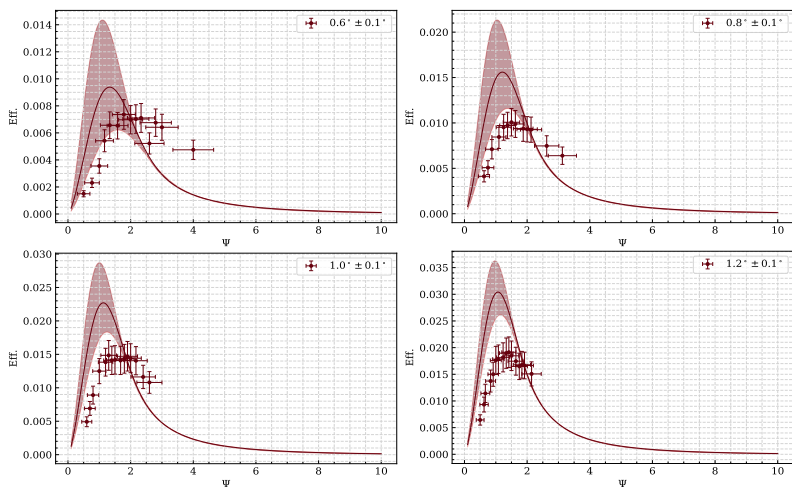


Fig. B.4 As before (incident energy of 471 keV), for the off-axis configuration.